UNIVERSITY OF CALIFORNIA SAN DIEGO

An Immersed Reproducing Kernel Particle Method for Modeling Inhomogeneous Media

A dissertation submitted in partial satisfaction of the
requirements for the degree
Doctor of Philosophy

in

Structural Engineering

by

Frank Beckwith

Committee in charge:

Jiun-Shyan Chen, Chair
Randolph Bank
Yuri Bazilevs
Hyonny Kim
Jesse Sherburn
Benson Shing

2018

The dissertation of Frank Beckwith is approved, and it is acceptable in quality and form for publication on microfilm and electronically:

_____

_____

_____

_____

_____

_____

Chair

University of California San Diego

2018

DEDICATION

To my family

EPIGRAPH

All truths are easy to understand once they are discovered;

the point is to discover them.

—Galileo Galilei

TABLE OF CONTENTS

LIST OF FIGURES

LIST OF TABLES

ACKNOWLEDGEMENTS

I would like to thank my advisor Professor J.S. Chen for his support and advice over the last four years. He has been very patient with my research and I feel privelaged to be part of his research group. I would also like to extend my thanks to Professor Randolph Bank, Professor Yuri Bazilevs, Professor Benson Shing, Professor Hyonny Kim, and Dr. Jesse Sherburn for serving on my committee.

The sponsorship of this research by the US Army Engineering Research Development Center and Sandia National Laboratories is greatly acknowledged. In particular, I had the privelage of interning at Sandia National Laboratories during the summers of 2015 and 2016 under the mentorship of Dr. Joseph Bishop and Dr. Stephen Attaway, both of whom have enthusiastically supported my research and were very helpful during my internships there. I would also like to thank Dr. Michael Tupek for his support and constant musings. Dr. Jesse Sherburn and Dr. Jason Roth from the US Army ERDC were both very helpful in providing data and advice to our research team for which I am thankful.

I must also thank all of my colleagues who I have worked with, who often gave me new ideas to approach a difficult problem: Dr. Haoyan Wei, Professor Michael Hillman, Dr. Edouard Yreux, Qizhi He, Jacob Koester, Marco Pasetto, Tsung-Hui "Alex" Huang, Jonghyuk Baek, Karan Taneja, Shigeki Kaneko, and Xialong He. Dr. Haoyan Wei in particular was very helpful in reviewing my work and had many ideas for improving on it.

Finally, I must also thank my family for their constant support, both financially and for my well-being. Through my struggles, they were always there to keep my spirits and believing in me through each step of this long journey.

Chapters 4, 5, and 6 are currently being prepared for submission for publication. F. Beckwith, J.S. Chen, and H. Wei, "An Immersed Reproducing Kernel Particle Method for Modeling Inhomogeneous Media."

Chapter 7 includes unpublished material which is coauthored with J.S. Chen, H. Wei, and

J. Sherburn. The dissertation author was the primary author of this chapter.

VITA

2011	B. S. in Civil Engineering, University of Idaho, Moscow
2015	M. S. in Structural Engineering, University of California, San Diego
2015-2018	Graduate Teaching Assistant, University of California, San Diego
2015-2016	Technical Graduate Student Intern, Sandia National Laboratories, Albuquerque
2018	Ph. D. in Structural Engineering, University of California, San Diego

PUBLICATIONS

F. Beckwith, J.S. Chen, and H. Wei, "An Immersed Reproducing Kernel Particle Method for Modeling Inhomogeneous Media," under preparation.

J.S. Chen, T.-H. Huang, H. Wei, and F. Beckwith, "MFreePDEs: Open-Source Implementation of Reproducing Kernel Particle Method for Solving Partial Differential Equations," under preparation.

H. Wei, J.S. Chen, F. Beckwith, "A Naturally Stabilized Semi-Lagrangian Meshfree Formulation for Multiphase Porous Media with Application to Landslide Modeling," *Journal of Engineering Mechanics*, submitted for publication.

D. Littlewood, M. Hillman, E. Yreux, J. Bishop, J.S. Chen, and F. Beckwith, "Implementation and verification of RKPM in the Sierra/SolidMechanics analysis code," ASME International Mechanical Engineering Congress and Exposition, Houston, Texas, 2015.

ABSTRACT OF THE DISSERTATION

An Immersed Reproducing Kernel Particle Method for Modeling Inhomogeneous Media

by

Frank Beckwith

Doctor of Philosophy in Structural Engineering

University of California San Diego, 2018

Professor Jiun-Shyan Chen, Chair

Structures involving multiple materials are difficult for meshfree methods to model accurately due to the strain discontinuity introduced at the material interface. An immersed Reproducing Kernel Particle Method (RKPM) approach is proposed to model inhomogeneous materials using an immersed domain approach to allow independent approximations and discretizations for the background matrix and the foreground inclusion. In this approach, Nitsche's method is introduced to enforce the interface compatibility conditions in a variationally consistent manner. The proposed method simplifies the spatial discretization procedures for multi-material problems involving complex geometries because the conforming requirements in discretization at the interface are avoided. Efficient and stable domain integration methods for the immersed

RKPM discretization are investigated, and the performance of several approaches are compared. Specifically, conforming and non-conforming domain integration between the foreground and background domains are discussed. Optimal convergence is achieved without tedious procedures such as enrichment functions or boundary singular kernels commonly employed in other meshfree methods for solving multi-material problems. Several numerical examples are presented to examine the effectiveness of the proposed method. A nonlinear formulation of the immersed RKPM method is also presented and its effectiveness in modeling brittle materials using an elastic-damage model is investigated.

Chapter 1

Introduction

1.1 Motivation

Meshfree methods are effective in constructing approximations with higher-order continuity and completeness with arbitrary point discretizations. Additionally, meshfree methods do not rely on an element mesh and construct the approximation using nodal information only. These features are attractive for modeling problems under large deformation due to loading from extreme events. However, modeling problems with multiple materials remains a challenging problem for meshfree simulations due to the presence of discontinuities in the strain field. Meshfree methods that are highly continuous are unable to capture such weak discontinuities and suffer from oscillations in the strain space due to Gibb's phenomenon unless enrichment functions with derivative discontinuities are introduced. Although the finite element method (FEM) can easily model strain discontinuities due its C^0 approximation, it suffers from issues due to mesh entanglement and element inversion under large deformation and requires costly remeshing.

Discretizing multi-material problems with complex geometries is also a tedious task if a conformal discretization with respect to the material interface is required. For FEM simulations, this can lead to distorted elements and introduce error into the approximation. Meshfree methods

appear to have an advantage since they do not require a conforming mesh but cannot properly approximate strain discontinuities at the material interface. Extrinsic enrichment techniques may be adopted to introduce weak discontinuities into the meshfree approximation. Such enrichment functions require nodal discretization that conforms to the material interface. They also introduce additional degrees of freedom corresponding to the amplitude of the strain jump which adds computational expense to the simulation. Intrinsic enriching avoids the additional degrees of freedom by building the derivative discontinuities into the basis functions of the meshfree approximation. However, the process still requires parameterization of the interface and can lead to ill-conditioning away from the enrichment location.

Problems with complex material geometries may arise, for example, in composite structures with multiple fibers that cross and intersect each other. These structures often encounter material damage in the matrix of the surrounding material due to extreme loading. The use of meshfree approximations without any treatment at the material interface may prematurely damage the matrix material due to oscillations occurring from Gibb's phenomenon. Additionally, FEM or other conformal methods fail to properly model these problems because of severe element distortion near the material interface. To this end, body-unfitted or immersed approaches that employ independent discretizations capable of capturing the weak discontinuity are desired.

1.2 Objectives

Despite several efforts made to improve meshfree approximations in the presence of material discontinuities, simulating multi-material problems with meshfree remains a challenging problem. The major objectives of this dissertation are as follows:

- Develop an immersed meshfree framework using Nitsche's method for interface compatibility. Immersed, or body-unfitted, approaches are intended to avoid a conformal discretization of the interface and utilize simple discretizations of the background and foreground materi-

als. This alleviates the discretization effort required for conformal techniques while still capturing the strain discontinuities through the use of independent approximations in the background and foreground discretizations.

- Formulate the immersed meshfree method which is compatible for arbitrary approximation functions for use with heterogeneous materials. Investigate and formulate accurate and stable numerical algorithms, including the Nitsche's penalty, the domain integration, the order of continuity in the background and foreground approximation functions, and their influence on the convergence rate of the numerical solution.

- Application of the immersed meshfree method to nonlinear problems with material damage without remeshing, moving mesh/point, or element death for problems with deformation dependent interface conditions such as interface debonding and material separation. Considerations with respect to domain and interface integration are discussed when nonlinear models are present. The use of Nitsche's method in nonlinear problems is also discussed.

1.3 Outline

The remainder of this dissertation is organized as follows. An overview of the current methods for solving multi-material problems with both body-fitted and body-unfitted approaches is presented in Chapter 2. The construction of the reproducing kernel approximation is presented in Chapter 3 in both continuous and discrete formats. A multi-dimensional notation is also introduced for constructing RK approximations in arbitrary dimensions. The mechanics of the multi-material problem and the formulation of the immersed method are given in Chapter 4. A fictitious domain is introduced for the immersed approach which serves to simplify the discretization of the total domain. Emphasis is placed on the use of simple discretizations for approximating the background and foreground domains and the ease of obtaining these discretizations. Integration methods for the immersed RKPM method are presented in Chapter 5. Different strategies for

populating integration points for use with the immersed approach is discussed. The immersed RKPM approach is applied to linear analysis and verified with several numerical examples in Chapter 6. In Chapter 7, the immersed RKPM approach is extended to heterogeneous problems with material nonlinearities. The linearization procedures are discussed and an example using an elastic-damage model is given. Chapter 8 summarizes this work and gives recommendations for future research.

Chapter 2

Literature Review

Meshfree methods, such as element free Galerkin (EFG) or reproducing kernel particle method (RKPM), have been shown to be versatile in constructing approximations with arbitrary order of continuity and polynomial completeness, where the order of continuity and completeness are decoupled from each other [12]. These features usually result in more accurate solutions and better resolved stress and strain fields than C^0 finite elements for smooth problems, and simplifies solution procedures for solving problems involving high-order spatial derivatives, such as thin shells and gradient damage modeling [16, 14]. Further, meshfree methods are effective for problems with excessive deformation where mesh-based methods often encounter difficulties due to mesh distortion or element entanglement [15]. On the other hand, for problems involving heterogeneous materials, the meshfree solutions exhibit severe spurious oscillations due to the smooth approximations with overlapping supports that cannot adequately realize the strain jump conditions across material interfaces. The C^0 finite elements naturally introduce a weak discontinuity in the strains across the material interface providing that a conforming mesh with respect to the material interface is generated. However, in bi-material problems involving complex geometries, such as reinforced concrete or composite materials, domain discretization with a conforming mesh along the material interfaces remains a challenging and tedious task.

To improve meshfree methods in capturing weak discontinuities, various approaches have been proposed, which broadly fall into two categories: body-fitted methods and body-unfitted methods, depending on whether or not the nodal distribution location conforms to the material interfaces [59]. Within the category of body-fitted methods, Cordes and Moran [23] attempted to apply a Lagrange multiplier method to enforce the interface jump conditions in the EFG discretization, but the derivative oscillations around the interface are encountered unless additional filtering schemes are adopted. Krongauz and Belytschko [50] enhanced the EFG shape functions using extrinsic enrichment with built-in discontinuities in their derivatives, while at the cost of introducing extra degrees of freedom associated with the amplitude of derivative jump. By exploiting the reproducing conditions, an intrinsic interface-enriched reproducing kernel approximation with embedded derivative discontinuities on the material interface was proposed in Wang, Chen, and Sun [80], which maintains the completeness without extra degrees of freedom. Lu, Kim, and Liu [61] proposed to capture weak discontinuities by truncating the window function and global partition polynomials, which keeps the advantage of both finite element methods and meshfree methods similar to that in the reproducing kernel element method [56].

2.1 Body-Unfitted Approaches

All the above-mentioned body-fitted methods require the discretization on the material interfacial geometry, which is an enhancement over the finite element typed conformal requirement. However, these approaches usually involve additional degrees of freedom, either extrinsically or intrinsically, and are considerably tedious for three dimensional, large-scale simulations of structures with complex material interface geometries (e.g., reinforced concrete structures embedded with numerous rebars and stirrups). Therefore, it is desirable to have a numerical scheme that allows the mesh/point distributions to be entirely independent to the underlying interface geometry. Along this line, various body-unfitted numerical methods have been developed, including *immersed*

boundary methods [36, 66, 2, 31, 24, 71, 65], *immersed finite element methods* [90, 89, 83, 82, 84], *embedded methods* [52, 60, 59], *fictitious domain methods* [5, 10, 11, 33, 88, 42, 47, 85], *finite cell methods* [29, 69], *Cartesian grid methods* [22, 25, 64, 48, 1, 67], and *extended/generalized finite element methods* [27, 28, 39, 78, 79].

In the extended/generalized finite element methods, partition-of-unity based extrinsic enrichment functions are introduced to enable the approximation to capture weak discontinuities without the need of a conforming mesh [8, 79, 78, 39]. In similar works [38, 27], a material interface is embedded into an underlying mesh and the weak discontinuity is achieved by some form of enrichment. These methods employ a level set function to identify the interface and subdivide or "cut" the intersected elements. To model the weak discontinuity, Nitsche's method [68] is normally employed. In [38, 39], Nitsche's method is used along an embedded interface with triangle elements. Nodes of elements cut by the interface are duplicated and their shape functions are modified such that they are positive on one side of the interface and zero on the other. In addition, a lower bound on the Nitsche parameter, γ, is given using an a priori analysis. In [27, 41], a closed-form expression for constant-strain triangles is given for γ using the inverse inequality. Annavarapu, Hautefeuille, and Dolbow [3] demonstrated the Nitsche parameter γ depends on the weighted average scheme used in the flux terms of Nitsche's method and proposes different weights based on the relative stiffness and size of the cut element to either side of the embedded interface. Jiang, Annavarapu, Dolbow, and Harari [45] extended the use of Nitsche's method for spline-based finite elements where a closed-form expression for γ cannot be obtained. Instead, the generalized inverse estimate is used on both sides of the interface to determine a lower bound for the interfacial weights. Other works have also employed Nitsche's method in conjunction with heirarchical *h*-refinement of the level set function to accurately define the interface and integration domains [53].

Body-unfitted approaches such as the immersed boundary and fictitious domain methods have been studied extensively in fluid-structure interaction (FSI) problems. In the fictitious domain

method developed in [49], a solid is immersed into a finite volume discretization and the no-slip condition is enforced on the interface. Using the distributed Lagrange multiplier method [35, 34], solid particulates surrounded by a fluid medium have been modeled. The immersed boundary (IB) method [70, 71] immerses solids in an Eulerian fluid domain and couples the two fields via discrete Dirac delta functions. A second-order accurate version of IB [51] was developed by employing a time-centered explicit integration scheme. An adaptive IB method [74] for improved accuracy was later introduced. These methods use a network of volume-less fibers to estimate the stresses in the solid. The extended immersed boundary method (EIBM) improves the accuracy by estimating stresses via a continuum solid using finite elements [81], and the discrete Dirac delta functions of the IB method are also replaced with reproducing kernel (RK) delta functions for arbitrary C^n continuity. Similarly, this idea was extended to model both the fluid and structure with elements in the immersed finite element method [90]. In the immersed finite element method [90, 89, 83, 82, 84], the immersed solid material is described with a deformable solid with finite volume. These methods have successfully been used towards heart valve simulations [72, 63, 44], wave propagation in cochlea [9], de-aggregation of red blood cell clusters [58], and recently to air-blast FSI [6].

For applications to inhomogeneous solid materials, the mortar element method [7] couples two non-conforming FEM approximations using Lagrange multipliers. The finite cell method [29, 69] relaxes the conforming requirement by extending the domain of the problem to a uniform grid of cells. Quadrature points outside of the physical domain are given softer material properties to approximate the actual geometry. This approach requires high-order quadrature near the boundary to accurately integrate the true strain energy. In a similar work [54, 55], a uniform grid of elements is used and the shape functions are modified along the interface to capture the jump condition. In [40], Nitsche's method is employed for "embedded mesh" problems where two separate discretizations overlap each other. The interface is defined as the collection of edges from the elements used to discretize the immersed inclusion. Background triangles intersecting

this interface are cut in order to appropriately integrate each subdomain. In [76], this method was extended to quadrilaterals to solve elasticity problems.

Despite the significant progress described above, studies on meshfree methods with body-unfitted techniques are still rare. Recently, Wu, Guo, and Askari [86] introduced an immersed meshfree formulation, which shows promising performance compared to body-fitted meshfree or conforming finite element discretizations, especially for large deformation problems [87]. In these works, the approximation functions are so constructed to impose continuity at the discrete nodal points along the material interface, usually achieved by the boundary singular kernel method or mixed transformation method [17]. As the resulting approximations generally do not conform to each other away from the discrete points on the interface, optimal convergence for bi-material problems are not guaranteed. In this work, an immersed RKPM approach is proposed where a "fictitious" zone is introduced in the background which overlaps the underlying inclusion and allows the background to be treated as a single, continuous body. Due to the independent discretizations and approximations in the background and foreground domains, jump conditions across the interface is achieved without the need of any enrichment schemes described in [50, 80]. In contrast to the earlier immersed meshfree formulation [86, 87], Nitsche's method is adopted in the present work to enforce the interface conditions, resulting in a computational framework that allows incorporation of different approximations in the background and foreground discretizations in a variationally consistent manner, and optimal convergence is achieved for modeling multi-materials problems without any tedious procedures described in [86, 87] for matching different approximations at interfaces.

Chapter 3

Reproducing Kernel Particle Method

3.1 Continuous Reproducing Kernel Approximation

Consider a field u in the domain Ω. The kernel estimate u^k of this field used in SPH is given by the following convolution integral.

$$u^k(x) = \int_\Omega \phi_a(x-s)u(s)\,\mathrm{d}s \tag{3.1}$$

ϕ_a is a kernel function with compact support given by a and is similar to the weighting function for a moving least squares (MLS) approximation. The kernel estimate is not complete for arbitrary polynomial orders. The RK approximation addresses this issue by introducing a correction function $C(x;x-s)$ into the kernel estimate such that the following approximation is complete up to polynomials of order n.

$$u^R(x) = \int_\Omega C(x;x-s)\phi_a(x-x)u(s)\,\mathrm{d}s \tag{3.2}$$

To this end, the following correction function first proposed in [57] is introduced.

$$C(x;x-s) = \sum_{i=0}^{n} (x-s)^i b_i(x) = \boldsymbol{H}^T(x-s)\boldsymbol{b}(x) \tag{3.3}$$

where $\boldsymbol{H}(x)$ is a basis vector of monomials:

$$\boldsymbol{H}^T(x-s) = \begin{bmatrix} 1 & x-s & (x-s)^2 & \cdots & (x-s)^n \end{bmatrix} \tag{3.4}$$

and $\boldsymbol{b}(x)$ is a set of moving coefficients that are as yet undetermined. Here, monomial basis functions have been used but others types of basis functions may be introduced as well. To determine the coefficients, a Taylor expansion of $u(s)$ is taken as follows:

$$u(s) = \sum_{i=0}^{\infty} \frac{(s-x)^i}{i!} u^{(i)}(x) \tag{3.5}$$

where $u^{(i)}(x)$ denotes the i^{th} derivative of the function $u(x)$. Substituting (3.3) and (3.5) into the RK approximation given by (3.2) above yields:

$$u^R(x) = \overline{m}_0(x)u(x) + \sum_{i=1}^{\infty} \frac{(-1)^i}{i!} \overline{m}_i(x) u^{(i)}(x) \tag{3.6}$$

where $\overline{m}_i(x)$ is the i^{th} moment of the corrected kernel $\overline{\phi}_a$ and is given as:

$$\overline{m}_i(x) = \int_{\Omega} (x-s)^i \boldsymbol{H}^T(x-s)\boldsymbol{b}(x)\phi_a(x-s)\,\mathrm{d}s \tag{3.7}$$

For the RK approximation $u^R(x)$ to achieve n^{th} order completeness, the first moment is taken as $\overline{m}_0(x) = 1$ and all other moments $\overline{m}_i(x) = 0$ for all i. These "reproducing conditions" lead to the following system of equations.

$$\boldsymbol{M}(x)\boldsymbol{b}(x) = \boldsymbol{H}(0) \tag{3.8}$$

where $\boldsymbol{M}(x)$ is a moment matrix given by

$$\boldsymbol{M}(x) = \begin{bmatrix} \overline{m}_0(x) & \overline{m}_1(x) & \cdots & \overline{m}_n(x) \\ \overline{m}_1(x) & \overline{m}_2(x) & \cdots & \overline{m}_{n+1}(x) \\ \vdots & \vdots & \ddots & \vdots \\ \overline{m}_n(x) & \overline{m}_{n+1}(x) & \cdots & \overline{m}_{2n}(x) \end{bmatrix} \tag{3.9}$$

or

$$\boldsymbol{M}(x) = \int_{\Omega} \boldsymbol{H}(x-s)\boldsymbol{H}^T(x-s)\phi_a(x-s)\,\mathrm{d}s \tag{3.10}$$

and the reproducing conditions are

$$\boldsymbol{H}^T(0) = \begin{bmatrix} 1 & 0 & \cdots & 0 \end{bmatrix} \tag{3.11}$$

$\boldsymbol{M}(x)$ is a Gram or moment matrix and as such is symmetric and positive definite. With (3.8) the vector $\boldsymbol{b}(x)$ is solved as follows:

$$\boldsymbol{b}(x) = \boldsymbol{M}^{-1}(x)\boldsymbol{H}(0) \tag{3.12}$$

Reintroducing the moving coefficients into (3.2), the continuous RK approximation is obtained.

$$\begin{aligned} u^R(x) &= \boldsymbol{H}^T(0)\boldsymbol{M}^{-1}(x)\int_{\Omega} \boldsymbol{H}(x-s)\phi_a(x-s)u(s)\,\mathrm{d}s \\ &= \int_{\Omega} \Psi(x;x-s)u(s)\,\mathrm{d}s \end{aligned} \tag{3.13}$$

where $\Psi(x;x-s)$ is known as the reproducing kernel approximation function given as follows:

$$\Psi(x;x-s) = \boldsymbol{H}(0)\boldsymbol{M}^{-1}(x)\boldsymbol{H}(x-s)\phi_a(x-s) \tag{3.14}$$

An alternative method for developing the continuous RK approximation is presented

in [18] by directly imposing reproducing conditions of the n^{th} polynomial to the RK approximation.

$$\int_{\Omega} C(x;x-s)\phi_a(x-s)s^i \,\mathrm{d}s = x^i, \quad i = 0,\cdots,n \tag{3.15}$$

(3.15) is equivalently expressed as

$$\int_{\Omega} C(x;x-s)\phi_a(x-s)(x-s)^i \,\mathrm{d}s = \delta_{0i}, \quad i = 0,\cdots,n \tag{3.16}$$

where δ_{0i} is the Kronecker delta function. Further rewriting the above and introducing the definition of the correction function from (3.3) earlier gives:

$$\left(\int_{\Omega} \boldsymbol{H}(x-s)\boldsymbol{H}^T(x-s)\phi_a(x-s)\,\mathrm{d}s\right)\boldsymbol{b}(x) = \boldsymbol{H}(0)$$

$$\boldsymbol{M}(x)\boldsymbol{b}(x) = \boldsymbol{H}(0) \tag{3.17}$$

which produces the same result and can be further utilized to arrive at the reproducing kernel $\Psi(x;x-s)$ as before.

As observed from (3.14), the reproducing kernel $\Psi(x;x-s)$ retains the continuity of the original kernel before correction; that is, if $\phi_a(x-s)$ belongs to C^k, so too does $\Psi(x;x-s)$. Also, the completeness of the reproducing kernel is completely independent of the original kernel continuity, unlike polynomial spline functions. An example of a kernel function ϕ_a is the cubic B-spline function given as:

$$\phi_a(x-s) = \begin{cases} \frac{2}{3} - 4z^2 + 4z^2 & 0 \le z \le 0.5 \\ \frac{4}{3} - 4z + 4z^2 - \frac{4}{3}z^3 & 0.5 \le z \le 1.0 \\ 0 & z > 1.0 \end{cases} \quad \text{where } z = \frac{|x-s|}{a} \tag{3.18}$$

3.2 Discrete Reproducing Kernel Approximation

The continuous form of the RK approximation must be discretized in order to construct an approximation function for a finite-dimensional solution of a set of partial differential equations. However, simply discretizing the continuous form in the previous section will violate the reproducing conditions and must be reformulated in a consistent manner for the discrete setting. Let S be a set of nodes x_I used to discretize the domain $\overline{\Omega}$ and $NP = \text{card}(S)$ be the total number of nodes.

$$S = \{I \mid x_I \in \overline{\Omega}\} \tag{3.19}$$

The discrete RK approximation is given as:

$$u^h(x) = \sum_{I \in S} C(x; x - x_I)\phi_a(x - x_I)u_I \tag{3.20}$$

where

$$C(x; x - x_I) = \boldsymbol{H}^T(x - x_I)\boldsymbol{b}(x) \tag{3.21}$$

Following [15], the discrete reproducing conditions are imposed as follows.

$$\sum_{I \in S} C(x; x - x_I)\phi_a(x - x_I)x_I^i = x^i, \quad i = 0, 1, \cdots, n \tag{3.22}$$

or equivalently

$$\sum_{I \in S} C(x; x - x_I)\phi_a(x - x_I)(x - x_I)^i = \delta_{0i}, \quad i = 0, 1, \cdots, n \tag{3.23}$$

Rewriting the above using (3.21), the following system of equations is obtained:

$$\sum_{I \in S} \boldsymbol{H}(x - x_I)\boldsymbol{H}^T(x - x_I)\phi_a(x - x_I)\boldsymbol{b}(x) = \boldsymbol{H}(0)$$

$$\boldsymbol{M}(x)\boldsymbol{b}(x) = \boldsymbol{H}(0) \tag{3.24}$$

where

$$\boldsymbol{M}(x) = \sum_{I \in S} \boldsymbol{H}(x - x_I)\boldsymbol{H}^T(x - x_I)\phi_a(x - x_I) \tag{3.25}$$

Once again by solving for the moving coefficients $\boldsymbol{b}(x)$ using (3.25) above and substituting into the discrete RK approximation in (3.20) results in the following.

$$u^h(x) = \sum_{I \in S} \boldsymbol{H}^T(0)\boldsymbol{M}^{-1}\boldsymbol{H}(x - x_I)\phi_a(x - x_I)u_I \equiv \sum_{I \in S} \Psi_I(x)u_I \tag{3.26}$$

where $\Psi_I(x)$ is the shape function at node I.

$$\boldsymbol{H}^T(0)\boldsymbol{M}^{-1}\boldsymbol{H}(x - x_I)\phi_a(x - x_I) \tag{3.27}$$

By construction of the RK approximation, the n^{th} order consistency condition is exactly satisfied.

3.3 Multi-dimensional RK Approximation

The discrete RK approximation in 1D may easily be extended to arbitrary dimension. Consider a domain $\Omega \in \mathbb{R}^d$ where d is the spatial dimension. The set S is redefined such that $S = \{I \mid \boldsymbol{x}_I \in \overline{\Omega}\}$. The RK approximation is now expressed as:

$$\boldsymbol{u}^h(\boldsymbol{x}) = \sum_{I \in S} C(\boldsymbol{x}; \boldsymbol{x} - \boldsymbol{x}_I)\phi_a(\boldsymbol{x} - \boldsymbol{x}_I)\boldsymbol{u}_I \tag{3.28}$$

where $\boldsymbol{x} = (x_1, x_2, \cdots, x_d)$. In what follows, a multi-index notation is employed where $\alpha = (\alpha_1, \alpha_2, \cdots, \alpha_d)$ denote the integer powers α_i for each x_i of a monomial $\boldsymbol{x}^\alpha \equiv x_1^{\alpha_1} x_2^{\alpha_2} \cdots x_d^{\alpha_d} = \Pi_{i=1}^d x_i^{\alpha_i}$. The length of the monomial order is given as $|\alpha| = \sum_{i=1}^d \alpha_i$. In (3.28) above, $C(\boldsymbol{x}; \boldsymbol{x} - \boldsymbol{x}_I)$ represents a correction function defined as the linear combination of monomials complete to

degree n.

$$C(\boldsymbol{x};\boldsymbol{x}-\boldsymbol{x}_I) \equiv \sum_{|\alpha|\leq n} (\boldsymbol{x}-\boldsymbol{x}_I)^{\alpha} b_{\alpha}(\boldsymbol{x}) = \boldsymbol{H}^T(\boldsymbol{x}-\boldsymbol{x}_I)\boldsymbol{b}(\boldsymbol{x}) \tag{3.29}$$

As before, $\boldsymbol{H}(\boldsymbol{x}-\boldsymbol{x}_I) = \{(\boldsymbol{x}-\boldsymbol{x}_I)^{\alpha}\}_{|\alpha|\leq n}$ represents a set of monomial basis functions. In three dimensions ($d=3$), the basis vector complete up to n^{th} order polynomials is given as:

$$\boldsymbol{H}^T(\boldsymbol{x}-\boldsymbol{x}_I) = \begin{bmatrix} 1 & x_1-x_{1I} & x_2-x_{2I} & x_3-x_{3I} & \cdots & (x_1-x_{1I})^n & \cdots (x_3-x_{3I})^n \end{bmatrix} \tag{3.30}$$

Again, the reproducing conditions are imposed to the multi-dimensional RK approximation to arrive at the following.

$$\sum_{I\in S} C(\boldsymbol{x};\boldsymbol{x}-\boldsymbol{x}_I)\phi_a(\boldsymbol{x}-\boldsymbol{x}_I)\boldsymbol{x}_I^{\alpha} = \boldsymbol{x}^{\alpha}, \quad |\alpha| \leq n \tag{3.31}$$

Equivalently,

$$\sum_{I\in S} \boldsymbol{H}(\boldsymbol{x}-\boldsymbol{x}_I)\boldsymbol{H}^T(\boldsymbol{x}-\boldsymbol{x}_I)\phi_a(\boldsymbol{x}-\boldsymbol{x}_I)\boldsymbol{b}(\boldsymbol{x}) = \boldsymbol{H}(\boldsymbol{0})$$

$$\boldsymbol{M}(\boldsymbol{x})\boldsymbol{b}(\boldsymbol{x}) = \boldsymbol{H}(\boldsymbol{0}) \tag{3.32}$$

where

$$\boldsymbol{M}(\boldsymbol{x}) = \sum_{I\in S} \boldsymbol{H}(\boldsymbol{x}-\boldsymbol{x}_I)\boldsymbol{H}^T(\boldsymbol{x}-\boldsymbol{x}_I)\phi_a(\boldsymbol{x}-\boldsymbol{x}_I) \tag{3.33}$$

Solving for the moving coefficient vector $\boldsymbol{b}(\boldsymbol{x})$ and substituting back into (3.28) in the usual manner results in the multi-dimensional RK approximation.

$$\boldsymbol{u}^h(\boldsymbol{x}) = \sum_{I\in S} \boldsymbol{H}^T(\boldsymbol{0})\boldsymbol{M}^{-1}(\boldsymbol{x})\boldsymbol{H}(\boldsymbol{x}-\boldsymbol{x}_I)\phi_a(\boldsymbol{x}-\boldsymbol{x}_I)\boldsymbol{u}_I \equiv \sum_{I\in S} \Psi_I(\boldsymbol{x})\boldsymbol{u}_I \tag{3.34}$$

$$\Psi_I(\boldsymbol{x}) = \boldsymbol{H}^T(\boldsymbol{0})\boldsymbol{M}^{-1}(\boldsymbol{x})\boldsymbol{H}(\boldsymbol{x}-\boldsymbol{x}_I)\phi_a(\boldsymbol{x}-\boldsymbol{x}_I) \tag{3.35}$$

In the definition of (3.35), the inverse of the moment matrix is taken and requires that the moment matrix is non-singular. In the continuous version, the moment matrix is guaranteed to be positive-definite, but this is not always the case in the discrete setting. To be able to evaluate an approximation function at a given point $\boldsymbol{x}$, the point is also required to be covered by at least m non-coplanar nodes, where m is the number of basis functions in $\boldsymbol{H}(\boldsymbol{x}-\boldsymbol{x}_I)$ and is given as:

$$m = \frac{(n+d)!}{n!d!} \tag{3.36}$$

In (3.28) through (3.35), the multi-dimensional kernel functions may be constructed by using the one-dimensional kernel as

$$\phi_a(\boldsymbol{x}-\boldsymbol{x}_I) = \Pi_{i=1}^{d}\phi_a(x_i - x_{iI}) = \phi_a(x_1 - x_{1I})\phi_a(x_2 - x_{2I})\cdots\phi_a(x_d - x_{dI}) \tag{3.37}$$

for a kernel with rectangular support; or

$$\phi_a(\boldsymbol{x}-\boldsymbol{x}_I) = \phi_a(z), \quad z = \frac{||\boldsymbol{x}-\boldsymbol{x}_I||}{a} \tag{3.38}$$

for a kernel with spherical support.

There are some notable properties of the RK approximation.

- As before in the continuous RK approximation, the RK kernel Ψ_I possesses the same order of continuity as the original kernel ϕ_a, while the consistency of the kernel is determined by the basis functions used in the correction function $C(\boldsymbol{x};\boldsymbol{x}-\boldsymbol{x}_I)$. Further, these two properties are independent of each other. This allows the RK approximation to be tailored to have a desired level of continuity for a particular problem.

- Although the RK approximation may be constructed with arbitrary completeness and continuity, the RK shape functions do not possess the Kronecker delta property, that is $\Psi_I(\boldsymbol{x}_J) \neq \delta_{IJ}$. This complicates the imposition of essential boundary conditions of the

governing partial differential equations. This topic is discussed in [17, 32].

- The RK approximation is constructed using nodal information only and does not require an element mesh. This obviates issues arising from mesh entanglement and also allows for a straightforward implementation of adaptive refinement.

- In addition to satisfying the consistency conditions, the derivatives of the RK approximation functions also satisfy the derivative reproducing conditions.

Chapter 4

Formulation of the immersed RKPM method

4.1 Problem Statement for Linear Elasticity

In this section, the governing equations and the weak form for use with the immersed reproducing kernel particle method. Consider an open domain Ω with an associated boundary $\Gamma = \Gamma^g \cup \Gamma^h$, where Γ^g denotes the essential boundary and Γ^h denotes the natural boundary. An illustration of the body is shown in Figure 4.1. The body, $\Omega = \Omega^1 \cup \Omega^2$, consists of two elastic solids with different material properties. Ω^1 defines a surrounding matrix with material constants E^1 and ν^1, and Ω^2 defines an inclusion with material constants E^2 and ν^2. The outer matrix and inclusions are connected via a material interface, Γ^I, over which traction equilibrium and displacement continuity must be satisfied. The body is subject to prescribed displacement, $\boldsymbol{g}$, acting over the essential boundary, Γ^g, and applied tractions, $\boldsymbol{h}$, acting over the natural boundary, Γ^h. Let the body force $\boldsymbol{b}^1$ act over the outer matrix, Ω^1, and the body force $\boldsymbol{b}^2$ act over the inclusion, Ω^2.

The bi-material problem is treated as two bodies taken separately and couple together at

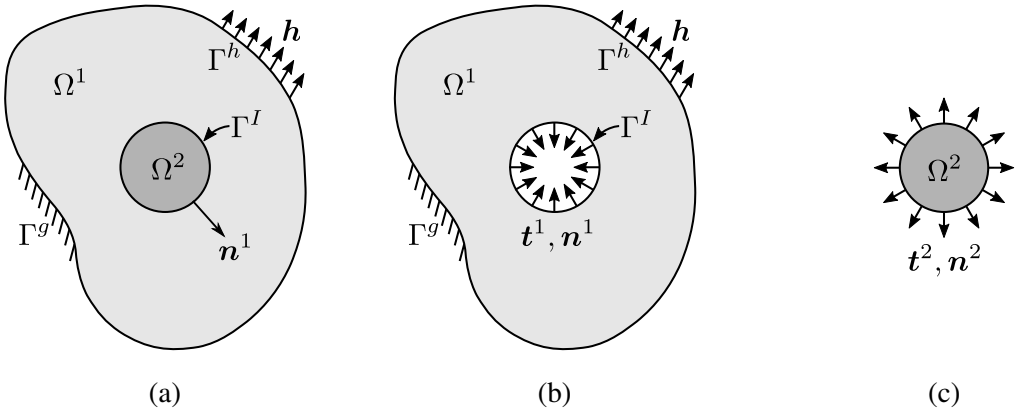

(a) (b) (c)

Figure 4.1: Inhomogeneous geometry. (a) Domain with circular inclusion; (b) Sub-domain of base matrix Ω^1; (c) Sub-domain of inclusion Ω^2

the material interface. The total potential energy of the bi-material problem is thus a combination of the potential energy from each subdomain. Without loss of generality, Lagrange multipliers $\boldsymbol{\tau}$ and $\boldsymbol{\lambda}$ are used to enforce the jump conditions on Γ^I and the essential boundary conditions on Γ^g, respectively. Treating $\boldsymbol{\lambda}$ and $\boldsymbol{\tau}$ as unknowns, the virtual work is then stated as follows: find $\boldsymbol{u}^1, \boldsymbol{u}^2 \in \mathcal{U}^1 \times \mathcal{U}^2$ such that

$$\begin{aligned}
\delta U = &\int_{\Omega^1} \delta\boldsymbol{\varepsilon}^1 : \boldsymbol{\sigma}^1 \,\mathrm{d}\Omega - \int_{\Omega^1} \delta\boldsymbol{u}^1 \cdot \boldsymbol{b}^1 \,\mathrm{d}\Omega - \int_{\Gamma^h} \delta\boldsymbol{u}^1 \cdot \boldsymbol{h} \,\mathrm{d}\Gamma \\
&+ \int_{\Omega^2} \delta\boldsymbol{\varepsilon}^2 : \boldsymbol{\sigma}^2 \,\mathrm{d}\Omega - \int_{\Omega^2} \delta\boldsymbol{u}^2 \cdot \boldsymbol{b}^2 \,\mathrm{d}\Omega \\
&- \int_{\Gamma^g} \delta\boldsymbol{u}^1 \cdot \boldsymbol{\lambda} \,\mathrm{d}\Gamma - \int_{\Gamma^g} \delta\boldsymbol{\lambda} \cdot \left(\boldsymbol{u}^1 - \boldsymbol{g}\right) \mathrm{d}\Gamma \\
&- \int_{\Gamma^I} \left(\delta\boldsymbol{u}^2 - \delta\boldsymbol{u}^1\right) \cdot \boldsymbol{\tau} \,\mathrm{d}\Gamma - \int_{\Gamma^I} \delta\boldsymbol{\tau} \cdot \left(\boldsymbol{u}^2 - \boldsymbol{u}^1\right) \mathrm{d}\Gamma = 0
\end{aligned} \tag{4.1}$$

for all $\delta\boldsymbol{u}^1, \delta\boldsymbol{u}^2 \in \mathcal{V}^1 \times \mathcal{V}^2$ where the test and trial spaces are defined as:

$$\mathcal{U}^i = \{\boldsymbol{u}^i \mid \boldsymbol{u}^i \in H_g^1(\Omega^i), \boldsymbol{u}^i = \boldsymbol{g} \text{ on } \Gamma^g\} \tag{4.2a}$$

$$\mathcal{V}^i = \{\delta\boldsymbol{u}^i \mid \delta\boldsymbol{u}^i \in H_0^1(\Omega^i), \delta\boldsymbol{u}^i = \boldsymbol{0} \text{ on } \Gamma^g\} \tag{4.2b}$$

for $i = 1,2$. The strain, $\boldsymbol{\varepsilon}$, is defined as the symmetric gradient of displacement

$$\boldsymbol{\varepsilon}^i = \frac{1}{2}\left(\nabla \otimes \boldsymbol{u}^i + \boldsymbol{u}^i \otimes \nabla\right) \tag{4.3}$$

and the stress is the given by $\boldsymbol{\sigma}^i = \boldsymbol{C}^i : \boldsymbol{\varepsilon}^i$ where $\boldsymbol{C}^i$ is the modulus tensor for material i.

The first line of (4.1) above corresponds to the virtual work δU^1 of subdomain Ω^1, the second line corresponds to the virtual work δU^2 of subdomain Ω^2, the third line enforces essential boundary conditions using the Lagrange multiplier $\boldsymbol{\lambda}$, and the fourth line enforces the interface conditions using the Lagrange multiplier $\boldsymbol{\tau}$. Note that the essential boundary conditions must be explicitly enforced with Lagrange multipliers for RKPM because the RK approximation does not possess the Kronecker delta property and in general is not interpolatory over Γ^g [17].

To deduce the physical interpretation of the Lagrange multipliers $\boldsymbol{\lambda}$ and $\boldsymbol{\tau}$, the product rule of differentiation is applied to the internal energy terms in (4.1) followed by divergence theorem to obtain the Euler-Lagrange equations corresponding to the virtual work. The Euler-Lagrange equations are given as

$$\begin{aligned}
\delta U = &- \int_{\Omega^1} \delta\boldsymbol{u}^1 \cdot \left(\nabla \cdot \boldsymbol{\sigma}^1 + \boldsymbol{b}^1\right) \mathrm{d}\Omega + \int_{\Gamma^h} \delta\boldsymbol{u}^1 \cdot \left(\boldsymbol{\sigma}^1 \cdot \boldsymbol{n}^1 - \boldsymbol{h}\right) \mathrm{d}\Gamma + \int_{\Gamma^g} \delta\boldsymbol{u}^1 \cdot \left(\boldsymbol{\sigma}^1 \cdot \boldsymbol{n}^1 - \boldsymbol{\lambda}\right) \mathrm{d}\Gamma \\
&+ \int_{\Gamma^I} \delta\boldsymbol{u}^1 \cdot \left(\boldsymbol{\sigma}^1 \cdot \boldsymbol{n}^1 + \boldsymbol{\tau}\right) \mathrm{d}\Gamma - \int_{\Omega^2} \delta\boldsymbol{u}^2 \cdot \left(\nabla \cdot \boldsymbol{\sigma}^2 + \boldsymbol{b}^2\right) \mathrm{d}\Omega + \int_{\Gamma^I} \delta\boldsymbol{u}^2 \cdot \left(\boldsymbol{\sigma}^2 \cdot \boldsymbol{n}^2 - \boldsymbol{\tau}\right) \mathrm{d}\Gamma \\
&- \int_{\Gamma^g} \delta\boldsymbol{\lambda} \cdot \left(\boldsymbol{u}^1 - \boldsymbol{g}\right) \mathrm{d}\Gamma - \int_{\Gamma^I} \delta\boldsymbol{\tau} \cdot \left(\boldsymbol{u}^2 - \boldsymbol{u}^1\right) \mathrm{d}\Gamma = 0
\end{aligned} \tag{4.4}$$

Because the variations $\delta\boldsymbol{u}^i$, $\delta\boldsymbol{\lambda}$, and $\delta\boldsymbol{\tau}$ are arbitrary, all the terms surrounded by parentheses must identically be equal to zero. It can be seen that the physical interpretation of the Lagrange multipliers $\boldsymbol{\lambda}$ and $\boldsymbol{\tau}$ are the tractions acting on the essential boundary Γ^g and the material interface Γ^I, respectively. It is important to note that $\boldsymbol{\tau} = -\boldsymbol{\sigma}^1 \cdot \boldsymbol{n}^1 = \boldsymbol{\sigma}^2 \cdot \boldsymbol{n}^2$. This indicates the traction produced by the surrounding matrix is equal and opposite to the traction produced by inclusion at the material interface. Noting the outward normals acting on the material interface are also equal

and opposite to each other, a single normal $\boldsymbol{n} = \boldsymbol{n}^1 = -\boldsymbol{n}^2$ is taken. Using this definition, the governing equations describing linear elasticity for the multi-material problem are deduced from the Euler-Lagrange equations above.

$$\nabla \cdot \boldsymbol{\sigma}^1 + \boldsymbol{b}^1 = \boldsymbol{0} \quad \text{in} \quad \Omega^1 \tag{4.5a}$$

$$\nabla \cdot \boldsymbol{\sigma}^2 + \boldsymbol{b}^2 = \boldsymbol{0} \quad \text{in} \quad \Omega^2 \tag{4.5b}$$

$$\boldsymbol{\sigma}^1 \cdot \boldsymbol{n} = \boldsymbol{h} \quad \text{on} \quad \Gamma^{\boldsymbol{h}} \tag{4.5c}$$

$$\boldsymbol{u}^1 = \boldsymbol{g} \quad \text{on} \quad \Gamma^{\boldsymbol{g}} \tag{4.5d}$$

$$\boldsymbol{\sigma}^1 \cdot \boldsymbol{n} = \boldsymbol{\lambda} \quad \text{on} \quad \Gamma^{\boldsymbol{g}} \tag{4.5e}$$

$$[\![\boldsymbol{u}]\!] = \boldsymbol{0} \quad \text{on} \quad \Gamma^I \tag{4.5f}$$

$$[\![\boldsymbol{\sigma} \cdot \boldsymbol{n}]\!] = \boldsymbol{0} \quad \text{on} \quad \Gamma^I \tag{4.5g}$$

Note the use of the jump operator $[\![\cdot]\!] = (\cdot)^2 - (\cdot)^1$ which is used to describe displacement continuity and traction equilibrium in (4.5f) and (4.5g), respectively. The governing equations above describe a perfectly bonded interface but can be easily extended to include a cohesion term which admits compliance proportional to the traction experienced at the material interface, Γ^I.

The Lagrange multiplier method, while general, is cumbersome to apply directly as one must solve for the unknowns $\boldsymbol{\lambda}$ and $\boldsymbol{\tau}$. In addition, it suffers from instabilities such as pressure modes if the inf-sup condition is not met. To avoid these issues, the Lagrange multipliers are redefined according to their physical interpretation similar to the modified variational principle [62].

$$\boldsymbol{\lambda} = \boldsymbol{\sigma} \cdot \boldsymbol{n} - \frac{\beta}{2} \cdot \left(\boldsymbol{u}^1 - \boldsymbol{g}\right) \tag{4.6a}$$

$$\boldsymbol{\tau} = \langle \boldsymbol{\sigma} \rangle \cdot \boldsymbol{n} - \frac{\gamma}{2} \cdot [\![\boldsymbol{u}]\!] \tag{4.6b}$$

The notation $\langle\cdot\rangle = \alpha^1 (\cdot)^1 + \alpha^2 (\cdot)^2$ has been used to indicate a weighted average operator. This is used to average the flux terms above for the definition of $\boldsymbol{\tau}$. Substituting these definitions into (4.1) for $\boldsymbol{\lambda}$ and $\boldsymbol{\tau}$ results in the well known Nitsche's method [68].

$$\begin{aligned}\delta U = &\int_{\Omega^1} \delta\varepsilon^1 : \boldsymbol{\sigma}^1 \,\mathrm{d}\Omega + \int_{\Omega^2} \delta\varepsilon^2 : \boldsymbol{\sigma}^2 \,\mathrm{d}\Omega - \int_{\Omega^1} \delta\boldsymbol{u}^1 \cdot \boldsymbol{b}^1 \,\mathrm{d}\Omega - \int_{\Omega^2} \delta\boldsymbol{u}^2 \cdot \boldsymbol{b}^2 \,\mathrm{d}\Omega \\ &- \int_{\Gamma^h} \delta\boldsymbol{u}^1 \cdot \boldsymbol{h} \,\mathrm{d}\Gamma - \int_{\Gamma^g} \delta\boldsymbol{\sigma}^1 \cdot \boldsymbol{n}^1 \cdot \boldsymbol{u}^1 \,\mathrm{d}\Gamma - \int_{\Gamma^g} \delta\boldsymbol{u}^1 \cdot \boldsymbol{\sigma}^1 \cdot \boldsymbol{n}^1 \,\mathrm{d}\Gamma + \beta \int_{\Gamma^g} \delta\boldsymbol{u}^1 \cdot \boldsymbol{u}^1 \,\mathrm{d}\Gamma \\ &+ \int_{\Gamma^g} \delta\boldsymbol{\sigma}^1 \cdot \boldsymbol{n}^1 \cdot \boldsymbol{g} \,\mathrm{d}\Gamma - \beta \int_{\Gamma^g} \delta\boldsymbol{u}^1 \cdot \boldsymbol{g} \,\mathrm{d}\Gamma + \int_{\Gamma^I} [\![\delta\boldsymbol{u}]\!] \cdot \langle\boldsymbol{\sigma}\rangle \cdot \boldsymbol{n}^1 \,\mathrm{d}\Gamma \\ &+ \int_{\Gamma^I} \langle\delta\boldsymbol{\sigma}\rangle \cdot \boldsymbol{n}^1 \cdot [\![\boldsymbol{u}]\!] \,\mathrm{d}\Gamma + \gamma \int_{\Gamma^I} [\![\delta\boldsymbol{u}]\!] \cdot [\![\boldsymbol{u}]\!] \,\mathrm{d}\Gamma = 0\end{aligned} \tag{4.7}$$

In the above, β and γ are penalty-like terms for the imposition of essential boundary conditions and interface conditions, respectively. It has been shown that these stabilization terms must be selected sufficiently large to ensure coercivity with Nitsche's method [39, 41]. A choice of $\beta > C$ and $\gamma > C$ for a mesh-dependent constant C ensures the following coercivity function is met.

$$a(\boldsymbol{v}^h, \boldsymbol{v}^h) \geq C||\boldsymbol{v}^h|| \tag{4.8}$$

where $a(\cdot,\cdot)$ is the bi-linear strain energy operator corresponding to the weak form. The question remains how to determine C so that an appropriate set of stabilization terms may be selected.

The choice of α^1 and α^2 has been studied extensively for application to embedded interfaces with linear tetrahedra [3, 4]. There, the coercivity of the system and thus the choice of the value γ was shown to be dependent on the weights α^1 and α^2. A scheme for selecting the weights was proposed based on the material modulus and the volume of the element intersected by an interface. The analysis is based off of constant-strain tetrahedral elements which admits an analytical solution for the coercivity. A later work extended the analysis to spline-based elements by leveraging the inverse inequality [45]. In the present work, the RK approximation is used

and the aforementioned studies based off of finite element approximations do not apply. For simplicity, a one-sided flux of $\alpha^1 = 1$ and $\alpha^2 = 0$ has been chosen.

4.2 Immersed Method by the Fictitious Domain Approach

The above weak form is still expressed as separate integrals over the individual subdomains Ω^1 and Ω^2. With complex geometries, tedious discretization of each subdomain with respect to the material interface is required to solve the weak form using the Galerkin method. To simplify the task of discretization, a fictitious domain which occupies the same space as the "foreground" inclusion is introduced. The internal energy of this fictitious material is then added and subtracted from the weak form and the internal energy is modified as follows:

$$\delta W^{int} = \int_{\Omega^1} \delta\varepsilon^1 : \boldsymbol{\sigma}^1 \, \mathrm{d}\Omega + \int_{\Omega^2} \delta\varepsilon^2 : \boldsymbol{\sigma}^2 \, \mathrm{d}\Omega + \int_{\Omega^2} \delta\varepsilon^1 : \boldsymbol{\sigma}^1 \, \mathrm{d}\Omega - \int_{\Omega^2} \delta\varepsilon^1 : \boldsymbol{\sigma}^1 \, \mathrm{d}\Omega \tag{4.9}$$

The last two terms of (4.9) correspond to the contributions of the fictitious domain to the internal energy. By adding the first and third integrals, a total domain integral of the "background" energy is obtained. The second and fourth integrals may also be combined to yield the following:

$$\delta W^{int} = \int_{\Omega} \delta\varepsilon^1 : \boldsymbol{\sigma}^1 \, \mathrm{d}\Omega + \int_{\Omega^2} \left(\delta\varepsilon^2 : \boldsymbol{\sigma}^2 - \delta\varepsilon^1 : \boldsymbol{\sigma}^1 \right) \mathrm{d}\Omega \tag{4.10}$$

The internal energy is now approximated by a total domain integral over the background matrix material and the difference in internal energy between the inclusion and fictitious domains. We refer to $\int_{\Omega^2} \delta\varepsilon^1 : \boldsymbol{\sigma}^1 \, \mathrm{d}\Omega$ as the fictitious term in the (4.10). With the above, the total domain Ω may be discretized using simple techniques in such a way that is not required to conform to the material interface. In addition, the discretization of the background and foreground domains are independent of each other. By the same procedure, the external energy from body forces may

also be combined as follows:

$$\delta W^{ext} = \int_{\Omega} \delta \boldsymbol{u}^1 \cdot \boldsymbol{b}^1 \, \mathrm{d}\Omega + \int_{\Omega^2} \left(\delta \boldsymbol{u}^2 \cdot \boldsymbol{b}^2 - \delta \boldsymbol{u}^1 \cdot \boldsymbol{b}^1 \right) \mathrm{d}\Omega \tag{4.11}$$

where the term $\int_{\Omega^2} \delta \boldsymbol{u}^1 \cdot \boldsymbol{b}^1 \, \mathrm{d}\Omega$ is also a fictitious term.

Using (4.10) and (4.11), the weak form of (4.7) may be re-expressed to yield the weak form for the immersed procedure using Nitsche's method.

$$\delta U = \delta W^{int} - \delta W^{ext} + \delta U^I + \delta U^{EB} = 0 \tag{4.12a}$$

$$\delta W^{int} = \int_{\Omega} \delta \boldsymbol{\varepsilon}^1 : \boldsymbol{\sigma}^1 \, \mathrm{d}\Omega + \int_{\Omega^2} \left(\delta \boldsymbol{\varepsilon}^2 : \boldsymbol{\sigma}^2 - \delta \boldsymbol{\varepsilon}^1 : \boldsymbol{\sigma}^1 \right) \mathrm{d}\Omega \tag{4.12b}$$

$$\delta U^I = -\int_{\Gamma^I} [\![\delta \boldsymbol{u}]\!] \cdot \langle \boldsymbol{\sigma} \rangle \cdot \boldsymbol{n}^1 \, \mathrm{d}\Gamma - \int_{\Gamma^I} \langle \delta \boldsymbol{\sigma} \rangle \cdot \boldsymbol{n}^1 \cdot [\![\boldsymbol{u}]\!] \, \mathrm{d}\Gamma + \gamma \int_{\Gamma^I} [\![\delta \boldsymbol{u}]\!] \cdot [\![\boldsymbol{u}]\!] \, \mathrm{d}\Gamma \tag{4.12c}$$

$$\delta W^{ext} = \int_{\Omega} \delta \boldsymbol{u}^1 \cdot \boldsymbol{b}^1 \, \mathrm{d}\Omega + \int_{\Omega^2} \left(\delta \boldsymbol{u}^2 \cdot \boldsymbol{b}^2 - \delta \boldsymbol{u}^1 \cdot \boldsymbol{b}^1 \right) \mathrm{d}\Omega + \int_{\Gamma^h} \delta \boldsymbol{u}^1 \cdot \boldsymbol{h} \, \mathrm{d}\Gamma \tag{4.12d}$$

$$\begin{aligned} \delta U^{EB} = &-\int_{\Gamma^g} \delta \boldsymbol{\sigma}^1 \cdot \boldsymbol{n}^1 \cdot \boldsymbol{u}^1 \, \mathrm{d}\Gamma - \int_{\Gamma^g} \delta \boldsymbol{u}^1 \cdot \boldsymbol{\sigma}^1 \cdot \boldsymbol{n}^1 \, \mathrm{d}\Gamma + \beta \int_{\Gamma^g} \delta \boldsymbol{u}^1 \cdot \boldsymbol{u}^1 \, \mathrm{d}\Gamma \\ &+ \int_{\Gamma^g} \delta \boldsymbol{\sigma}^1 \cdot \boldsymbol{n}^1 \cdot \boldsymbol{g} \, \mathrm{d}\Gamma - \beta \int_{\Gamma^g} \delta \boldsymbol{u}^1 \cdot \boldsymbol{g} \, \mathrm{d}\Gamma \end{aligned} \tag{4.12e}$$

In the above, all subdomain integrals over Ω^1 have been converted into total domain integrals over Ω, which eases the discretization over the background. The foreground domain Ω^2 must still be discretized according to the geometry of the inclusion, but this may now be done independently of the background discretization.

4.3 Discretization of Immersed RKPM

In the following sections, an immersed approach is introduced in which the total domain $\overline{\Omega} = \overline{\Omega}^1 \cup \overline{\Omega}^2$ and the inclusion over $\overline{\Omega}^2$ are independently discretized. The discretization of the inclusion Ω^2 is then immersed or overset on top of the background discretization over $\overline{\Omega}$. This allows for a straightforward discretization of the total domain because it avoids the complexity

of the interface compared to discretizing the individual subdomain $\overline{\Omega}^1$. Because the inclusion is not required to conform with the background, the discretization of the inclusion domain $\overline{\Omega}^2$ is also greatly simplified. In the following, a simple discretization strategy is considered with the immersed concept based on the weak form in (4.12).

RKPM is chosen to approximate the solution field for potential future applications to large deformation problems where mesh based methods could encounter mesh distortion or entanglement issues. The weak form allows nodes from the point discretization of $\overline{\Omega}^2$ to be inserted into $\overline{\Omega}$, leading to a number of discretization strategies. To demonstrate, consider a square domain with a circular inclusion as depicted in Figure 4.2.

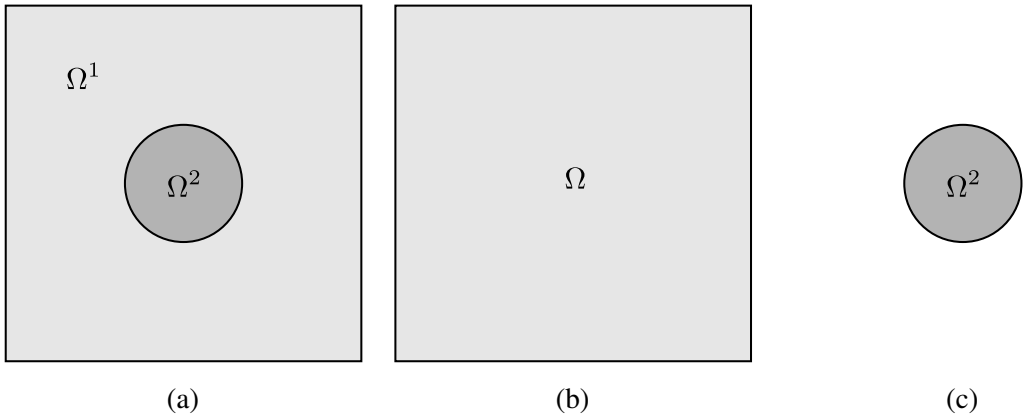

Figure 4.2: Square domain with circular inclusion. (a) The original domain; (b) the background (total) domain; and (c) the foreground domain

Let S be a set of points $\boldsymbol{x}_I$ used to discretize the total domain $\overline{\Omega} = \overline{\Omega}^1 \cup \overline{\Omega}^2$, and $NP = \text{card}(S)$ be the number of nodal points used to discretize $\overline{\Omega}$. Similarly, let $\tilde{S}$ be a set of points used to discretize the domain $\overline{\Omega}^2$, and $\tilde{NP} = \text{card}(\tilde{S})$ represent the number of nodal points in $\overline{\Omega}^2$. The point sets S and $\tilde{S}$ may be generated independently of each other. The two point sets S and $\tilde{S}$ are defined in (4.13a) and (4.13b) and are depicted in Figure 4.3. To discretize the fictitious domain, a set of fictitious points $\hat{S} \subset S$ is defined such that the domain of influence of each point $\boldsymbol{x}_I \in \hat{S}$ intersects only with the sub-domain $\overline{\Omega}^2$, given by (4.13c). This point set will be explained

in greater detail in Section 4.3.1.

$$S = \left\{ I \,|\, \boldsymbol{x}_I \in \overline{\Omega} \right\} \tag{4.13a}$$

$$\tilde{S} = \left\{ I \,|\, \tilde{\boldsymbol{x}}_I \in \overline{\Omega}^2 \right\} \tag{4.13b}$$

$$\hat{S} = \left\{ I \,|\, I \in S, \mathrm{supp}(\phi_a(\boldsymbol{x} - \boldsymbol{x}_I)) \cap \Omega^2 \neq \emptyset \right\} \tag{4.13c}$$

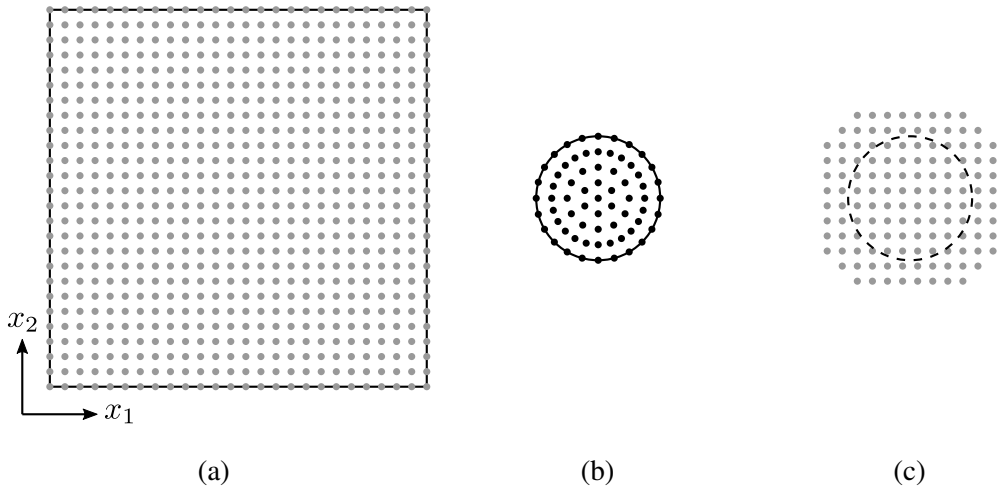

Figure 4.3: Simple discretization strategy. (a) Discretization of $\overline{\Omega}$ in set S; (b) discretization of $\overline{\Omega}^2$ in set $\tilde{S}$; and (c) discretization of fictitious domain in set $\hat{S}$.

The subdomain $\overline{\Omega}^1$ is no longer used due to its discretization complexity and is replaced instead with the total domain with the discretization described above. Once the point sets S and $\tilde{S}$ for the background and foreground domains have been determined, the approximations to the background and foreground displacement fields $\boldsymbol{u}^1$ and $\boldsymbol{u}^2$ are then constructed according to (3.34), discussed next.

4.3.1 Galerkin equation for immersed RKPM

In the following, RK approximations will be introduced in the discretization of background and foreground domains considering the appropriate monomial reproducing conditions. In (4.12b) and (4.12d), the discretizations of the background terms, $\int_\Omega \delta\boldsymbol{\varepsilon}^1 : \boldsymbol{\sigma}^1 \, \mathrm{d}\Omega$ and $\int_\Omega \delta\boldsymbol{u}^1 \cdot \boldsymbol{b}^1 \, \mathrm{d}\Omega$, are

carried out by using the background discrete points in S by

$$\int_\Omega \delta\varepsilon^1 : \boldsymbol{\sigma}^1 \, \mathrm{d}\Omega \approx \int_\Omega \delta\boldsymbol{\varepsilon}(\boldsymbol{u}^h) : \boldsymbol{\sigma}(\boldsymbol{\varepsilon}(\boldsymbol{u}^h), E^1, \nu^1) \, \mathrm{d}\Omega \tag{4.14a}$$

$$\int_\Omega \delta\boldsymbol{u}^1 \cdot \boldsymbol{b}^1 \, \mathrm{d}\Omega \approx \int_\Omega \delta\boldsymbol{u}^h \cdot \boldsymbol{b}^1 \, \mathrm{d}\Omega \tag{4.14b}$$

where

$$\boldsymbol{u}^h(\boldsymbol{x}) = \sum_{I \in S} \Psi_I(\boldsymbol{x}) \boldsymbol{u}_I, \quad \boldsymbol{x} \in \overline{\Omega} \tag{4.15}$$

Here, the RK shape functions $\{\Psi_I(\boldsymbol{x})\}_{I \in S}$ are constructed so that they meet the reproducing conditions in $\overline{\Omega}$, that is

$$\sum_{I \in S} \Psi_I(\boldsymbol{x}) \boldsymbol{x}_I^\alpha = \boldsymbol{x}^\alpha, \quad \forall \boldsymbol{x} \in \overline{\Omega}, \quad |\alpha| \leq n \tag{4.16}$$

As before, multi-dimensional notation has been employed as described earlier in Section 3.3.

Similarly, the discretization of the terms in (4.12b) and (4.12d) corresponding to the inclusion, $\int_{\Omega^2} \delta\varepsilon^2 : \boldsymbol{\sigma}^2 \, \mathrm{d}\Omega$ and $\int_{\Omega^2} \delta\boldsymbol{u}^2 \cdot \boldsymbol{b}^2 \, \mathrm{d}\Omega$, are performed by using the foreground discrete points in $\tilde{S}$ by

$$\int_{\Omega^2} \delta\varepsilon^2 : \boldsymbol{\sigma}^2 \, \mathrm{d}\Omega \approx \int_{\Omega^2} \delta\boldsymbol{\varepsilon}(\tilde{\boldsymbol{u}}^h) : \boldsymbol{\sigma}(\boldsymbol{\varepsilon}(\tilde{\boldsymbol{u}}^h), E^2, \nu^2) \, \mathrm{d}\Omega \tag{4.17a}$$

$$\int_{\Omega^2} \delta\boldsymbol{u}^2 \cdot \boldsymbol{b}^2 \, \mathrm{d}\Omega \approx \int_{\Omega^2} \delta\tilde{\boldsymbol{u}}^h \cdot \boldsymbol{b}^2 \, \mathrm{d}\Omega \tag{4.17b}$$

where

$$\tilde{\boldsymbol{u}}^h(\boldsymbol{x}) = \sum_{I \in \tilde{S}} \tilde{\Psi}_I(\boldsymbol{x}) \tilde{\boldsymbol{u}}_I, \quad \boldsymbol{x} \in \overline{\Omega}^2 \tag{4.18}$$

Here, the shape functions $\{\tilde{\Psi}_I(\boldsymbol{x})\}_{I \in \tilde{S}}$ are constructed so that they meet the reproducing conditions

in $\overline{\Omega}^2$, that is

$$\sum_{I\in\tilde{S}} \tilde{\Psi}_I(\boldsymbol{x})\boldsymbol{x}_I^{\alpha} = \boldsymbol{x}^{\alpha}, \quad \forall \boldsymbol{x} \in \overline{\Omega}^2, \quad |\alpha| \leq n \tag{4.19}$$

Next, the discretization of the fictitious terms in (4.12b) and (4.12d), $\int_{\Omega^2} \delta\boldsymbol{\varepsilon}^1 : \boldsymbol{\sigma}^1 \, \mathrm{d}\Omega$ and $\int_{\Omega^2} \delta\boldsymbol{u}^1 \cdot \boldsymbol{b}^1 \, \mathrm{d}\Omega$, are performed by using a subset of the background discrete points described in $\hat{S}$. The approximation of the fictitious terms is given by:

$$\int_{\Omega^2} \delta\boldsymbol{\varepsilon}^1 : \boldsymbol{\sigma}^1 \, \mathrm{d}\Omega \approx \int_{\Omega^2} \delta\boldsymbol{\varepsilon}(\hat{\boldsymbol{u}}^h) : \boldsymbol{\sigma}(\boldsymbol{\varepsilon}(\hat{\boldsymbol{u}}^h), E^1, \nu^1) \, \mathrm{d}\Omega \tag{4.20a}$$

$$\int_{\Omega^2} \delta\boldsymbol{u}^1 \cdot \boldsymbol{b}^1 \, \mathrm{d}\Omega \approx \int_{\Omega^2} \delta\hat{\boldsymbol{u}}^h \cdot \boldsymbol{b}^1 \, \mathrm{d}\Omega \tag{4.20b}$$

where

$$\hat{\boldsymbol{u}}^h(\boldsymbol{x}) = \sum_{I\in\hat{S}} \hat{\Psi}_I(\boldsymbol{x})\hat{\boldsymbol{u}}_I, \quad \boldsymbol{x} \in \overline{\Omega}^2 \tag{4.21}$$

In the above, a new set of shape functions $\{\hat{\Psi}_I\}_{I\in\hat{S}}$ is defined over a set of points $\hat{S} \subset S$. In the current formulation, $\{\hat{\Psi}_I\}_{I\in\hat{S}} = \{\Psi_I(\boldsymbol{x}) \,|\, \mathrm{supp}(\Psi_I(\boldsymbol{x})) \cap \Omega^2 \neq \emptyset\}$ is taken as a subset of the shape functions defined over S. This serves as the approximation space for the fictitious terms utilized in the immersed procedure.

For the interface terms in (4.12c), the approximation for $\boldsymbol{u}^1$ and $\boldsymbol{u}^2$ follow the background and foreground discretizations in (4.15) and (4.18), that is

$$\int_{\Gamma^I} [\![\delta\boldsymbol{u}]\!] \cdot \langle\boldsymbol{\sigma}\rangle \cdot \boldsymbol{n}^1 \, \mathrm{d}\Gamma \approx \int_{\Gamma^I} \left(\delta\tilde{\boldsymbol{u}}^h - \delta\boldsymbol{u}^h\right) \cdot \left(\alpha^1\boldsymbol{\sigma}(\boldsymbol{\varepsilon}^h, E^1, \nu^1) + \alpha^2\boldsymbol{\sigma}(\tilde{\boldsymbol{\varepsilon}}^h, E^2, \nu^2)\right) \cdot \boldsymbol{n}^1 \, \mathrm{d}\Gamma \tag{4.22a}$$

$$\int_{\Gamma^I} \langle\delta\boldsymbol{\sigma}\rangle \cdot \boldsymbol{n}^1 \cdot [\![\boldsymbol{u}]\!] \, \mathrm{d}\Gamma \approx \int_{\Gamma^I} \left(\alpha^1\boldsymbol{\sigma}(\delta\boldsymbol{\varepsilon}^h, E^1, \nu^1) + \alpha^2\boldsymbol{\sigma}(\delta\tilde{\boldsymbol{\varepsilon}}^h, E^2, \nu^2)\right) \cdot \boldsymbol{n}^1 \cdot \left(\tilde{\boldsymbol{u}}^h - \boldsymbol{u}^h\right) \mathrm{d}\Gamma \tag{4.22b}$$

$$\gamma \int_{\Gamma^I} [\![\delta\boldsymbol{u}]\!] \cdot [\![\boldsymbol{u}]\!] \, \mathrm{d}\Gamma \approx \gamma \int_{\Gamma^I} \left(\delta\tilde{\boldsymbol{u}}^h - \delta\boldsymbol{u}^h\right) \cdot \left(\tilde{\boldsymbol{u}}^h - \boldsymbol{u}^h\right) \mathrm{d}\Gamma \tag{4.22c}$$

where $\boldsymbol{\varepsilon}^h = \boldsymbol{\varepsilon}(\boldsymbol{u}^h)$ and $\tilde{\boldsymbol{\varepsilon}}^h = \boldsymbol{\varepsilon}(\tilde{\boldsymbol{u}}^h)$.

The formulations above do not require that the shape functions conform along the interface as that introduced in [86]. In fact, the approximation functions Ψ_I, $\tilde{\Psi}_I$, $\hat{\Psi}_I$ are generated independently from each other and do not conform in general. It is possible to use the above formulation where the background and foreground approximations are equal, but requires more effort to discretize. In the more general case where $\boldsymbol{u}^h \neq \tilde{\boldsymbol{u}}^h$ for $\boldsymbol{x} \in \Omega^2$, that is using background discretization S in (4.13a) and foreground discretization $\tilde{S}$ in (4.13b), all of the interface terms in (4.12a) to (4.12e) must be included.

$$\delta W^{int} = \int_{\Omega} \delta\varepsilon(\boldsymbol{u}^h) : \boldsymbol{\sigma}(\varepsilon(\boldsymbol{u}^h), E^1, \nu^1)\, \mathrm{d}\Omega \tag{4.23a}$$
$$+ \int_{\Omega^2} \Big(\delta\varepsilon(\tilde{\boldsymbol{u}}^h) : \boldsymbol{\sigma}(\varepsilon(\tilde{\boldsymbol{u}}^h), E^2, \nu^2) - \delta\varepsilon(\hat{\boldsymbol{u}}^h) : \boldsymbol{\sigma}(\varepsilon(\hat{\boldsymbol{u}}^h), E^1, \nu^1) \Big)\, \mathrm{d}\Omega$$

$$\delta U^I = -\int_{\Gamma^I} \Big(\delta\tilde{\boldsymbol{u}}^h - \delta\boldsymbol{u}^h \Big) \cdot \Big(\alpha^1 \boldsymbol{\sigma}(\varepsilon^h, E^1, \nu^1) + \alpha^2 \boldsymbol{\sigma}(\tilde{\varepsilon}^h, E^2, \nu^2) \Big) \cdot \boldsymbol{n}^1\, \mathrm{d}\Gamma \tag{4.23b}$$
$$- \int_{\Gamma^I} \Big(\alpha^1 \boldsymbol{\sigma}(\delta\varepsilon^h, E^1, \nu^1) + \alpha^2 \boldsymbol{\sigma}(\delta\tilde{\varepsilon}^h, E^2, \nu^2) \Big) \cdot \boldsymbol{n}^1 \cdot \Big(\tilde{\boldsymbol{u}}^h - \boldsymbol{u}^h \Big)\, \mathrm{d}\Gamma$$
$$+ \gamma \int_{\Gamma^I} \Big(\delta\tilde{\boldsymbol{u}}^h - \delta\boldsymbol{u}^h \Big) \cdot \Big(\tilde{\boldsymbol{u}}^h - \boldsymbol{u}^h \Big)\, \mathrm{d}\Gamma$$

$$\delta W^{ext} = \int_{\Omega} \delta\boldsymbol{u}^h \cdot \boldsymbol{b}^1\, \mathrm{d}\Omega + \int_{\Omega^2} \Big(\delta\tilde{\boldsymbol{u}}^h \cdot \boldsymbol{b}^2 - \delta\boldsymbol{u}^h \cdot \boldsymbol{b}^1 \Big)\, \mathrm{d}\Omega + \int_{\Gamma^h} \delta\boldsymbol{u}^h \cdot \boldsymbol{h}\, \mathrm{d}\Gamma \tag{4.23c}$$

$$\delta U^{EB} = -\int_{\Gamma^g} \delta\boldsymbol{\sigma}(\varepsilon(\boldsymbol{u}^h), E^1, \nu^1) \cdot \boldsymbol{n}^1 \cdot \boldsymbol{u}^h\, \mathrm{d}\Gamma - \int_{\Gamma^g} \delta\boldsymbol{u}^h \cdot \boldsymbol{\sigma}(\varepsilon(\boldsymbol{u}^h), E^1, \nu^1) \cdot \boldsymbol{n}^1\, \mathrm{d}\Gamma \tag{4.23d}$$
$$+ \beta \int_{\Gamma^g} \delta\boldsymbol{u}^h \cdot \boldsymbol{u}^h\, \mathrm{d}\Gamma + \int_{\Gamma^g} \delta\boldsymbol{\sigma}(\varepsilon(\boldsymbol{u}^h), E^1, \nu^1) \cdot \boldsymbol{n}^1 \cdot \boldsymbol{g}\, \mathrm{d}\Gamma - \beta \int_{\Gamma^g} \delta\boldsymbol{u}^h \cdot \boldsymbol{g}\, \mathrm{d}\Gamma$$

The equations above allow an arbitrary choice of approximations between Ω and Ω^2 with no restrictions on constructing the approximation functions along the interface. By introducing the approximations given by (4.15), (4.18), and (4.21) into (4.23a), the matrix form follows. The matrix form is cast in a block format where the diagonal stiffness matrices represent internal energy of the two bodies and the off-diagonal terms are associated with the weakly enforced

constraints responsible for displacement continuity.

$$\begin{bmatrix} \boldsymbol{K} & \boldsymbol{G} \\ \boldsymbol{G}^T & \tilde{\boldsymbol{K}} \end{bmatrix} \begin{Bmatrix} \boldsymbol{u} \\ \tilde{\boldsymbol{u}} \end{Bmatrix} = \begin{Bmatrix} \boldsymbol{f} \\ \tilde{\boldsymbol{f}} \end{Bmatrix} \tag{4.24}$$

where the stiffness terms are given as:

$$\boldsymbol{K}_{IJ} = \int_{\Omega} \boldsymbol{B}_I^T \boldsymbol{C}^1 \boldsymbol{B}_J \,\mathrm{d}\Omega - \int_{\Omega^2} \boldsymbol{B}_I^T \boldsymbol{C}^1 \boldsymbol{B}_J \,\mathrm{d}\Omega + \alpha^1 \int_{\Gamma^I} \boldsymbol{B}_I^T \boldsymbol{C}^1 \boldsymbol{\eta} \Psi_J \,\mathrm{d}\Gamma \tag{4.25a}$$

$$+\alpha^1 \int_{\Gamma^I} \Psi_I \boldsymbol{\eta}^T \boldsymbol{C}^1 \boldsymbol{B}_J \,\mathrm{d}\Gamma + \gamma \boldsymbol{I} \int_{\Gamma^I} \Psi_I \Psi_J \,\mathrm{d}\Gamma + \boldsymbol{K}_{IJ}^{EB}$$

$$\boldsymbol{K}_{IJ}^{EB} = -\int_{\Gamma^g} \boldsymbol{B}_I^T \boldsymbol{C}^1 \boldsymbol{\eta} \Psi_J \,\mathrm{d}\Gamma - \int_{\Gamma^g} \Psi_I \boldsymbol{\eta}^T \boldsymbol{C}^1 \boldsymbol{B}_J \,\mathrm{d}\Gamma + \beta \boldsymbol{I} \int_{\Gamma^g} \Psi_I \Psi_J \,\mathrm{d}\Gamma \tag{4.25b}$$

$$\boldsymbol{G}_{IJ} = -\alpha^1 \int_{\Gamma^I} \boldsymbol{B}_I^T \boldsymbol{C}^1 \boldsymbol{\eta} \tilde{\Psi}_J \,\mathrm{d}\Gamma + \alpha^2 \int_{\Gamma^I} \Psi_I \boldsymbol{\eta}^T \boldsymbol{C}^2 \tilde{\boldsymbol{B}}_J \,\mathrm{d}\Gamma - \gamma \boldsymbol{I} \int_{\Gamma^I} \Psi_I \tilde{\Psi}_J \,\mathrm{d}\Gamma \tag{4.25c}$$

$$\tilde{\boldsymbol{K}}_{IJ} = \int_{\Omega^2} \tilde{\boldsymbol{B}}_I^T \boldsymbol{C}^2 \tilde{\boldsymbol{B}}_J \,\mathrm{d}\Omega - \alpha^2 \int_{\Gamma^I} \tilde{\boldsymbol{B}}_I^T \boldsymbol{C}^2 \boldsymbol{\eta} \tilde{\Psi}_J \,\mathrm{d}\Gamma \tag{4.25d}$$

$$-\alpha^2 \int_{\Gamma^I} \tilde{\Psi}_I \boldsymbol{\eta}^T \boldsymbol{C}^2 \tilde{\boldsymbol{B}}_J \,\mathrm{d}\Gamma + \gamma \boldsymbol{I} \int_{\Gamma^I} \tilde{\Psi}_I \tilde{\Psi}_J \,\mathrm{d}\Gamma$$

and the forcing terms are given as:

$$\boldsymbol{f}_I = \int_{\Omega} \Psi_I \boldsymbol{b}^1 \,\mathrm{d}\Omega - \int_{\Omega^2} \Psi_I \boldsymbol{b}^1 \,\mathrm{d}\Omega + \int_{\Gamma^h} \Psi_I \boldsymbol{h} \,\mathrm{d}\Gamma + \boldsymbol{f}_I^{EB} \tag{4.26a}$$

$$\boldsymbol{f}_I^{EB} = \int_{\Gamma^g} \boldsymbol{B}_I^T \boldsymbol{C}^1 \boldsymbol{\eta} \boldsymbol{g} \,\mathrm{d}\Gamma - \beta \int_{\Gamma^g} \Psi_I \boldsymbol{g} \,\mathrm{d}\Gamma \tag{4.26b}$$

$$\tilde{\boldsymbol{f}}_I = \int_{\Omega^2} \tilde{\Psi}_I \boldsymbol{b}^2 \,\mathrm{d}\Omega \tag{4.26c}$$

Here the elastic modulii tensors are given by $\boldsymbol{C}^1 \equiv \boldsymbol{C}(E^1, \nu^1)$ and $\boldsymbol{C}^2 \equiv \boldsymbol{C}(E^2, \nu^2)$. The gradient

matrix $\boldsymbol{B}_I$ and normal matrix $\boldsymbol{\eta}$ are defined as

$$\boldsymbol{B}_I^T = \begin{bmatrix} \Psi_{I,1} & 0 & 0 & \Psi_{I,2} & \Psi_{I,3} & 0 \\ 0 & \Psi_{I,2} & 0 & \Psi_{I,1} & 0 & \Psi_{I,3} \\ 0 & 0 & \Psi_{I,3} & 0 & \Psi_{I,1} & \Psi_{I,2} \end{bmatrix} \tag{4.27a}$$

$$\tilde{\boldsymbol{B}}_I^T = \begin{bmatrix} \tilde{\Psi}_{I,1} & 0 & 0 & \tilde{\Psi}_{I,2} & \tilde{\Psi}_{I,3} & 0 \\ 0 & \tilde{\Psi}_{I,2} & 0 & \tilde{\Psi}_{I,1} & 0 & \tilde{\Psi}_{I,3} \\ 0 & 0 & \tilde{\Psi}_{I,3} & 0 & \tilde{\Psi}_{I,1} & \tilde{\Psi}_{I,2} \end{bmatrix} \tag{4.27b}$$

$$\boldsymbol{\eta}^T = \begin{bmatrix} n_1 & 0 & 0 & n_2 & n_3 & 0 \\ 0 & n_2 & 0 & n_1 & 0 & n_3 \\ 0 & 0 & n_3 & 0 & n_1 & n_2 \end{bmatrix} \tag{4.27c}$$

Remark 1: In the implementation of the method above, one must define two sets of shape functions corresponding to the background and foreground. Further, the integration of the various terms may involve shape functions from both sets when integrating over the interface. A pseudo-code for the immersed RKPM method is given in Appendix A.

Remark 2: During output, the displacements in each sub-domain $\overline{\Omega}^i$ are obtained using the corresponding approximation functions in each sub-domain:

$$\boldsymbol{u}^h(\boldsymbol{x}) = \begin{cases} \sum_{I \in S} \Psi_I(\boldsymbol{x}) \boldsymbol{u}_I & \boldsymbol{x} \in \Omega^1 \\ \sum_{I \in \tilde{S}} \tilde{\Psi}_I(\boldsymbol{x}) \tilde{\boldsymbol{u}}_I & \boldsymbol{x} \in \Omega^2 \end{cases} \tag{4.28}$$

Similar evaluations for the strain and stress fields are also employed.

Remark 3: The stiffness matrix $\boldsymbol{K}$ may further be subdivided into two regions. Considering the original sub-domain $\overline{\Omega}^1$, point sets $S_A = \{I \,|\, \text{supp}(\Psi_I) \cap \overline{\Omega}^1 \neq \emptyset\}$ and $S_B = S \setminus S_A$ are defined. The first set S_A includes nodal points which may reside in $\overline{\Omega}^2$ but has kernel value in the original sub-domain $\overline{\Omega}^1$. In contrast, the second set S_B corresponds to nodal points strictly inside

of $\overline{\Omega}^2$ which do not have kernel value in $\overline{\Omega}^1$. The system of equations can be written as

$$\begin{bmatrix} \boldsymbol{K}_{AA} & \boldsymbol{K}_{AB} & \boldsymbol{G} \\ \boldsymbol{K}_{BA} & \boldsymbol{K}_{BB} & \mathbf{0} \\ \boldsymbol{G}^T & \mathbf{0} & \tilde{\boldsymbol{K}} \end{bmatrix} \begin{bmatrix} \boldsymbol{u}_A \\ \boldsymbol{u}_B \\ \tilde{\boldsymbol{u}} \end{bmatrix} = \begin{bmatrix} \boldsymbol{f}_A \\ \boldsymbol{f}_B \\ \tilde{\boldsymbol{f}} \end{bmatrix} \tag{4.29}$$

Under sufficient integration, the terms $\boldsymbol{K}_{AB}$, $\boldsymbol{K}_{BA}$, and $\boldsymbol{K}_{BB}$ are nearly zero due to the second term in (4.25a). This is problematic for iterative matrix solvers. In this case, the background node set may be modified such that $S \leftarrow S \setminus S_B$ to completely remove these nodes from the analysis. This has the additional advantage of reducing the total number of equations to solve since the fictitious degrees of freedom are removed. Alternatively, the rows and columns corresponding to S_B may be condensed out of the matrix entirely by replacing those degrees of freedom with identity to remove any ill-conditioning problems. The topic of integration is discussed in more detail in the next chapter.

Acknowledgements

This chapter is currently being prepared for submission for publication of the material. F. Beckwith, J.S. Chen, and H. Wei, “An Immersed Reproducing Kernel Particle Method for Modeling Inhomogeneous Media.” The dissertation author was the primary investigator of this material.

Chapter 5

Domain integration of the immersed RKPM method

In order to solve a given problem using the immersed RKPM method, numerical integration rules for use with the equations given in Chapter 4 must first be defined. Unlike FEM, the integration rules for meshfree methods is not a straightforward task. Gauss quadrature fails to give exact integration for the rational RK shape functions with supports that do not match with the integration cells. Further, Dolbow and Belytschko [26] and Chen et al. [20, 13, 12] showed that significant error results when the quadrature cells are not aligned with the kernel support of the shape functions. For these reasons, domain integration for meshfree methods must be carefully formulated. This chapter discusses the integration details for the immersed RKPM method.

Domain integration of the bulk terms in the immersed method is carried out in three main steps: a total domain integral over $\overline{\Omega}$ of the background matrix; a domain integral over $\overline{\Omega}^2$ of the inclusion; and a domain integral over the fictitious domain coinciding with $\overline{\Omega}^2$ to subtract the fictitious energy introduced previously. A similar series of integrals is also carried out to compute the external work due to body forces and tractions on the natural boundary. Accordingly, two sets of integration cells are defined for the immersed RKPM method. Let

the set of points $\{\boldsymbol{\xi}_L\}_{L=1}^{N_{int}}$ define the integration points of the background with corresponding integration weights $\{w_L\}_{L=1}^{N_{int}}$. Similarly, the set of points $\{\tilde{\boldsymbol{\xi}}_L\}_{L=1}^{\tilde{N}_{int}}$ defines the integration points of the foreground with corresponding integration weights $\{\tilde{w}_L\}_{L=1}^{\tilde{N}_{int}}$. A set of integration points is also defined to numerically integrate the fictitious domain terms, which is discussed later. The integration domain for the background matrix taken over $\overline{\Omega}$ is illustrated by Figure 5.1a whereas the integration domain for the inclusion domain taken over $\overline{\Omega}^2$ is shown in Figure 5.1b. Although shown separately, the integration domains overlap in general and are not required to conform to each other.

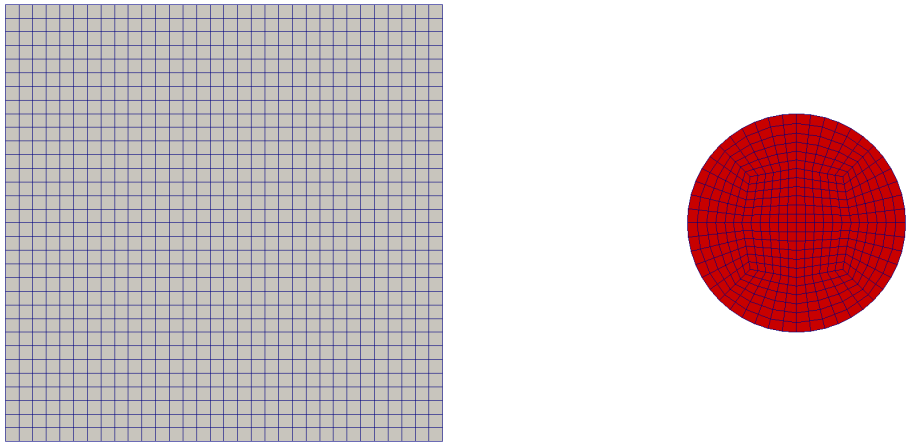

(a) (b)

Figure 5.1: Integration domains for immersed RKPM. (a) Background integration mesh over $\overline{\Omega}$; (b) Foreground integration mesh over $\overline{\Omega}^2$

After the internal energy and external work from the bulk contributions of the background, foreground, and fictitious domains are calculated, they are coupled together using Nitsche's method at the material interface. Let $\{\boldsymbol{\xi}_L^I\}_{L=1}^{N_{int}^I}$ define the integration points of on the interface Γ^I with corresponding integration weights $\{w_L^I\}_{L=1}^{N_{int}^I}$. This set of integration points is responsible for enforcing the interface conditions given in (4.25a). In a similar manner, integration points are

generated for the essential boundary terms over Γ^g.

The remainder of this chapter discusses techniques for generating these integration points for the immersed RKPM method. Many integration methods exists for RKPM, including background Gauss integration, stabilized conforming nodal integration (SCNI) [20], modified stabilized conforming nodal integration [14, 73], variationally consistent integration [13], and naturally stabilized nodal integration (NSNI) [43]. The reader is referred to [12] for more details. This dissertation focuses on Gauss integration using background quadrature cells and the modified stabilized nodal integration method.

5.1 Gauss Integration with Background Quadrature Cells

One option for quadrature is simply to use Gauss integration (GI) over each integration cell. This method involves populating the domain with a set of uniform cells over which integration points are generated. Alternatively, integration points may be generated for non-uniform background cells which conform to the computational domain of the problem. An example of GI is depicted in Figure 5.2.

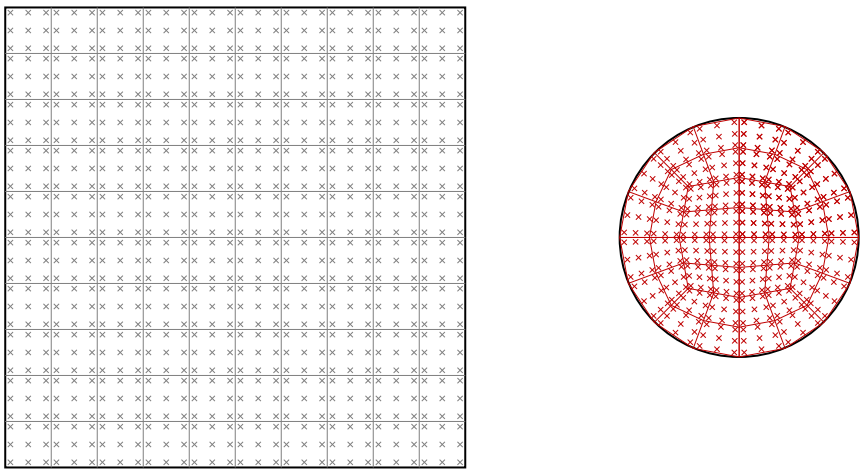

(a) (b)

Figure 5.2: Integration domains for immersed RKPM using GI. (a) Background quadrature points; (b) Foreground quadrature points

It remains to be stated how the internal energy of the fictitious domain is integrated. One option is to use the same quadrature rule as that is used from the foreground integration. This is the simplest approach, but introduces integration error when integrating the internal energy of the fictitious domain with non-conformity between the background and fictitious integration domains. This leads to nearly zero stiffness coefficients in the matrix $\boldsymbol{K}$ for nodes spanned by the fictitious domain and introduces spurious oscillations as a result. A second option is to copy a subset of the background integration points, i.e. $\{\hat{\boldsymbol{\xi}}_L\} = \{\boldsymbol{\xi}_L \mid \boldsymbol{\xi}_L \in \overline{\Omega}^2\}$ for the fictitious domain integral. This alternative approach is illustrated in Figure 5.3. Using this scheme, the integration cells for the background and fictitious domains match, and the stiffness coefficients associated with the fictitious nodes become zero and can be condensed out of the stiffness matrix. However, some error is introduced because the domain described by the integration points $\{\hat{\boldsymbol{\xi}}_L\}$ does not conform with the true geometry of the fictitious domain, which is that of the inclusion itself.

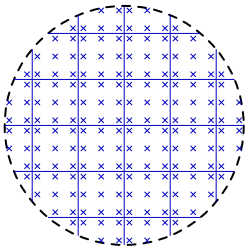

Figure 5.3: Alternative integration points for fictitious domain

Although straightforward to implement, Gauss integration is not variationally consistent with the Galerkin method and only converges optimally when a large number of integration points is used in each integration cell, which is computationally expensive. This was demonstrated in Chen et al. [20], where additional integration constraints were identified to achieve linear exactness in the meshfree Galerkin approximation. For approximations with first order completeness, the

integration constraint on the numerical quadrature of a 2nd-order PDE is

$$\hat{\int}_{\Omega} \nabla \Psi_I \, \mathrm{d}\Omega = \hat{\int}_{\Gamma} \Psi_I \boldsymbol{n} \, \mathrm{d}\Gamma \tag{5.1}$$

where a superposed '^' denotes numerical integration. (5.1) is the numerical quadrature version of the divergence theorem [20]. There it was found that Gauss integration does not satisfy the integration constraint if the shape function supports and the integration cells do not conform with each other, and consequently optimal convergence is lost in the numerical solution.

5.2 Modified Stabilized Conforming Nodal Integration

To satisfy the integration constraint for an arbitrary RK discretization, stabilized conforming nodal integration (SCNI) was proposed in [20] where the gradients of the displacement approximation are computed as follows.

$$\overline{\nabla} \otimes \boldsymbol{u}^h(\boldsymbol{x}_L) = \frac{1}{V_L} \hat{\int}_{\Omega_L} \nabla \otimes \boldsymbol{u}^h \, \mathrm{d}\Omega = \frac{1}{V_L} \hat{\int}_{\Gamma_L} \boldsymbol{u}^h \otimes \boldsymbol{n} \, \mathrm{d}\Gamma = \sum_{I \in S} \overline{\nabla} \Psi_I(\boldsymbol{x}_L) \boldsymbol{u}_I \tag{5.2a}$$

$$\overline{\boldsymbol{\varepsilon}}(\boldsymbol{u}^h) = \frac{1}{2} \left(\overline{\nabla} \otimes \boldsymbol{u}^h + \boldsymbol{u}^h \otimes \overline{\nabla} \right) \tag{5.2b}$$

where $V_L = \int_{\Omega_L} \mathrm{d}\Omega$ is the volume of the nodal representative domain Ω_L, and Γ_L is its boundary. Introducing (3.34) gives

$$\overline{\nabla} \Psi_I(\boldsymbol{x}_L) = \frac{1}{V_L} \hat{\int}_{\Gamma_L} \Psi_I(\boldsymbol{x}) \boldsymbol{n}(\boldsymbol{x}) \, \mathrm{d}\Gamma \tag{5.3}$$

To compute the above boundary integral, a simple trapezoidal rule over the surface of the nodal representative domain may be used. Combining the above result with nodal integration satisfies the integration constraint in (5.1) if the set of nodal representative domains $\{\Omega_L\}_{L=1}^{N_{int}}$ are conforming, such as the Voronoi diagram as shown in Figure 5.4a. Employing the above and redefining the set of integration points and their weights as nodal points $\{\boldsymbol{x}_L\}_{L \in S}$ and nodal volumes $\{V_L\}_{L \in S}$, the

discrete domain integral is expressed as

$$\int_{\hat{\Omega}} \delta\boldsymbol{\varepsilon}^h : \boldsymbol{C}^1 : \boldsymbol{\varepsilon}^h \, \mathrm{d}\Omega = \sum_{L \in S} \overline{\boldsymbol{\varepsilon}}(\delta \boldsymbol{u}^h) : \boldsymbol{C}^1 : \overline{\boldsymbol{\varepsilon}}(\boldsymbol{u}^h) V_L \tag{5.4}$$

Similarly, the set of integration points over the foreground is redefined to be $\{\tilde{\boldsymbol{x}}_L\}_{L \in \tilde{S}}$ with associated weights $\{\tilde{V}_L\}_{L \in \tilde{S}}$. Similar treatment on the gradient of shape functions may be generated for the foreground approximation as follows.

$$\overline{\nabla} \tilde{\Psi}_I(\boldsymbol{x}_L) = \frac{1}{V_L} \int_{\hat{\Gamma}_L} \tilde{\Psi}_I(\boldsymbol{x}) \boldsymbol{n}(\boldsymbol{x}) \, \mathrm{d}\Gamma \tag{5.5}$$

The corresponding discrete domain integral for the foreground inclusion is given as

$$\int_{\hat{\Omega}^2} \delta\tilde{\boldsymbol{\varepsilon}}^h : \boldsymbol{C}^2 : \tilde{\boldsymbol{\varepsilon}}^h \, \mathrm{d}\Omega = \sum_{L \in \tilde{S}} \overline{\boldsymbol{\varepsilon}}(\delta \tilde{\boldsymbol{u}}^h) : \boldsymbol{C}^2 : \overline{\boldsymbol{\varepsilon}}(\tilde{\boldsymbol{u}}^h) V_L \tag{5.6}$$

In [14], it is reported that although SCNI is variationally consistent, it still possesses spurious low-energy modes. To suppress these unphysical modes and to assume coercivity, a modified SCNI procedure, or M-SCNI [14, 73], was proposed with the following form

$$\begin{aligned} \int_{\hat{\Omega}} \delta\boldsymbol{\varepsilon}^h : \boldsymbol{C} : \boldsymbol{\varepsilon}^h \, \mathrm{d}\Omega = \sum_{L=1}^{NP} \Bigg\{ & \underbrace{\overline{\boldsymbol{\varepsilon}}(\delta \boldsymbol{u}^h) : \boldsymbol{C} : \overline{\boldsymbol{\varepsilon}}^h(\boldsymbol{u}^h)}_{\text{SCNI}} + \\ & + \underbrace{\sum_{K \in S_L} \left[c_L^K \left(\boldsymbol{\varepsilon}(\delta \boldsymbol{u}^h) - \overline{\boldsymbol{\varepsilon}}(\delta \boldsymbol{u}^h) \right) : \boldsymbol{C} : \left(\boldsymbol{\varepsilon}(\boldsymbol{u}^h) - \overline{\boldsymbol{\varepsilon}}(\boldsymbol{u}^h) \right) \right]}_{\text{Additional stabilization}} \Bigg\} V_L \end{aligned} \tag{5.7}$$

where c_L^K is a stabilization coefficient ranging between 0 and 1 and S_L is a set of sub-cells which decompose the SCNI nodal representative domain as shown in Figure 5.4b. In 5.7 above, $\boldsymbol{\varepsilon}(\boldsymbol{u}^h)$ is evaluated at the centroid of each sub-cell.

Using M-SCNI, a set of nodal representative domains may be generated using a Voronoi diagram. An example of such an integration scheme is given in Figure 5.5. Since each node

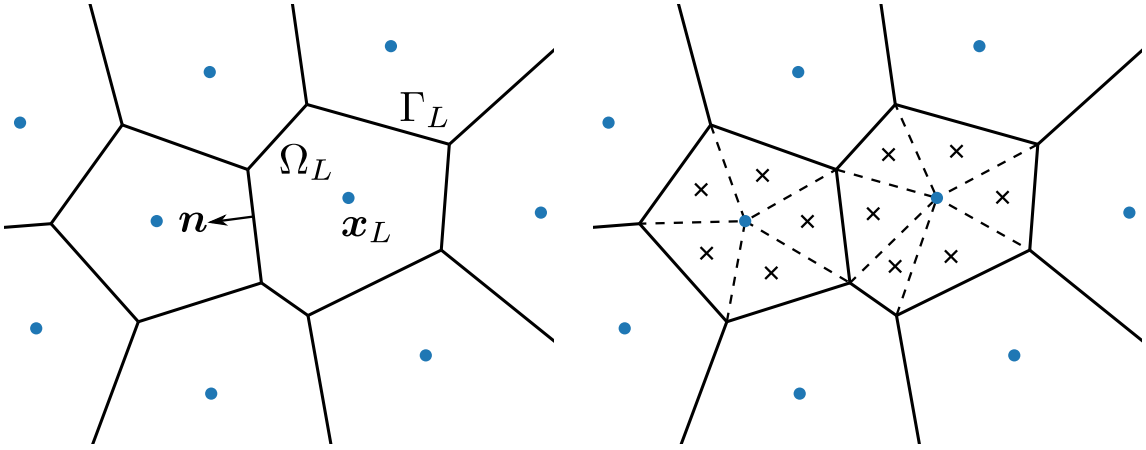

Figure 5.4: Integration cells for SCNI and M-SCNI. (a) SCNI cells at nodal integration point $\mathbf{x}_L$; (b) M-SCNI sub-cells associated with the nodal integration point $\mathbf{x}_L$. Each "x" indicates the centroid of sub-cell $\mathbf{x}_K$.

in the figure is effectively an integration point with an associated nodal volume, this method is much cheaper in comparison to GI depicted earlier in Figure 5.2, which clearly has many more evaluation points. The nodes and their volumes define the new integration sets $\{\mathbf{x}_L\}_{L=1}^{NP}$ and $\{\tilde{\mathbf{x}}_L\}_{L=1}^{\tilde{N}P}$. For integrating the interface conditions on Γ^I, the surface points of the foreground nodal representative domains which lie on the interface used in the calculation of the smoothed shape functions in (5.3) are reused for surface integration.

As for the strategies for generating integration points for the fictitious domains, one may choose to copy specific points from the set of background nodal representative domains or from the foreground nodal representative domains. Similar to GI described earlier, the first option is to define a set of integration points $\{\hat{\mathbf{x}}_L\}_{L=1}^{\hat{N}_{int}} = \{\tilde{\mathbf{x}}_L\}_{L=1}^{\tilde{N}_{int}}$. Alternatively, the fictitious integration points may be chosen as a subset of the background integration points, i.e. $\{\hat{\mathbf{x}}_L\} = \{\mathbf{x}_L \mid \mathbf{x}_L \in \overline{\Omega}^2\}$. The first option integrates the true geometry of the fictitious domain more accurately but leads to nearly zero stiffness terms which must be dealt with in the system of equations. The second option approximates the geometry of the fictitious domain but consistently integrates the internal energy of the background and fictitious terms.

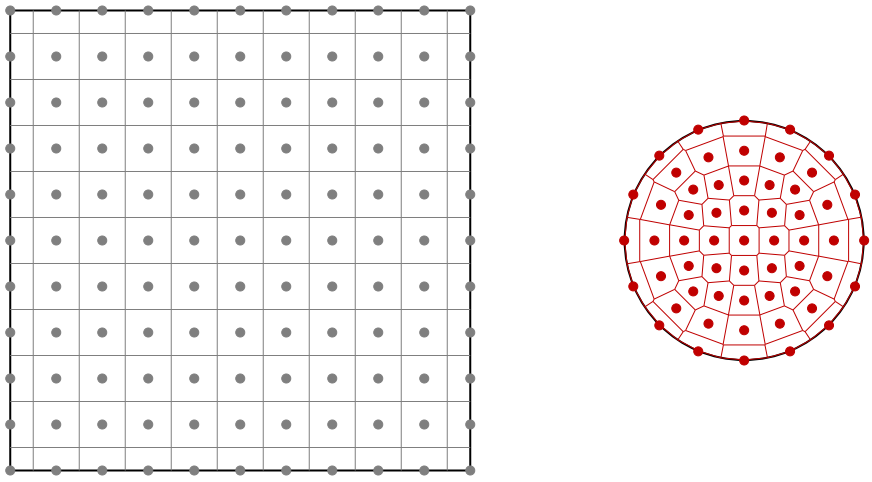

(a) (b)

Figure 5.5: Integration domains for immersed RKPM using M-SCNI, where each circle represents a node surrounded by its representative nodal domain. (a) Background nodal representative domains; (b) Foreground nodal representative domains

A third option is to take a subset of the background integration cells but this time cutting the cells which are intersected by the material interface. If the true geometry of the inclusion is curvilinear, the cut is approximated by identifying the intersection points with the cell to be cut and then cutting them with a plane section. The set of integration points for the fictitious domain is identical to the second option proposed above, but now conforms much more closely to the inclusion geometry due to the cut cells. An example of such a cut cell is shown in Figure 5.6. While presented for M-SCNI, cutting the integration cells is a valid technique for GI as well, but requires more complicated rules for populating each cell with Gauss points afterwards.

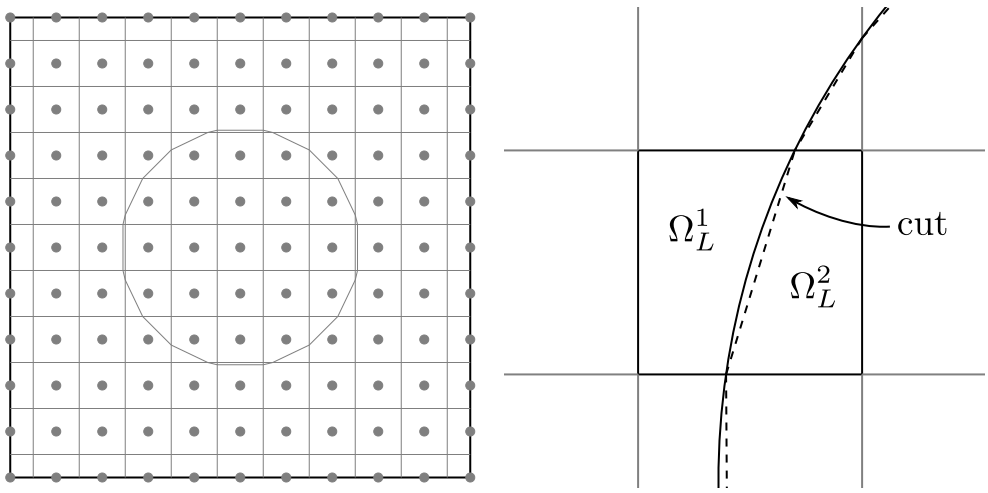

Figure 5.6: Cutting technique near material interface. (a) Background integration mesh over $\overline{\Omega}$ with cut cells; (b) Close-up view of cut cells. Ω_L^1 is the cut portion belonging to the background and Ω_L^2 is the cut belonging to the foreground.

5.3 Eshelby Analogy for the Multi-Material Problem

The integration constraints above are established for a homogeneous body with a single medium. The question remains whether this same integration constraint is valid for the immersed RKPM framework. To answer this question, the problem is posed as a series of heuristic steps where each has an accompanying state of stress and strain, similar to Eshelby's pioneering work on solving the inclusion problem [30]. The final solution is then a superposition of all the steps involved.

We first assume a homogeneous body without an inclusion subject to some far-field strain, denoted as ε^∞. The stress and strain in the matrix and inclusion sub-domains for this body are given as

$$\varepsilon^{m1} = \varepsilon^{I1} = \varepsilon^\infty \quad \boldsymbol{\sigma}^{m1} = \boldsymbol{\sigma}^{I1} = \boldsymbol{C}^1 : \varepsilon^\infty \tag{5.8}$$

At this stage, an inclusion with modified properties $\boldsymbol{C}^* = \boldsymbol{C}^2 - \boldsymbol{C}^1$ is to be inserted into the homogeneous medium. However, to do so it needs to be brought to the same state of deformation

as the outer medium. A traction $\boldsymbol{t} = \boldsymbol{C}^* : \varepsilon^\infty \cdot \boldsymbol{n}^2$ is applied to the inclusion's boundary Γ^I for it to assume the correct shape. The strain and stress at the end of the second step are

$$\varepsilon^{m2} = \varepsilon^\infty \quad \boldsymbol{\sigma}^{m2} = \boldsymbol{C}^1 : \varepsilon^\infty \tag{5.9a}$$

$$\varepsilon^{I2} = \varepsilon^\infty \quad \boldsymbol{\sigma}^{I2} = \boldsymbol{C}^1 : \varepsilon^\infty + \boldsymbol{C}^* : \varepsilon^\infty = \boldsymbol{C}^2 : \varepsilon^\infty \tag{5.9b}$$

The inclusion now has the correct shape and can be inserted at the location of the deformed inclusion of the outer medium and the bodies are "fused" together. However, an embedded layer of traction has been introduced to do so. This traction is removed by applying an equal and opposite traction $-\boldsymbol{t}^*$ to the interface Γ^I to negate the effect of the previous traction. Because the bodies are now effectively welded together at this point, this creates a constrained response ε^c in both the medium and the inclusion. Note, this strain field is necessarily discontinuous across the interface due to the difference in materials but the resultant stress and displacement field are continuous.

$$\varepsilon^{m3} = \varepsilon^c \quad \boldsymbol{\sigma}^{m3} = \boldsymbol{C}^1 : \varepsilon^c \tag{5.10a}$$

$$\varepsilon^{I3} = \varepsilon^c \quad \boldsymbol{\sigma}^{I3} = \boldsymbol{C}^2 : \varepsilon^c \tag{5.10b}$$

From the principle of superposition, the total response is the sum of all the individual responses from independent loadings.

$$\varepsilon^m = \varepsilon^\infty + \varepsilon^c \quad \boldsymbol{\sigma}^m = \boldsymbol{C}^1 : (\varepsilon^\infty + \varepsilon^c) \tag{5.11a}$$

$$\varepsilon^I = \varepsilon^\infty + \varepsilon^c \quad \boldsymbol{\sigma}^I = \boldsymbol{C}^2 : (\varepsilon^\infty + \varepsilon^c) \tag{5.11b}$$

In the above analysis, the far-field strain ε^∞ can be taken as polynomial of degree n under consideration, and the kinematics and kinetics of steps 1 and 2 are trivial. The third step involves the constrained field ε^c which depends on the geometry and the material properties in

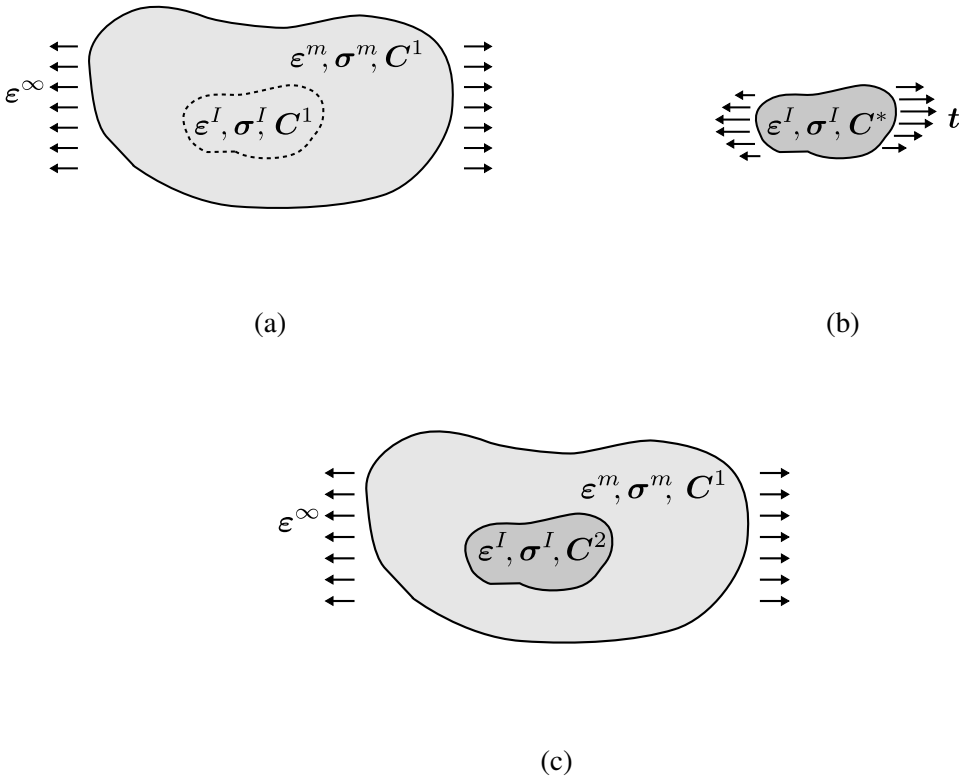

Figure 5.7: Superposition analogy of an inclusion. (a) shows the homogeneous body under far-field ε^∞; (b) is the inclusion deformed according to ε^∞; and (c) is the insertion and removal of traction $\boldsymbol{t}$

the inclusion and the matrix, and in general is non-smooth. For the development of integration constraints for the immersed formulation, Galerkin exactness of the boundary value problems is enforced in the first two steps of the above process, and the third step accounts for the higher order effects. As such, both the deformation in the matrix and the inclusion are polynomial, where the field in the background is given by $\boldsymbol{u}^n = \sum_{|\alpha|\leq n} \boldsymbol{c}_\alpha \boldsymbol{x}^\alpha$ and the field in the foreground is given by $\tilde{\boldsymbol{u}}^n = \sum_{|\alpha|\leq n} \tilde{\boldsymbol{c}}_\alpha \boldsymbol{x}^\alpha$. Under this assumption, the following three integration constraints

are determined following the variationally consistency procedure similar to that in [13].

$$\hat{\int}_{\Omega} \nabla \Psi_I \cdot \boldsymbol{\sigma}^{\alpha} \, \mathrm{d}\Omega = -\hat{\int}_{\Omega} \Psi_I \nabla \cdot \boldsymbol{\sigma}^{\alpha} \, \mathrm{d}\Omega + \hat{\int}_{\Gamma} \Psi_I \boldsymbol{\sigma}^{\alpha} \cdot \boldsymbol{n} \, \mathrm{d}\Gamma \tag{5.12a}$$

$$\hat{\int}_{\Omega^2} \nabla \tilde{\Psi}_I \cdot \tilde{\boldsymbol{\sigma}}^{\alpha} \, \mathrm{d}\Omega = -\hat{\int}_{\Omega^2} \tilde{\Psi}_I \nabla \cdot \tilde{\boldsymbol{\sigma}}^{\alpha} \, \mathrm{d}\Omega + \hat{\int}_{\Gamma^I} \tilde{\Psi}_I \tilde{\boldsymbol{\sigma}}^{\alpha} \cdot \boldsymbol{n} \, \mathrm{d}\Gamma \tag{5.12b}$$

$$-\hat{\int}_{\Omega^2} \nabla \Psi_I \cdot \boldsymbol{\sigma}^{\alpha} \, \mathrm{d}\Omega = \hat{\int}_{\Omega^2} \Psi_I \nabla \cdot \boldsymbol{\sigma}^{\alpha} \, \mathrm{d}\Omega - \hat{\int}_{\Gamma^I} \Psi_I \boldsymbol{\sigma}^{\alpha} \cdot \boldsymbol{n} \, \mathrm{d}\Gamma \tag{5.12c}$$

(5.12a) is the integration constraint for the background over the total domain, (5.12b) is the integration constraint for the inclusion, and (5.12c) is the integration constrain for the fictitious domain introduced in the immersed framework. Under constant stress and strain for the first order Galerkin exactness, the integration constraints become

$$\hat{\int}_{\Omega} \nabla \Psi_I \, \mathrm{d}\Omega = \hat{\int}_{\Gamma} \Psi_I \boldsymbol{n} \, \mathrm{d}\Gamma \tag{5.13a}$$

$$\hat{\int}_{\Omega^2} \nabla \tilde{\Psi}_I \, \mathrm{d}\Omega = \hat{\int}_{\Gamma^I} \tilde{\Psi}_I \boldsymbol{n} \, \mathrm{d}\Gamma \tag{5.13b}$$

$$-\hat{\int}_{\Omega^2} \nabla \Psi_I \, \mathrm{d}\Omega = -\hat{\int}_{\Gamma^I} \Psi_I \boldsymbol{n} \, \mathrm{d}\Gamma \tag{5.13c}$$

The SCNI formulation given in (5.3)-(5.6) is introduced in (5.1) based on the integration constraints in (5.12) for each of the total, inclusion, and fictitious domain integrals.

Acknowledgements

This chapter is currently being prepared for submission for publication of the material. F. Beckwith, J.S. Chen, and H. Wei, “An Immersed Reproducing Kernel Particle Method for Modeling Inhomogeneous Media.” The dissertation author was the primary investigator of this material.

Chapter 6

Verification of Immerse RKPM for Linear Analysis of Heterogeneous Materials

The immersed RKPM method is demonstrated in the examples that follow. In all of the examples, the RK approximation is constructed using linear basis with cubic B-spline kernels unless otherwise noted. The numerical results are obtained using 5-point Gauss quadrature as well as M-SCNI. A one-sided flux with $\alpha^1 = 1$ and $\alpha^2 = 0$ is considered and a stabilization parameter of $\gamma = 2.0E_1/h$ is taken.

6.1 Composite Rod

A composite rod in one dimension with different material constants E_1 and E_2 is fixed on the left side and subjected to a prescribed displacement g on the right side, as depicted in

Figure 6.1. The exact solution for the field with no body force is given by

$$u(x) = \begin{cases} \frac{E_2 g}{A} x & x \in [0, x_1] \\ \frac{(E_2 - E_1) x_1 g}{A} + \frac{E_1 g}{A} x & x \in [x_1, x_2] \\ \frac{(E_2 - E_1)(x_1 - x_2) g}{A} + \frac{E_2 g}{A} x & x \in [x_2, L] \end{cases} \tag{6.1a}$$

$$A = E_2 (L - x_2 + x_1) + E_1 (x_2 - x_1) \tag{6.1b}$$

where x_1 and x_2 mark the beginning and end of the inclusion and L is the length of the rod. For this example, $L = 10.0$ with $x_1 = 3.75$ and $x_2 = 6.25$. Material constants of $E_1 = 2.0 \times 10^9$ and $E_2 = 2.0 \times 10^{11}$ are selected with a prescribed displacement $g = 1.0$.

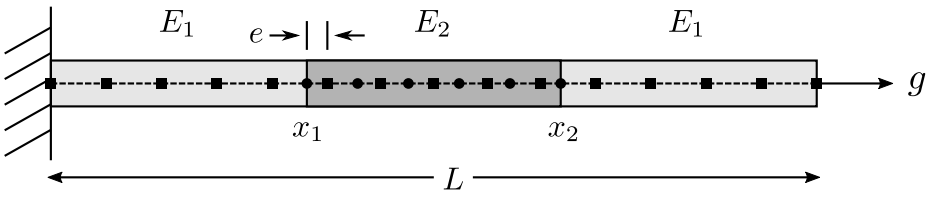

Figure 6.1: Bi-material rod with a prescribed displacement. Solid squares denote discretization points of the background and circles denote discretization points of the foreground.

The problem is modeled using the immersed RKPM method with linear basis and a normalized support $a = 2.0h$. Following the analysis given in [3], Nitsche's parameters $\gamma = 2E_1/h$ and $\beta = E_1/h$ are selected to enforce displacement continuity across the material interface and the essential boundary conditions, respectively. The model is discretized with 21 equally spaced points in the foreground corresponding to a nodal spacing of $h = 0.083$. To test the effect of discretization mismatch between the background and foreground, the background was discretized from 121 to 125 equally spaced points. At 121 background points, the background and foreground discretizations coincide. We define the mismatch, e, as the distance from the boundary of the

inclusion to the nearest node in the background points as shown in Figure 6.1. For this example, the values of e are selected as $e/h = 0.0, 0.25$, and 0.5. To achieve these values, the number of discretized points in the background are 121, 123, and 125 nodes, respectively.

The immersed RKPM formulation is first tested with 5-point Gauss quadrature, and the results of the displacement and strain fields are given in Figures 6.2, 6.3a, and 6.3b, respectively. The displacement solution is shown to agree with the analytical solution very well regardless of how well the discretizations are aligned. The error that can be seen is attributed to the approximate integration. When a misalignment e is present, the integration domains of the foreground and background do not coincide and leads to some error in the strain in the background field in the order of 10^{-3}. However, the foreground strain is seen to match very well with the analytical solution.

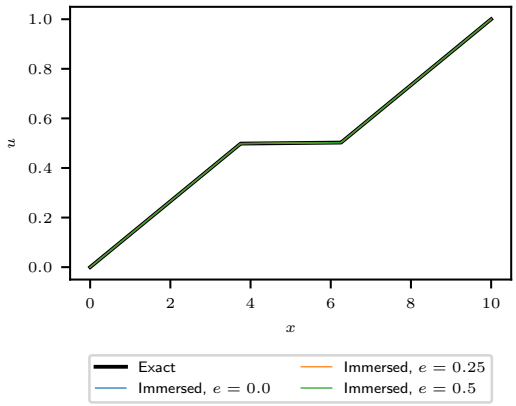

Figure 6.2: Displacement field of the composite rod, $a = 2.0h$

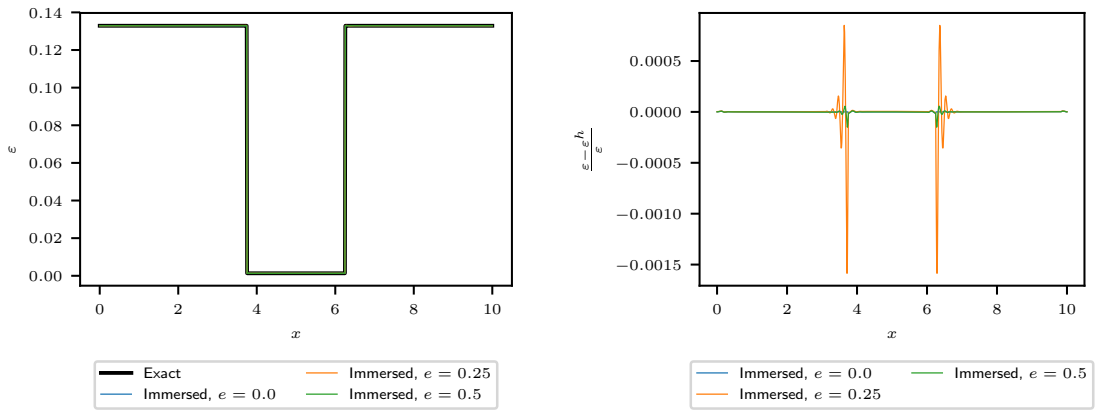

(a) (b)

Figure 6.3: Strain fields of the composite rod, $a = 2.0h$. (a) is the strain field and (b) is the normalized strain error.

For comparison, the 1D problem was modeled using body-unfitted FEM following the immersed procedure described in Section 4.3.1 but with an FEM approximation instead of an RK approximation. Linear, 2-node elements were utilized with the same discretization as the immersed RKPM setup. The results of the normalized strain error are given in Figure 6.4. Here, the error is seen to be much larger near the interface than the previous results given by the immersed RKPM approach in Figure 6.3.

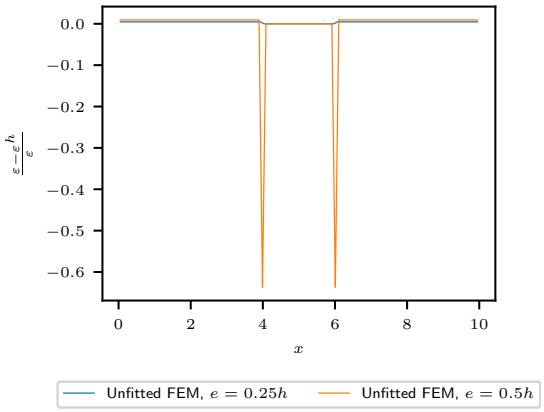

Figure 6.4: Normalized strain error with body-unfitted FEM

The next study investigates the impact of integration methods and integration accuracy in the immersed approach. In Figure 6.5, the number of Gauss quadrature points in each background cell varies from 1 to 4 point quadrature. When only a single integration point is used, significant error in the strain field is observed, shown in Figure 6.5a. The error in the strain reduces substantially as the order of integration increases. In this case, 5-point quadrature is sufficient for integration and higher order quadrature does not substantially improve the solution.

In addition to using GI above, M-SCNI is investigated with immersed RKPM, shown in Figure 6.6. M-SCNI gives exact answers near round-off error when there is no mismatch (i.e. $e = 0.0h$) with the largest normalized error of 3.1×10^{-12} in the strain field. By comparison, the maximum normalized strain error for the same mesh but using GI was 1.2×10^{-5}. For values of $e = 0.25$ and 0.5, M-SCNI gives similar accuracy as 5-point quadrature, but at much less

computational expense.

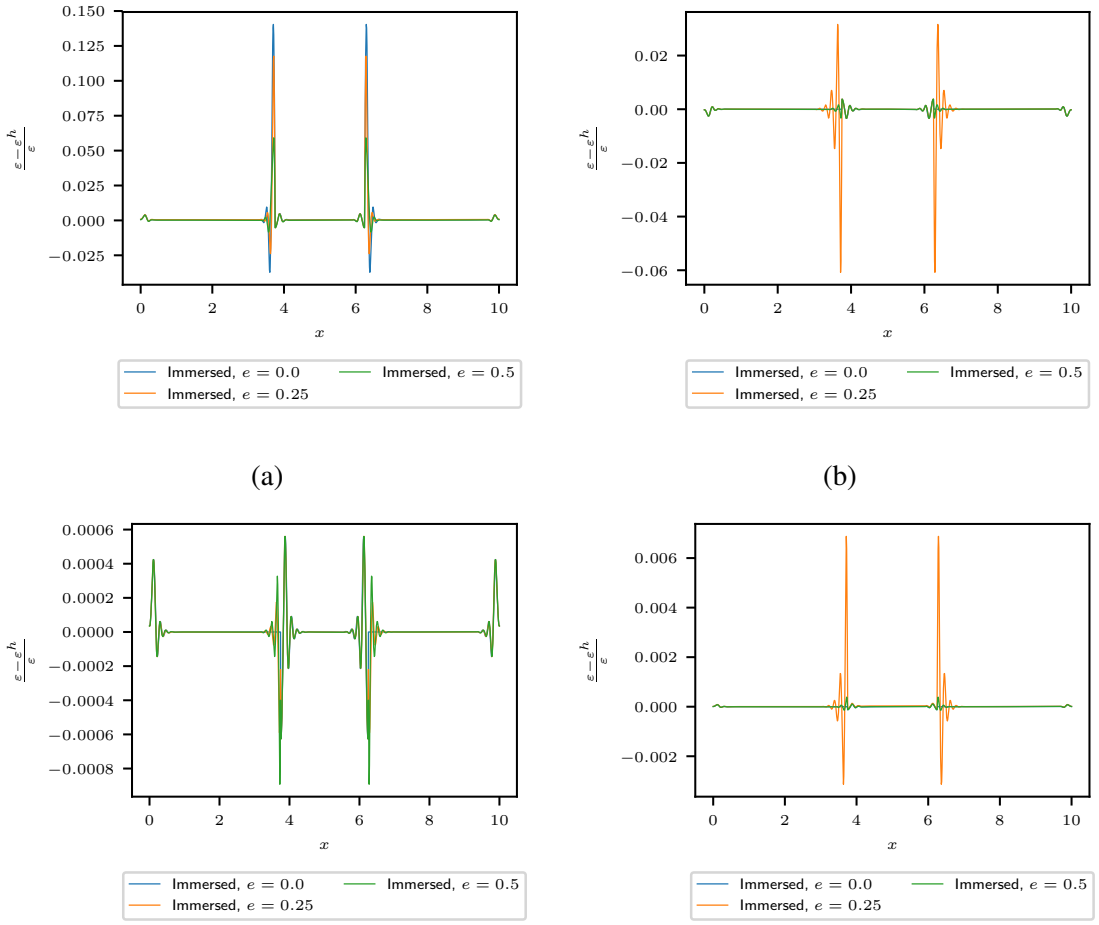

Figure 6.5: Strain fields of the composite rod with increasing number of Gauss quadrature points, $a = 2.00h$. (a) 1-point GI; (b) 2-point GI; (c) 3-point GI; (d) 4-point GI.

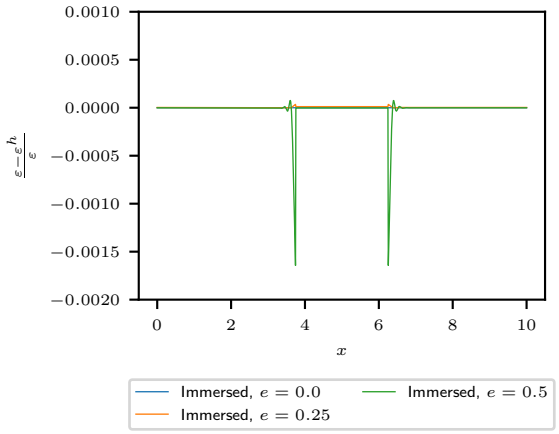

Figure 6.6: Normalized strain error of the composite rod with M-SCNI, $a = 2.0h$ with $c_L^K = 1.00$

Finally, for this 1D example the effect of kernel continuity is studied. Instead of the cubic B-spline kernel employed in the previous examples, the power kernel proposed in [75] is employed, given below.

$$\phi_a(x-x_I) = \begin{cases} (1-z)^p & 0 \le z \le 1.0 \\ 0 & z > 1.0 \end{cases} \quad \text{where } z = \frac{|x-x_I|}{a} \tag{6.2}$$

The power kernel is designed to be more localized for use in approximating the rough solutions. This kernel is only C^0 continuous and contains a derivative jump discontinuity at $z = 0$. Three values of $p = 6, 9$, and 12 are compared and given in Figure 6.7, again using M-SCNI. By increasing the value of p, the error in the strain field near the interface decreases due to the better approximation of the strain by introducing a discontinuity in background. Increasing the parameter p leads to increased localization and reduces the interpolation error across the strain discontinuity and the oscillations near the interface.

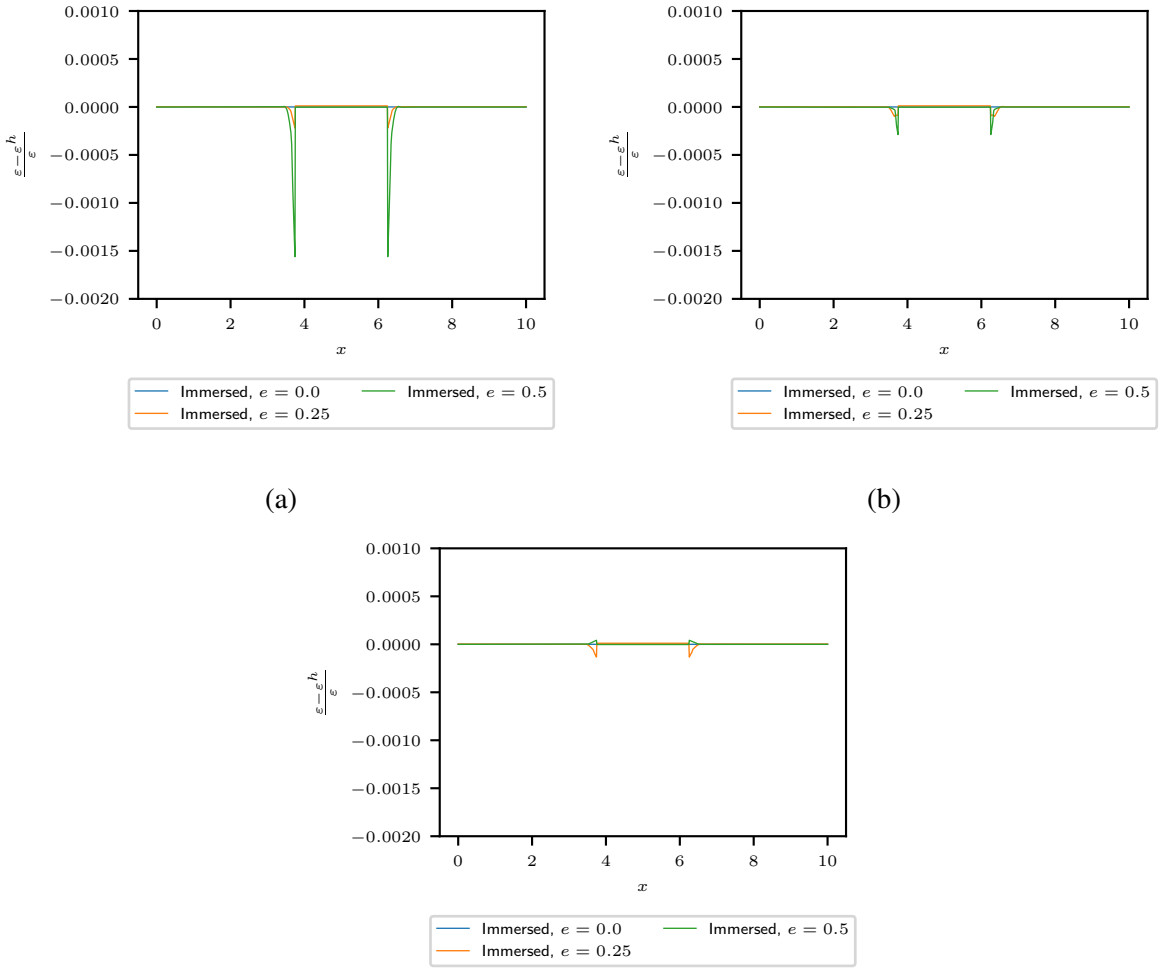

(a)

(b)

(c)

Figure 6.7: Strain fields of the composite rod using power kernel. (a) $p = 6$; (b) $p = 9$; (c) $p = 12$.

6.2 Circular Inclusion in an Infinite Plate Subject to Far-Field Tension

An infinite plate with a circular inclusion with radius R is subject to a far-field tension with magnitude P applied in the x-direction. The exact solution is given as follows [46]. Outside of the inclusion Ω^1, the stresses and their displacements are given by

$$\sigma_{rr} = \frac{P}{2}\left[1-\gamma_1\frac{R^2}{r^2}+\left(1-2\beta_1\frac{R^2}{r^2}-3\delta_1\frac{R^4}{r^4}\right)\cos 2\theta\right] \tag{6.3a}$$

$$\sigma_{\theta\theta} = \frac{P}{2}\left[1+\gamma_1\frac{R^2}{r^2}-\left(1-3\delta_1\frac{R^4}{r^4}\right)\cos 2\theta\right] \tag{6.3b}$$

$$\sigma_{r\theta} = -\frac{P}{2}\left(1+\beta_1\frac{R^2}{r^2}+3\delta_1\frac{R^4}{r^4}\right)\sin 2\theta \tag{6.3c}$$

$$u_r = \frac{PR}{8\mu_1}\left\{\left[\left(\kappa_1-1\right)\frac{r}{R}+2\gamma_1\frac{R}{r}\right]+\left[2\frac{r}{R}+\beta_1\left(\kappa_1+1\right)\frac{R}{r}+2\delta_1\frac{R^3}{r^3}\right]\cos 2\theta\right\} \tag{6.3d}$$

$$u_\theta = \frac{PR}{8\mu_1}\left[-2\frac{r}{R}-\beta_1\left(\kappa_1-1\right)\frac{R}{r}+2\delta_1\frac{R^3}{r^3}\right]\sin 2\theta \tag{6.3e}$$

where

$$\beta_1 = -\frac{2\left(\mu_2-\mu_1\right)}{\mu_1+\mu_2\kappa_1} \tag{6.4a}$$

$$\gamma_1 = \frac{\mu_1\left(\kappa_2-1\right)-\mu_2\left(\kappa_1-1\right)}{2\mu_2+\mu_1\left(\kappa_2-1\right)} \tag{6.4b}$$

$$\delta_1 = \frac{\mu_2-\mu_1}{\mu_1+\mu_2\kappa_1} \tag{6.4c}$$

and where $\kappa_i = 3 - 4\nu_i$ for plane strain and $\kappa_i = \frac{3-\nu_i}{1+\nu_i}$ for plane stress. The stresses and displacements inside of the inclusion Ω^2 are given by the following.

$$\sigma_{rr} = \frac{P}{2}\left(\beta_2 + \delta_2 \cos 2\theta\right) \tag{6.5a}$$

$$\sigma_{\theta\theta} = \frac{P}{2}\left(\beta_2 - \delta_2 \cos 2\theta\right) \tag{6.5b}$$

$$\sigma_{r\theta} = -\frac{P\delta_2}{2} \sin 2\theta \tag{6.5c}$$

$$u_r = \frac{Pr}{8\mu_2}\left[\beta_2\left(\kappa_2 - 1\right) + 2\delta_2 \cos 2\theta\right] \tag{6.5d}$$

$$u_\theta = -\frac{Pr\delta_2}{4\mu_2} \sin 2\theta \tag{6.5e}$$

where

$$\beta_2 = \frac{\mu_2\left(\kappa_1 + 1\right)}{2\mu_2 + \mu_1\left(\kappa_2 - 1\right)} \tag{6.6a}$$

$$\delta_2 = \frac{\mu_2\left(\kappa_1 + 1\right)}{\mu_1 + \mu_2\kappa_1} \tag{6.6b}$$

with κ_i as defined before. Eqs. (6.3) to (6.6) above correspond to a case where the inclusion is welded to the outer matrix.

The problem is modeled with a finite domain with dimension 4.0×4.0 using immersed RKPM with the exact displacement prescribed on the boundary as an essential boundary condition. The discretizations of the individual domains over the background and foreground are given in Figure 6.8a and Figure 6.8b, respectively. Nitsche's parameter $\beta = 100E_1/h$ is employed over the boundary Γ_g and $\gamma = 10E_1/h$ over the material interface, Γ^I. The inclusion is given a radius $R = 1.0$ and the far-field tension is $P = 100.0$. Material constants $E_1 = 1000.0$ and $\nu_1 = 0.30$ were selected for the matrix and $E_2 = 10000.0$ and $\nu_2 = 0.30$ were selected for the inclusion. Linear basis is used with quadratic B-spline kernels for the construction of the RK shape functions and 8×8 Gauss quadrature is employed over background integration cells.

As in the 1D example above, the effects of support size were also investigated in the 2D inclusion problem. The problem was modeled with varying support sizes for both the background and foreground inclusions and are given below in Figure 6.9. In this example, the results agree well with the exact solution regardless of the nodal support size, with only minor oscillations occurring when $a_1/h_1 = 3.0$ and $a_2/h_2 = 1.5$.

As is well known, the value of Nitsche's stabilization parameter γ can influence the coercivity of the solution. For methods which have constant strain over the integration domain (i.e. triangular elements) this value is given by a closed form solution. For other methods though with arbitrary strain fields, the value of γ is bounded by the maximum eigenvalue given by the coercivity condition. Typical values are on the order of E_1/h or E_2/h. For this example, three values of the Nitsche parameter $\gamma = 2.0E_1/h, 10E_1/h$, and $100E_1/h$ are investigated with support $a/h = 1.0$ and shown in Figure 6.10. The results show that favorable results are given for $\gamma = 2.0E_1/h$. As the stabilization parameter increases, it becomes the dominant term and the method behaves similar to the penalty method.

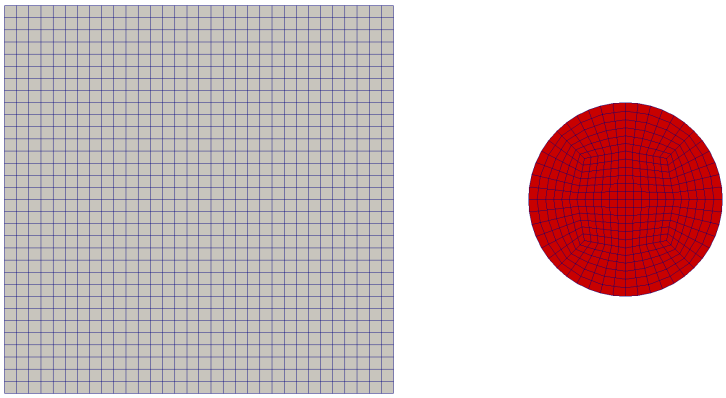

(a) (b)

Figure 6.8: Discretization of circular inclusion in an infinite plate. (a) Discretization of the background and (b) discretization of the foreground.

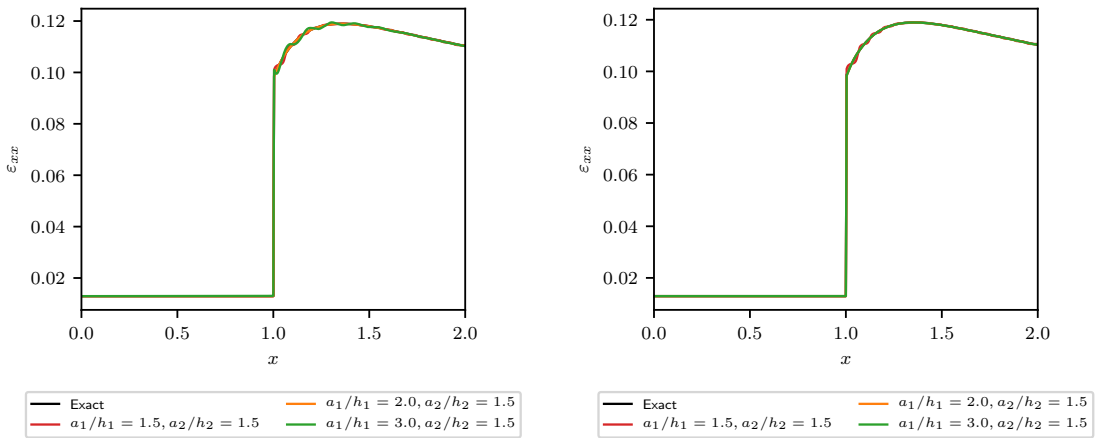

(a) (b)

Figure 6.9: ε_{xx} along line $y = 0$ with varying normalized supports. In (a) a_1/h_1 varies, a_2/h_2 held constant, and in (b) a_1/h_1 held constant, a_2/h_2 varies.

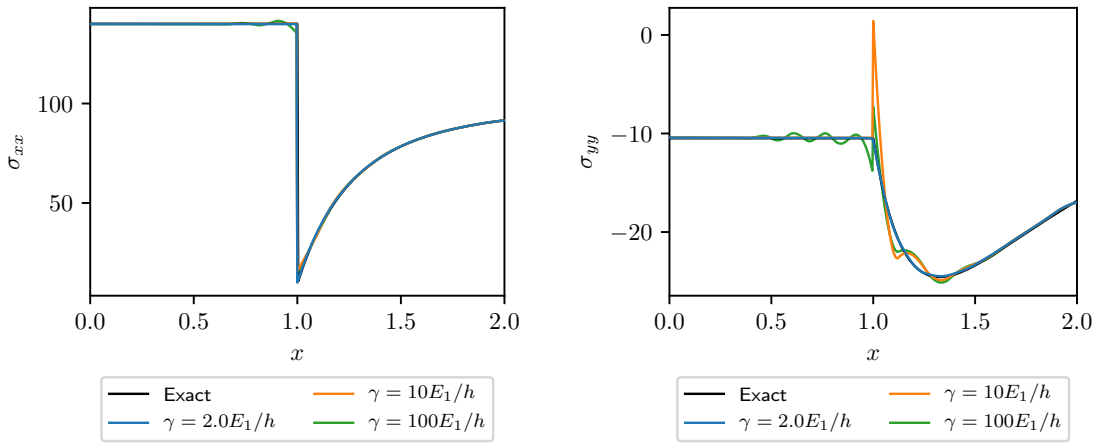

(a) (b)

Figure 6.10: Stress field with varying γ, 8-point GI. (a) σ_{xx} along line $x = 0$; (b) σ_{yy} along line $x = 0$

To determine the effect of quadrature order, the response with 2-point, 4-point, and 8-point Gauss quadrature is studied, and the stress results are given in Figure 6.11. As before, a low order of quadrature results in spurious, unphysical behavior with significant error in the stress results. Increasing to 4-point and 8-point GI removes much of this error.

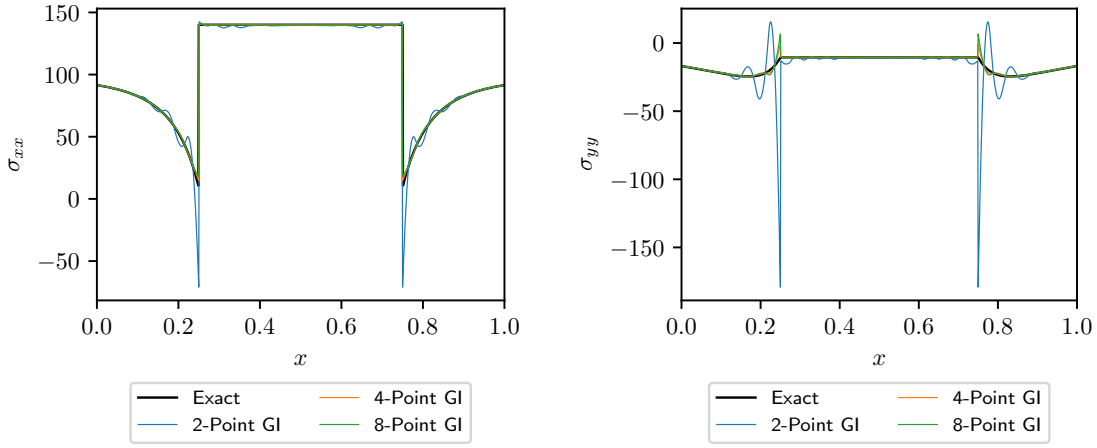

(a) (b)

Figure 6.11: Stress field with varying quadrature order. (a) σ_{xx} along line $x = 0$; (b) σ_{yy} along line $x = 0$

8-point GI was necessary above to achieve the accuracy desired. Using such a high number of integration points is undesirable as it adds significant cost computationally especially when solving problems in three dimensions. To study the effect of integration, the inclusion problem under tension was also simulated using M-SCNI. Figure 6.12 shows the results when using M-SCNI as the domain integration and is compared to GI. Here, M-SCNI is shown to give similar accuracy to GI.

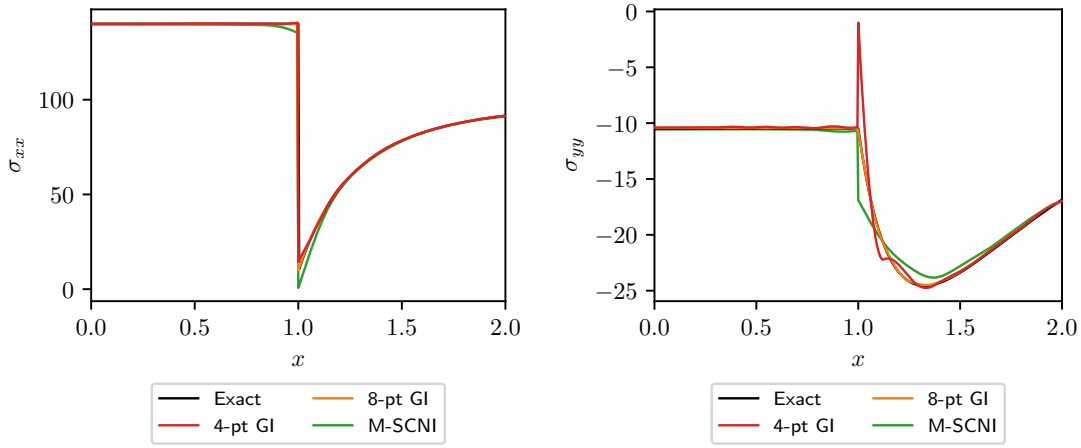

(a) (b)

Figure 6.12: Comparison of GI and M-SCNI along $x = 0$. (a) σ_{xx} comparison and (b) σ_{yy} comparison.

Finally, the convergence of displacement L_2 and energy error norms was carried out and the results are given in Figures 6.13a and 6.13b. 5-point Gauss quadrature is employed for the calculation of L_2 and energy error norms. Using 5-pt GI and an RK approximation with linear bases, near optimal rate of convergence of 2.0 is observed in the L_2 norm, and the energy norm convergence rate of 1.96 is faster than the optimal rate of 1.0 at the last refinement step. For comparison, the convergence is also investigated using M-SCNI as the integration method, which converges at a rate of 2.37 in the L_2 norm and 2.24 in the energy norm. This demonstrates the accuracy of the proposed immersed RKPM method in approximating both the displacements and stresses.

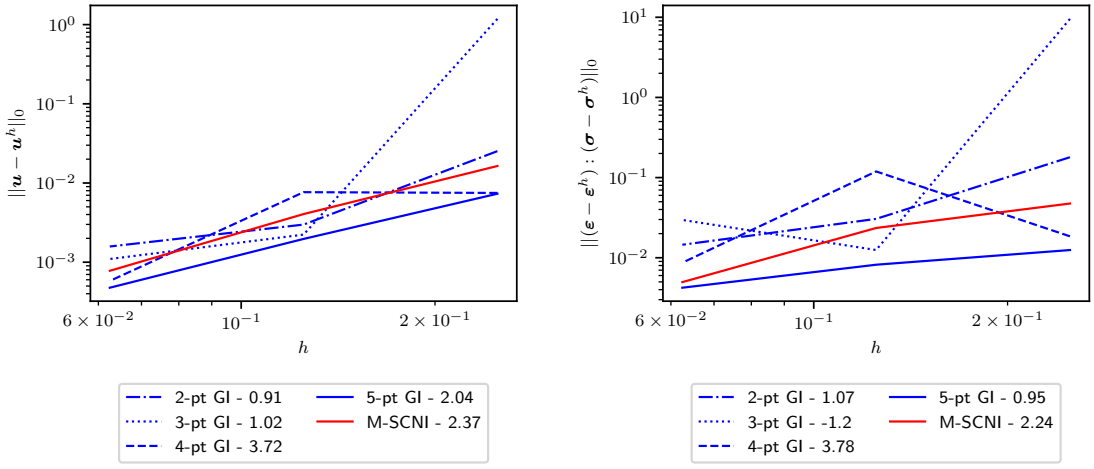

(a) (b)

Figure 6.13: Convergence rates of circular inclusion problem. (a) is the convergence in the L_2 norm and (b) is the convergence in the energy norm.

6.3 Multiple Inclusions Subject to Shear

A 1.0×1.0 unit square with multiple inclusions of varying radii is loaded as shown in Figure 6.14. The matrix is given material constants of $E_1 = 2.0 \times 10^9$ and $\nu_1 = 0.29$; the inclusions were given constants $E_2 = 2.0 \times 10^{10}$ and $\nu_2 = 0.29$. In Figure 6.14, the inclusion

domain is defined as the union of all the circular domains.

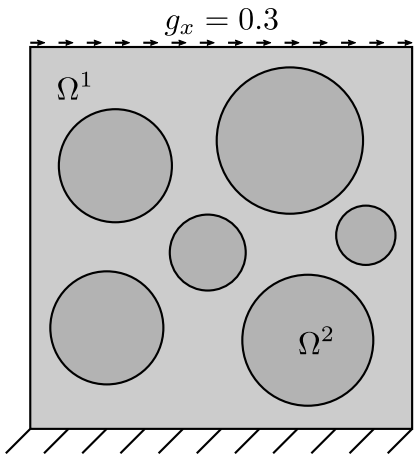

Figure 6.14: Simple shear with multiple inclusions

The RKPM approximation is constructed with linear basis functions and normalized supports of $a = 2.0h$. The background domain is uniformly discretized with 68×68 points and the inclusions are discretized with 4,235 points, and 8×8 Gauss integration is used. The discretizations of each body taken separately are shown in Figure 6.15. The values of $\beta = 100E_1/h$ and $\gamma = 2.0E_1/h$ are taken to enforce essential boundary conditions. It is emphasized the discretizations are not conforming at the interfaces between the two materials.

The displacement and shear strain fields are shown in Figure 6.16. Displacement continuity and strain discontinuities across the material interface are properly captured.

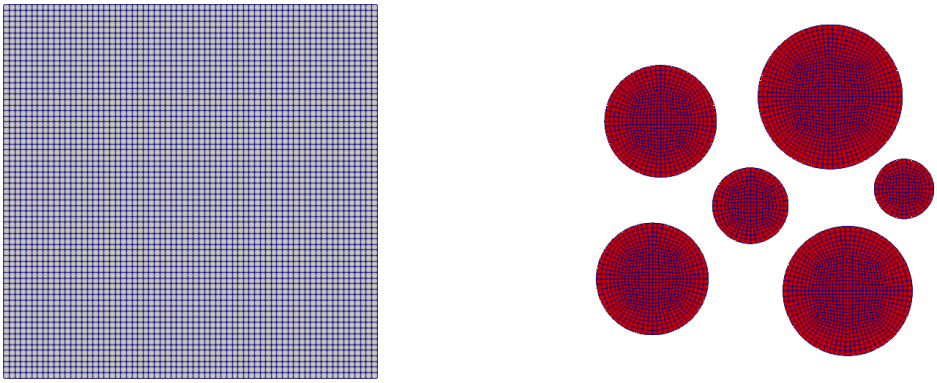

(a) (b)

Figure 6.15: Discretizations of matrix and reinforcing bodies shown separately. (a) Discretization of the background matrix; and (b) Discretization of the inclusions.

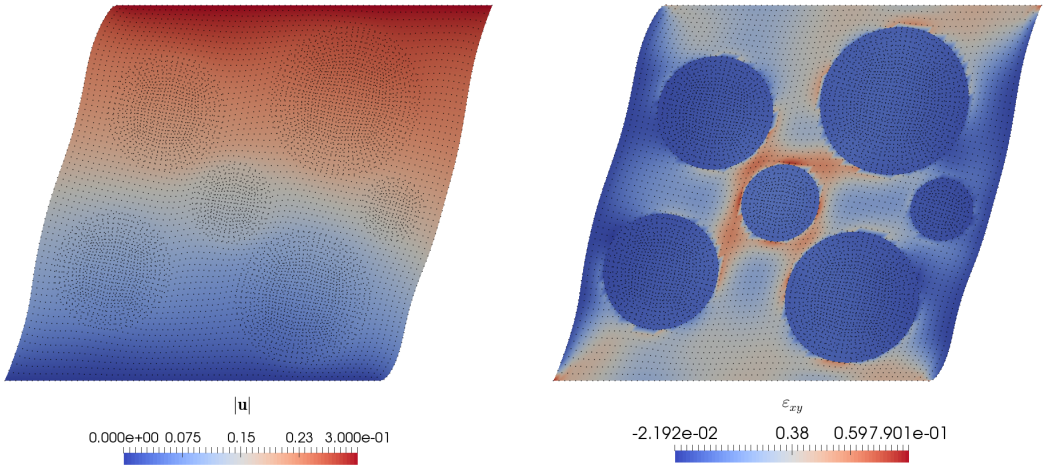

Figure 6.16: Displacement and strain fields of multiple inclusion problem, immersed RKPM

To determine the accuracy of immersed RKPM for this multiple inclusion example, it is compared to the FEM method. The FEM model is discretized with mesh size approximately equal to the nodal spacing of the immersed RKPM method. The displacement, stress, and strain fields along a horizontal line $y = 0.76$ are compared between both analyses, illustrated in Figure 6.19a through Figure 6.20b. The displacement solutions of the immersed RKPM agree well with the FEM analysis. Additionally, the discontinuities in the shear strain are properly captured by the proposed method with simple, non-conforming discretizations.

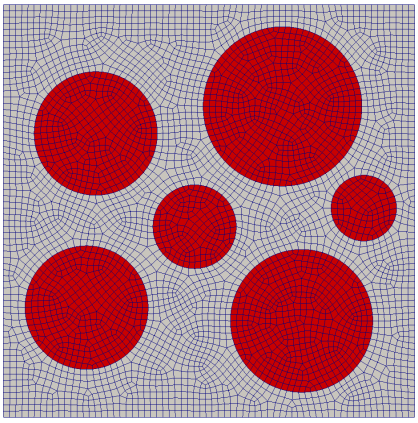

Figure 6.17: Conforming FEM mesh

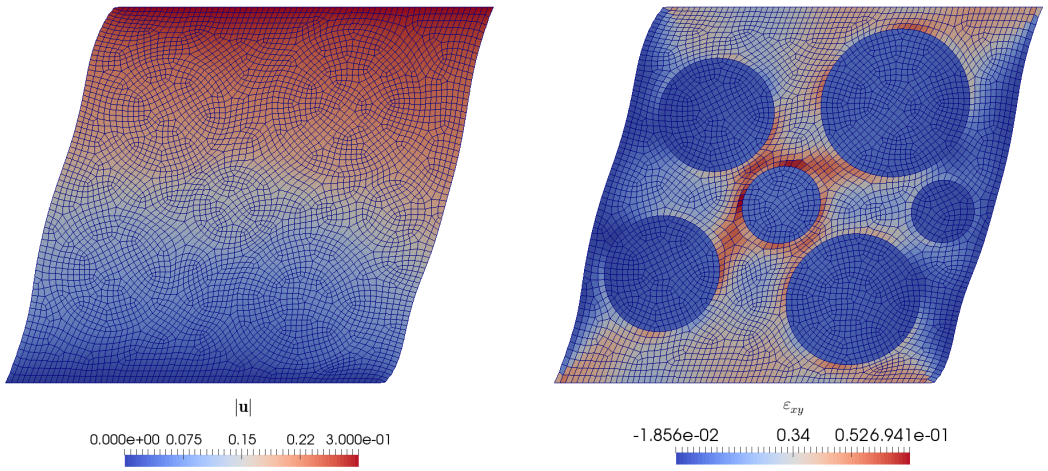

Figure 6.18: Displacement and strain fields of multiple inclusion problem, FEM

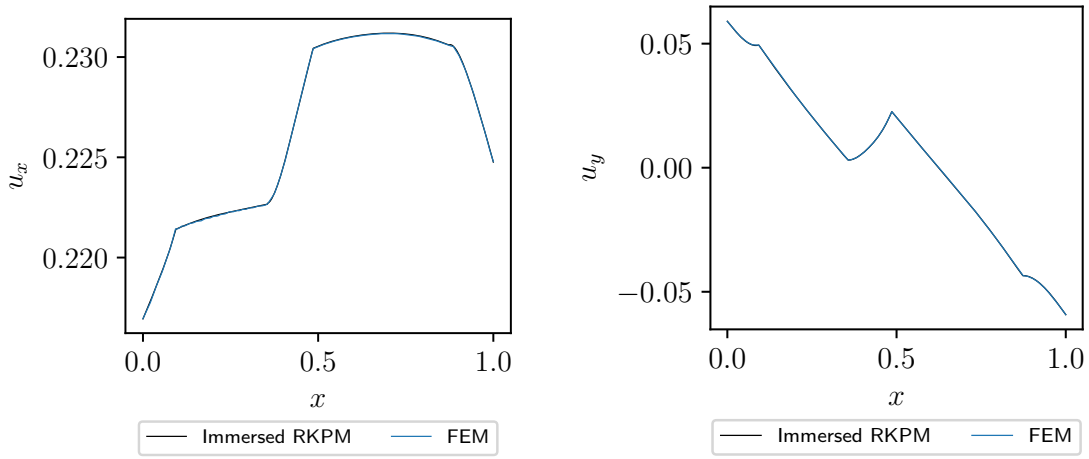

(a) (b)

Figure 6.19: Displacement comparison between immersed RKPM and FEM along $y = 0.76$. (a) u_x comparison; and (b) u_y comparison.

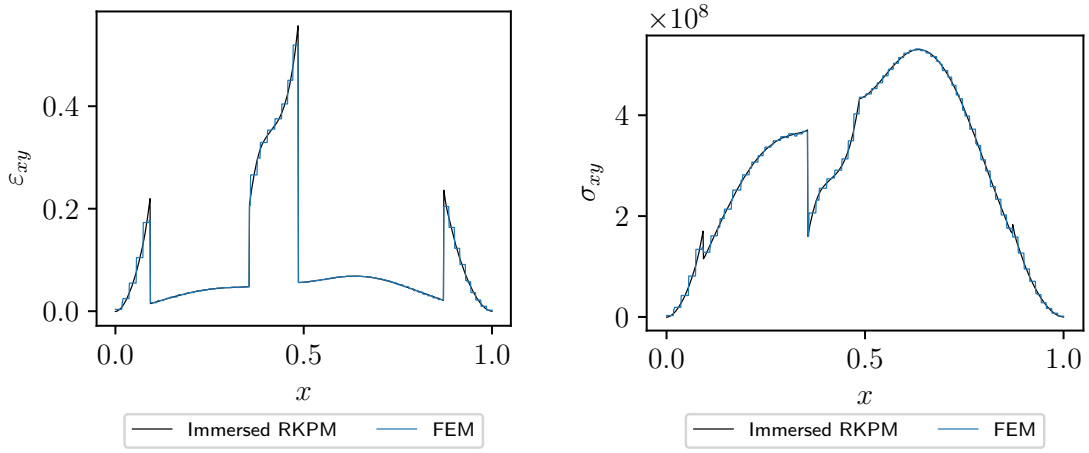

(a) (b)

Figure 6.20: Stress and strain comparison between immersed RKPM and FEM along $y = 0.76$. (a) ε_{xy} comparison; and (b) σ_{xy} comparison.

The results above were obtained again using 8-point Gauss quadrature over background cells. In total, shape functions and their derivatives were evaluated for 691,497 integration points, adding considerable expense to the immersed RKPM procedure. The problem is run again using M-SCNI with $c_L^K = 1.0$ for comparison and the results are shown in Figure 6.21. M-SCNI yields similar results compared to that obtained using Gauss integration, but at a much lower cost.

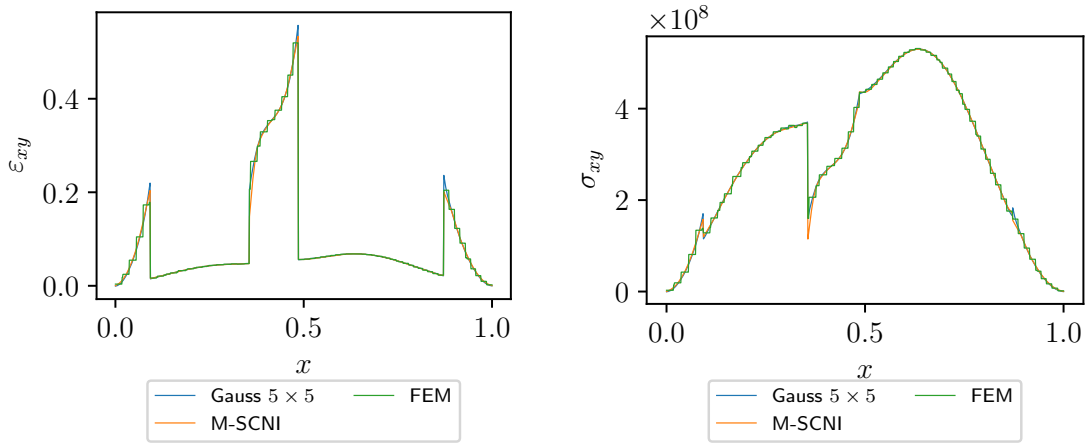

(a) (b)

Figure 6.21: Stress and strain comparison between 8-point GI, M-SCNI, and FEM along $y = 0.76$. (a) shows the ε_{xy} comparison; and (b) shows the σ_{xy} comparison.

6.4 3D Example with Cylindrical Inclusions

A block measuring $200 \times 200 \times 75$ in dimension with cylindrical inclusions is subject to tension by applying a prescribed displacement of $g_x = 10$ and $g_x = -10$ to the front and back surfaces of the block, respectively. Four cylindrical inclusions with radius $R = 12.5$ and length $L = 200$ are immersed with two cylinders aligned in the x-direction and two aligned in the y-direction. The cylinders in the x-direction are lowered vertically by 12.5 units and the cylinders in the y-direction are raised by 12.5 units with respect to the mid-plane such that the cylinders touch at the crossing zones. This arrangement produces an inclusion geometry which would be difficult to mesh under body-fitted schemes, and is likely to produce distorted meshes with large

aspect ratios near the crossing regions between the cylindrical inclusions. The background matrix is given material constants of $E_1 = 2.0 \times 10^9$ and $\nu_1 = 0.2$ and the cylindrical inclusions have material constants of $E_2 = 2.0 \times 10^{11}$ and $\nu_2 = 0.3$.

An average discretization size of $h = 4.0$ is chosen so that 110,902 nodes are discretized in the background and 24,424 nodes are discretized in the foreground inclusions. The background and foreground discretizations are shown in Figure 6.22. Linear basis with cubic B-splines is used with a normalized support $a = 2.0h$ for the RKPM approximation. M-SCNI is employed for integration and a stabilization coefficient of $c_L^K = 1.0$ is used to suppress low-energy modes in the solution. Nitsche's method is used to impose essential boundary conditions with $\beta = 500.0E_1/h$ and $\gamma = 2.0E_1/h$ for the interface. Note that the ends of the inclusions extend to the essential boundary and as such Nitsche's method is applied to both the background and foreground.

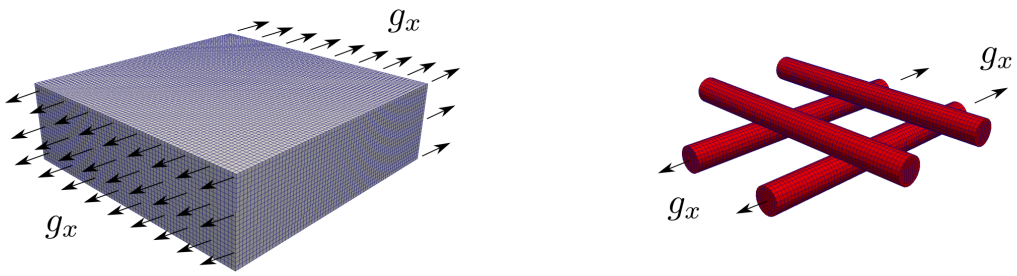

(a) (b)

Figure 6.22: Background and foreground discretizations of 3D immersed cylinder example. (a) shows the background discretization and (b) shows the foreground discretization.

The magnitude of displacement and the von Mises stress are shown in Figure 6.23, and are also shown in the y-plane with $y = -50$ in Figure 6.24. Due to the loading conditions and the difference in material stiffness between the two materials, the stress is concentrated in the inclusions parallel to the x-direction. The stresses are well resolved despite the relatively coarse discretization. Only marginal oscillations near the material interface on the essential boundary are present and diminish with refinement.

A comparison is made with a FEM model for reference. Due to the nature of the crossing

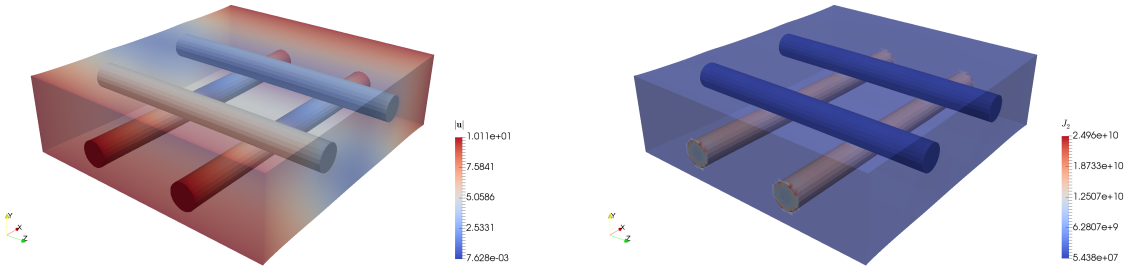

(a) (b)

Figure 6.23: Stress and displacement of 3D inclusion cylindrical inclusions. (a) shows the displacement magnitude $|\boldsymbol{u}|$ and (b) shows the von Mises stress, J_2.

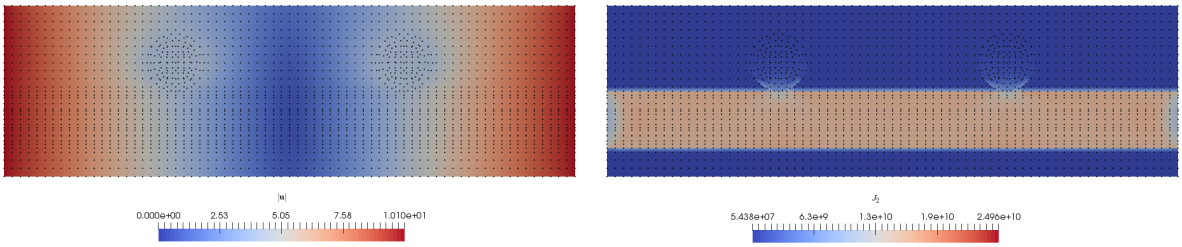

(a) (b)

Figure 6.24: Displacement and von Mises stress along the plane $y = -50$. (a) shows the displacement magnitude and (b) shows the J_2 stress. Note, these are plotted on the undeformed configuration.

geometries, a hexahedral mesh could not be generated. A tetrahedral mesh with constant strain elements was generated but the aspect ratio of the tetrahedral elements in those regions exceeded a value of 31.3, indicating poor quality elements in those regions. An element size is chosen to be approximately equal to the nodal spacing of the immersed RKPM model, resulting in 170,335 nodes and 976,550 elements generated. The mesh is shown in Figure 6.25 and the FEM results are obtained using ABAQUS.

The displacement components are compared between FEM and immersed RKPM in Figure 6.26 to Figure 6.28. The displacement solution of the immersed RKPM method agrees very well with the FEM mesh using tetrahedral elements, which is tedious to discretize with the given geometry.

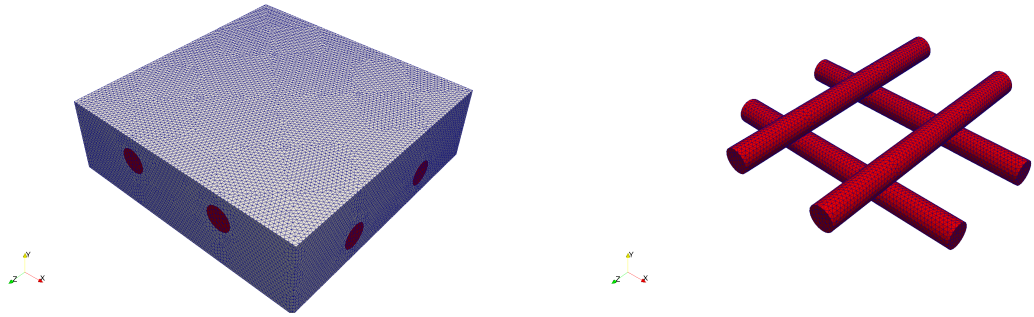

(a) (b)

Figure 6.25: FEM tetrahedral element mesh. (a) shows the tetrahedral mesh of the whole domain and (b) shows the tetrahedral mesh of the cylindrical inclusions.

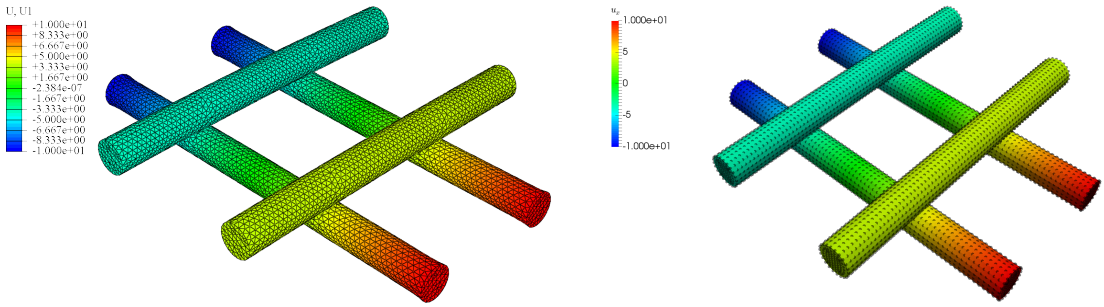

(a) (b)

Figure 6.26: u_x comparison between FEM (a) and immersed RKPM (b).

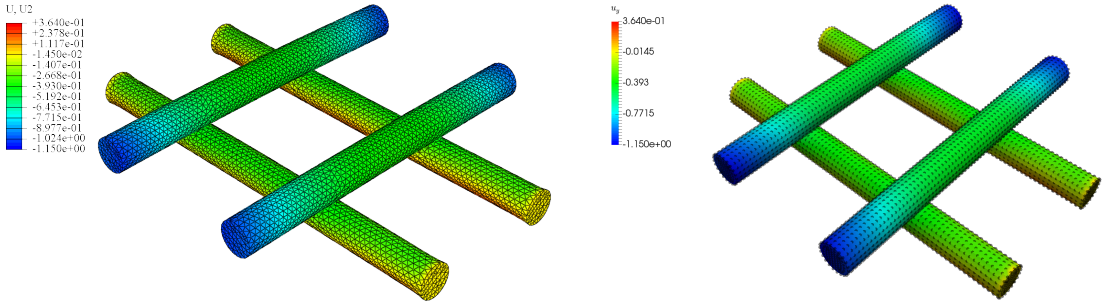

(a) (b)

Figure 6.27: u_y comparison between FEM (a) and immersed RKPM (b).

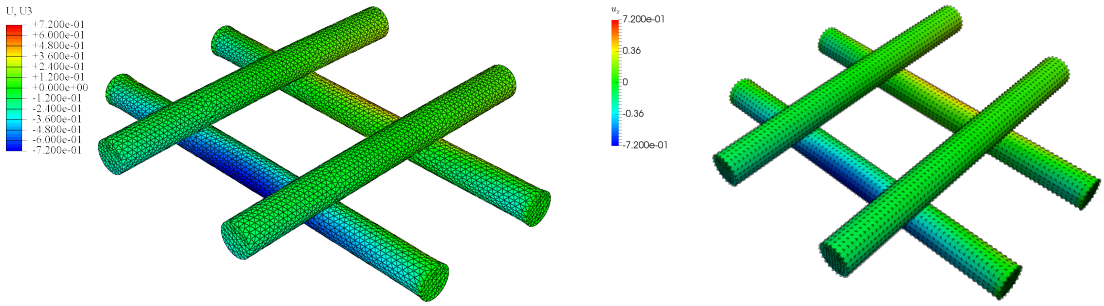

(a) (b)

Figure 6.28: u_z comparison between FEM (a) and immersed RKPM (b).

Acknowledgements

This chapter is currently being prepared for submission for publication of the material. F. Beckwith, J.S. Chen, and H. Wei, “An Immersed Reproducing Kernel Particle Method for Modeling Inhomogeneous Media.” The dissertation author was the primary investigator of this material.

Chapter 7

Immersed RKPM for Damage Analysis of Inhomogeneous Materials

In this section, the immersed RKPM method is extended to nonlinear heterogeneous media under the updated Lagrangian framework, in which the Cauchy stress and the energy conjugate strain are introduced, and both material and geometric nonlinearities are considered. This formulation can then be degenerated into problems dominated by material nonlinearity with very localized responses, such as damage near the material interfaces. The updated Lagrangian formulation discussed herein uses the current configuration as the reference configuration, and the RK approximation is also constructed in the current configuration, leading to the so called semi-Lagrangian formulation [21, 37]. In the following, the material point located at $\mathbf{X}$ in the undeformed configuration is mapped to $\mathbf{x} = \mathbf{x}(\mathbf{X}, t)$ in the deformed configuration, where t is the real or pseudo time.

7.1 Nonlinear Equations for the Immersed Formulation

The weak form for the immersed formulation under an updated Lagrangian framework is stated as follows: Given $\boldsymbol{b}^1$, $\boldsymbol{b}^2$, $\boldsymbol{h}$, and $\boldsymbol{g}$, find $\boldsymbol{u}^1, \boldsymbol{u}^2 \in \mathcal{U}^1 \times \mathcal{U}^2$ such that

$$\delta U = \delta W^{int} - \delta W^{ext} + \delta U^I + \delta U^{int,EB} - \delta U^{ext,EB} = 0 \tag{7.1a}$$

$$\delta W^{int} = \int_{\Omega_x} \delta\boldsymbol{\varepsilon}^1 : \boldsymbol{\sigma}^1 \, \mathrm{d}\Omega + \int_{\Omega_x^2} \left(\delta\boldsymbol{\varepsilon}^2 : \boldsymbol{\sigma}^2 - \delta\boldsymbol{\varepsilon}^1 : \boldsymbol{\sigma}^1 \right) \mathrm{d}\Omega \tag{7.1b}$$

$$\delta U^I = -\int_{\Gamma_x^I} [\![\delta\boldsymbol{u}]\!] \cdot \langle \boldsymbol{\sigma} \rangle \cdot \boldsymbol{n}^1 \, \mathrm{d}\Gamma - \int_{\Gamma_x^I} \langle \delta\boldsymbol{\sigma} \rangle \cdot \boldsymbol{n}^1 \cdot [\![\boldsymbol{u}]\!] \, \mathrm{d}\Gamma + \gamma \int_{\Gamma_x^I} [\![\delta\boldsymbol{u}]\!] \cdot [\![\boldsymbol{u}]\!] \, \mathrm{d}\Gamma \tag{7.1c}$$

$$\delta W^{ext} = \int_{\Omega_x} \delta\boldsymbol{u}^1 \cdot \boldsymbol{b}^1 \, \mathrm{d}\Omega + \int_{\Omega_x^2} \left(\delta\boldsymbol{u}^2 \cdot \boldsymbol{b}^2 - \delta\boldsymbol{u}^1 \cdot \boldsymbol{b}^1 \right) \mathrm{d}\Omega + \int_{\Gamma_x^h} \delta\boldsymbol{u}^1 \cdot \boldsymbol{h} \, \mathrm{d}\Gamma \tag{7.1d}$$

$$\delta U^{int,EB} = -\int_{\Gamma_x^g} \delta\boldsymbol{\sigma}^1 \cdot \boldsymbol{n}^1 \cdot \boldsymbol{u}^1 \, \mathrm{d}\Gamma - \int_{\Gamma_x^g} \delta\boldsymbol{u}^1 \cdot \boldsymbol{\sigma}^1 \cdot \boldsymbol{n}^1 \, \mathrm{d}\Gamma + \beta \int_{\Gamma_x^g} \delta\boldsymbol{u}^1 \cdot \boldsymbol{u}^1 \, \mathrm{d}\Gamma \tag{7.1e}$$

$$\delta U^{ext,EB} = -\int_{\Gamma_x^g} \delta\boldsymbol{\sigma}^1 \cdot \boldsymbol{n}^1 \cdot \boldsymbol{g} \, \mathrm{d}\Gamma + \beta \int_{\Gamma_x^g} \delta\boldsymbol{u}^1 \cdot \boldsymbol{g} \, \mathrm{d}\Gamma \tag{7.1f}$$

for all $\delta\boldsymbol{u}^1, \delta\boldsymbol{u}^2 \in \mathcal{V}^1 \times \mathcal{V}^2$, where the test and trial spaces are defined as:

$$\mathcal{U}^i = \{ \boldsymbol{u}^i \mid \boldsymbol{u}^i \in H_g^1(\Omega^i), \boldsymbol{u}^i = \boldsymbol{g} \text{ on } \Gamma_x^g \} \tag{7.2a}$$

$$\mathcal{V}^i = \{ \delta\boldsymbol{u}^i \mid \delta\boldsymbol{u}^i \in H_0^1(\Omega^i), \delta\boldsymbol{u}^i = \boldsymbol{0} \text{ on } \Gamma_x^g \} \tag{7.2b}$$

for $i = 1, 2$. Here, the subscript "x" in the domain and boundary terms denotes fields in the current configuration, whereas the subscript "0" in the domain and boundary terms denotes fields in the reference configuration.

The Galerkin form is derived by following the formulation given in Section 4.3.1. In both linear and nonlinear problems, the Galerkin approximation of the immersed approach leads to the following discrete equilibrium equations after introducing RK approximations in the background and foreground discretizations.

$$\begin{bmatrix} \boldsymbol{f}^{int}(\boldsymbol{u}^h, \tilde{\boldsymbol{u}}^h) \\ \tilde{\boldsymbol{f}}^{int}(\boldsymbol{u}^h, \tilde{\boldsymbol{u}}^h) \end{bmatrix} = \begin{bmatrix} \boldsymbol{f}^{ext} \\ \tilde{\boldsymbol{f}}^{ext} \end{bmatrix} \tag{7.3}$$

In linear problems, $\boldsymbol{f}^{int}$ and $\tilde{\boldsymbol{f}}^{int}$ are not functions of the displacements $\boldsymbol{u}^h$ and $\tilde{\boldsymbol{u}}^h$, while for nonlinear problems they are in general functions of the displacements. Since these are nonlinear equations, linearization of the weak form in (7.1) is required.

7.1.1 Linearization of the Immersed Formulation

To satisfy equilibrium between the internal and external forces for nonlinear problems, the weak form in (7.1) must be linearized. Following Chen et al. [15], the weak form is expressed in an incremental format as follows:

$$\Delta\left(\delta W^{int} + \delta U^{I} + \delta U^{int,EB}\right) = \left(\delta W^{ext} + \delta U^{ext,EB}\right)_{n+1} - \left(\delta W^{int} + \delta U^{I} + \delta U^{int,EB}\right)_{n+1}^{\nu+1} \tag{7.4}$$

where $n+1$ is the next load step to be solved and ν is the iteration index.

The linearization of the bulk terms given by $\Delta(\delta W^{int})$ involves both material and geometric nonlinearities:

$$\Delta(\delta W^{int}) = \Delta(\delta W^{int})^{\text{mat}} + \Delta(\delta W^{int})^{\text{geo}} \tag{7.5a}$$

$$\Delta(\delta W^{int})^{\text{mat}} = \int_{\Omega_x} \delta\boldsymbol{\varepsilon}^1 : \boldsymbol{D}^1 : \Delta\boldsymbol{\varepsilon}^1 \, \mathrm{d}\Omega + \int_{\Omega_x^2} \left(\delta\boldsymbol{\varepsilon}^2 : \boldsymbol{D}^2 : \Delta\boldsymbol{\varepsilon}^2 - \delta\boldsymbol{\varepsilon}^1 : \boldsymbol{D}^1 : \Delta\boldsymbol{\varepsilon}^1\right) \mathrm{d}\Omega \tag{7.5b}$$

$$\Delta(\delta W^{int})^{\text{geo}} = \int_{\Omega_x} \delta\boldsymbol{\varepsilon}^1 : \boldsymbol{T}^1 : \Delta\boldsymbol{\varepsilon}^1 \, \mathrm{d}\Omega + \int_{\Omega_x^2} \left(\delta\boldsymbol{\varepsilon}^2 : \boldsymbol{T}^2 : \Delta\boldsymbol{\varepsilon}^2 - \delta\boldsymbol{\varepsilon}^1 : \boldsymbol{T}^1 : \Delta\boldsymbol{\varepsilon}^1\right) \mathrm{d}\Omega \tag{7.5c}$$

where $\boldsymbol{D}^m$ is the material response tensor for material $m = 1, 2$, T^m_{ijkl} is the geometric response tensor defined in Table 7.1, σ^m_{ij} is the Cauchy stress component, and $\varepsilon_{ij} = u_{(i,j)} = (u_{i,j} + u_{j,i})/2$ is the conjugate strain. Comma notation has been employed with $(\cdot)_{,i} = \partial(\cdot)/\partial x_i$.

The Nitsche terms in δU^I and δW^{EB} are similar to follower loads in that they effectively

apply a traction to the current interface configuration. As such, the linearization of the interface and essential boundary terms involves several terms. Consider a single integral from δU^I. By employing Nanson's relationship, the boundary integral over the interface is mapped to the undeformed configuration over Γ_0^I.

$$\delta U^{I,1} = -\int_{\Gamma_x^I} [\![\delta \boldsymbol{u}]\!] \cdot \boldsymbol{n}^1 \cdot \langle \boldsymbol{\sigma} \rangle \, \mathrm{d}\Gamma = -\int_{\Gamma_0^I} [\![\delta \boldsymbol{u}]\!] \cdot \boldsymbol{n}^1 \cdot \langle \boldsymbol{\sigma} \rangle \, \boldsymbol{F}^{-1} J^S \, \mathrm{d}\Gamma = -\int_{\Gamma_0^I} [\![\delta \boldsymbol{u}]\!] \cdot \boldsymbol{n}_0^1 \cdot \langle \boldsymbol{\sigma} \rangle \, \boldsymbol{F}^{-1} \, \mathrm{d}\Gamma \tag{7.6}$$

where J^S above is the surface Jacobian that maps the reference area to the current area and $\boldsymbol{F}$ is the deformation gradient and the term $\boldsymbol{n}_0^1 = \boldsymbol{n}^1 J^S$. Linearization may now proceed by taking an increment of each term in the integrand above.

$$\begin{aligned} \Delta\left(\delta U^{I,1}\right) = &-\int_{\Gamma_0^I} [\![\delta \boldsymbol{u}]\!] \cdot \Delta \boldsymbol{n}_0^1 \cdot \langle \boldsymbol{\sigma} \rangle \, \boldsymbol{F}^{-1} \, \mathrm{d}\Gamma - \int_{\Gamma_0^I} [\![\delta \boldsymbol{u}]\!] \cdot \boldsymbol{n}_0^1 \cdot \langle \Delta \boldsymbol{\sigma} \rangle \, \boldsymbol{F}^{-1} \, \mathrm{d}\Gamma \\ &- \int_{\Gamma_0^I} [\![\delta \boldsymbol{u}]\!] \cdot \boldsymbol{n}_0^1 \cdot \langle \boldsymbol{\sigma} \rangle \, \Delta \boldsymbol{F}^{-1} \, \mathrm{d}\Gamma \end{aligned} \tag{7.7}$$

where $\Delta\boldsymbol{\sigma} = \boldsymbol{C} : \Delta\boldsymbol{\varepsilon} + \boldsymbol{S} : \Delta\boldsymbol{\omega}$, and $\Delta\omega_{ij} = \Delta u_{[i,j]}$ is the skew symmetric part of the strain increment defined as $u_{[i,j]} = (u_{i,j} - u_{j,i})/2$, and $\boldsymbol{C}$ and $\boldsymbol{S}$ for the Truesdell stress rate are given in Table 7.1. Index notation and summation convention has been employed where a sum is implied over repeated indices. Here, the term $\Delta\boldsymbol{n}_0^1$ has been ignored similar to that often done in the follower load problem to omit the stiffness matrix associated with the follower load.

Similarly, for the increment of $\delta U^{I,2}$ is as follows:

$$\begin{aligned} \Delta\left(\delta U^{I,2}\right) = &-\int_{\Gamma_0^I} \langle \delta \boldsymbol{\sigma} \rangle \cdot \Delta \boldsymbol{n}_0^1 \cdot [\![\boldsymbol{u}]\!] \boldsymbol{F}^{-1} \, \mathrm{d}\Gamma - \int_{\Gamma_0^I} \langle \delta \boldsymbol{\sigma} \rangle \cdot \boldsymbol{n}_0^1 \cdot [\![\Delta \boldsymbol{u}]\!] \boldsymbol{F}^{-1} \, \mathrm{d}\Gamma \\ &- \int_{\Gamma_0^I} \langle \delta \boldsymbol{\sigma} \rangle \cdot \boldsymbol{n}_0^1 \cdot [\![\boldsymbol{u}]\!] \Delta \boldsymbol{F}^{-1} \, \mathrm{d}\Gamma \end{aligned} \tag{7.8}$$

Table 7.1: Stress increment and response tensors in updated Lagrangian formulation

Cauchy Stress	σ_{ij}
Cauchy Stress increment	$\Delta\sigma_{ij} = C_{ijkl}\Delta u_{(k,l)} + S_{ijkl}\Delta u_{[k,l]}$ $C_{ijkl} = C^t_{ijkl} + C^*_{ijkl}$ $S_{ijkl} = \frac{1}{2}\left(\sigma_{il}\delta_{jk} + \sigma_{jl}\delta_{ik} - \sigma_{ik}\delta_{jl} - \sigma_{jk}\delta_{il}\right)$ C^t_{ijkl}, determined experimentally $C^*_{ijkl} = -\sigma_{ij}\delta_{kl} + \frac{1}{2}\left(\sigma_{il}\delta_{jk} + \sigma_{jl}\delta_{ik} + \sigma_{ik}\delta_{jl} + \sigma_{jk}\delta_{il}\right)$
Material and geometric response tensors	$D_{ijkl} = C^t_{ijkl}$ $T_{ijkl} = \delta_{ik}\sigma_{jl}$

Finally, the linearization of the stabilization term at the interface is:

$$\Delta\left(\delta U^{I,3}\right) = \gamma\int_{\Gamma_0^I}[\![\delta\boldsymbol{u}]\!]\cdot[\![\Delta\boldsymbol{u}]\!]J^S\,\mathrm{d}\Gamma + \gamma\int_{\Gamma_0^I}[\![\delta\boldsymbol{u}]\!]\cdot[\![\boldsymbol{u}]\!]\Delta J^S\,\mathrm{d}\Gamma \tag{7.9}$$

The linearization of the essential boundary terms follows the same procedure as the linearization of the interface, and are given below for completeness.

$$\begin{aligned}\Delta\left(\delta W^{int,EB,1}\right) = &-\int_{\Gamma_0^g}\delta\boldsymbol{u}^m\cdot\Delta\boldsymbol{n}_0^m\cdot\boldsymbol{\sigma}^m\boldsymbol{F}^{-1}\,\mathrm{d}\Gamma - \int_{\Gamma_0^g}\delta\boldsymbol{u}^m\cdot\boldsymbol{n}_0^m\cdot\Delta\boldsymbol{\sigma}^m\boldsymbol{F}^{-1}\,\mathrm{d}\Gamma \\ &-\int_{\Gamma_0^g}\delta\boldsymbol{u}^m\cdot\boldsymbol{n}_0^m\cdot\boldsymbol{\sigma}^m\Delta\boldsymbol{F}^{-1}\,\mathrm{d}\Gamma\end{aligned} \tag{7.10}$$

$$\begin{aligned}\Delta\left(\delta W^{int,EB,2}\right) = &-\int_{\Gamma_0^g}\delta\boldsymbol{\sigma}^m\cdot\Delta\boldsymbol{n}_0^m\cdot\boldsymbol{u}^m\boldsymbol{F}^{-1}\,\mathrm{d}\Gamma - \int_{\Gamma_0^g}\delta\boldsymbol{\sigma}^m\cdot\boldsymbol{n}_0^m\cdot\Delta\boldsymbol{u}^m\boldsymbol{F}^{-1}\,\mathrm{d}\Gamma \\ &-\int_{\Gamma_0^g}\delta\boldsymbol{\sigma}^m\cdot\boldsymbol{n}_0^m\cdot\boldsymbol{u}^m\Delta\boldsymbol{F}^{-1}\,\mathrm{d}\Gamma\end{aligned} \tag{7.11}$$

$$\Delta\left(\delta W^{int,EB,3}\right) = \beta^m\int_{\Gamma_0^g}\delta\boldsymbol{u}^m\cdot\Delta\boldsymbol{u}^m J^S\,\mathrm{d}\Gamma + \beta^m\int_{\Gamma_0^g}\delta\boldsymbol{u}^m\cdot\boldsymbol{u}^m\Delta J^S\,\mathrm{d}\Gamma \tag{7.12}$$

The notation m indicates which subdomain the above equations are applied to and has been included in the case where the inclusion may also be subject to essential boundary conditions.

The linearizations from the above formulas may then be combined to form a tangent stiffness, which will have both material and geometric components. It should be emphasized that although having a consistent tangent matrix will converge faster in the Newton-Raphson procedure, it is not necessary to approximate equilibrium in (7.3). With this in mind, one may choose to omit calculating the stiffness matrix at each iteration taking only the first stiffness. This simplifies the procedure while decreasing the overall expense of building a new stiffness matrix, albeit at an increased number of iterations.

7.1.2 Internal Force and Stiffness

The internal force consists of bulk terms given by the internal energy of the system, and Nitsche terms which enforce the interface conditions between the background material and the foreground inclusion. The enforcement of boundary conditions also contributes to the internal work. Together, the internal force is given as

$$\begin{bmatrix} \boldsymbol{f}^{int} \\ \tilde{\boldsymbol{f}}^{int} \end{bmatrix} = \begin{bmatrix} \boldsymbol{f}^{int,b} \\ \tilde{\boldsymbol{f}}^{int,b} \end{bmatrix} + \begin{bmatrix} \boldsymbol{f}^{int,N} \\ \tilde{\boldsymbol{f}}^{int,N} \end{bmatrix} + \begin{bmatrix} \boldsymbol{f}^{int,EB} \\ \tilde{\boldsymbol{f}}^{int,EB} \end{bmatrix} \tag{7.13}$$

By introducing the approximations given by (4.15), (4.18), and (4.21) into the test functions $\delta\boldsymbol{u}^h$, $\delta\tilde{\boldsymbol{u}}^h$, and $\delta\hat{\boldsymbol{u}}^h$ of (7.1b), the discrete equations for the internal force are determined as follows:

$$\boldsymbol{f}_I^{int,b} = \int_{\Omega_x} \boldsymbol{B}_I^T \boldsymbol{\sigma}^1(\varepsilon^h)\,\mathrm{d}\Omega - \int_{\Omega_x^2} \hat{\boldsymbol{B}}_I^T \boldsymbol{\sigma}^1(\hat{\varepsilon}^h)\,\mathrm{d}\Omega \tag{7.14a}$$

$$\tilde{\boldsymbol{f}}_I^{int,b} = \int_{\Omega_x^2} \tilde{\boldsymbol{B}}_I^T \boldsymbol{\sigma}^2(\tilde{\varepsilon}^h)\,\mathrm{d}\Omega \tag{7.14b}$$

In a similar manner, (4.15) and (4.18) are used for the Nitsche terms in (7.1c). For the interface terms, the variation of stress $\delta\boldsymbol{\sigma}^m(\boldsymbol{u})$ is present. Following a displacement-based

formulation, this may be expressed as:

$$\delta\boldsymbol{\sigma}^1(\boldsymbol{u}^h) = \sum_{I\in S} \boldsymbol{D}^1 \boldsymbol{B}_I \delta\boldsymbol{u}_I \tag{7.15a}$$

$$\delta\boldsymbol{\sigma}^2(\tilde{\boldsymbol{u}}^h) = \sum_{I\in \tilde{S}} \boldsymbol{D}^2 \tilde{\boldsymbol{B}}_I \delta\tilde{\boldsymbol{u}}_I \tag{7.15b}$$

In the above, $\boldsymbol{D}^m$ is the consistent tangent according to the Truesdell stress rate for material m. Substituting these approximations and invoking the arbitrariness of $\delta\boldsymbol{u}_I$ and $\delta\tilde{\boldsymbol{u}}_I$ results in the following nodal forces from the interface terms.

$$\begin{aligned}\boldsymbol{f}_I^{int,N} = &\int_{\Gamma_x^I} \Psi_I \boldsymbol{\eta}^T (\alpha^1 \boldsymbol{\sigma}^1(\boldsymbol{\varepsilon}^h) + \alpha^2 \boldsymbol{\sigma}^2(\tilde{\boldsymbol{\varepsilon}}^h))\,\mathrm{d}\Gamma - \alpha^1 \int_{\Gamma_x^I} \boldsymbol{B}_I^T \boldsymbol{D}^1 \boldsymbol{\eta}(\tilde{\boldsymbol{u}}^h - \boldsymbol{u}^h)\,\mathrm{d}\Gamma \\ &-\gamma \int_{\Gamma_x^I} \Psi_I(\tilde{\boldsymbol{u}}^h - \boldsymbol{u}^h)\,\mathrm{d}\Gamma \end{aligned} \tag{7.16a}$$

$$\begin{aligned}\tilde{\boldsymbol{f}}_I^{int,N} = -&\int_{\Gamma_x^I} \tilde{\Psi}_I \boldsymbol{\eta}^T (\alpha^1 \boldsymbol{\sigma}^1(\boldsymbol{\varepsilon}^h) + \alpha^2 \boldsymbol{\sigma}^2(\tilde{\boldsymbol{\varepsilon}}^h))\,\mathrm{d}\Gamma - \alpha^2 \int_{\Gamma_x^I} \tilde{\boldsymbol{B}}_I^T \boldsymbol{D}^2 \boldsymbol{\eta}(\tilde{\boldsymbol{u}}^h - \boldsymbol{u}^h)\,\mathrm{d}\Gamma \\ &+\gamma \int_{\Gamma_x^I} \tilde{\Psi}_I(\tilde{\boldsymbol{u}}^h - \boldsymbol{u}^h)\,\mathrm{d}\Gamma \end{aligned} \tag{7.16b}$$

The internal force contributions from the essential boundary are treated similarly to the internal force from the interface conditions.

$$\boldsymbol{f}_I^{int,EB} = -\int_{\Gamma_x^g} \boldsymbol{B}_I^T \boldsymbol{D}^1 \boldsymbol{\eta} \boldsymbol{u}^h\,\mathrm{d}\Gamma - \int_{\Gamma_x^g} \Psi_I \boldsymbol{\eta}^T \boldsymbol{\sigma}^1(\boldsymbol{\varepsilon}^h)\,\mathrm{d}\Gamma + \beta^1 \int_{\Gamma_x^g} \Psi_I \boldsymbol{u}^h\,\mathrm{d}\Gamma \tag{7.17a}$$

$$\tilde{\boldsymbol{f}}_I^{int,EB} = -\int_{\Gamma_x^{g^2}} \tilde{\boldsymbol{B}}_I^T \boldsymbol{D}^2 \boldsymbol{\eta} \tilde{\boldsymbol{u}}^h\,\mathrm{d}\Gamma - \int_{\Gamma_x^{g^2}} \tilde{\Psi}_I \boldsymbol{\eta}^T \boldsymbol{\sigma}^2(\tilde{\boldsymbol{\varepsilon}}^h)\,\mathrm{d}\Gamma + \beta^2 \int_{\Gamma_x^{g^2}} \tilde{\Psi}_I \tilde{\boldsymbol{u}}^h\,\mathrm{d}\Gamma \tag{7.17b}$$

Note that in general the inclusion may lie on the essential boundary $\Gamma_x^{g,2}$. In this case, it receives a similar treatment to the background for the purpose of imposing essential boundary conditions on the inclusion material.

Using (7.5a) to (7.12) defined earlier during linearization, the tangent stiffness matrix considering material nonlinearities only is given as follows. The equations are virtually identical

to those given in (4.25a) with the exception that $\boldsymbol{D}^m$ is used instead of linear elasticity.

$$\boldsymbol{K}_{IJ} = \int_{\Omega_x} \boldsymbol{B}_I^T \boldsymbol{D}^1 \boldsymbol{B}_J \,\mathrm{d}\Omega - \int_{\Omega_x^2} \hat{\boldsymbol{B}}_I^T \boldsymbol{D}^1 \hat{\boldsymbol{B}}_J \,\mathrm{d}\Omega + \alpha^1 \int_{\Gamma_x^I} \boldsymbol{B}_I^T \boldsymbol{D}^1 \boldsymbol{\eta} \Psi_J \,\mathrm{d}\Gamma \tag{7.18a}$$
$$+\alpha^1 \int_{\Gamma_0^I} \Psi_I \boldsymbol{\eta}^T \boldsymbol{D}^1 \boldsymbol{B}_J \,\mathrm{d}\Gamma + \gamma \boldsymbol{I} \int_{\Gamma_0^I} \Psi_I \Psi_J \,\mathrm{d}\Gamma + \boldsymbol{K}_{IJ}^{EB}$$

$$\boldsymbol{K}_{IJ}^{EB} = -\int_{\Gamma_0^g} \boldsymbol{B}_I^T \boldsymbol{D}^1 \boldsymbol{\eta} \Psi_J \,\mathrm{d}\Gamma - \int_{\Gamma_0^g} \Psi_I \boldsymbol{\eta}^T \boldsymbol{D}^1 \boldsymbol{B}_J \,\mathrm{d}\Gamma + \beta^1 \boldsymbol{I} \int_{\Gamma_0^g} \Psi_I \Psi_J \,\mathrm{d}\Gamma \tag{7.18b}$$

$$\boldsymbol{G}_{IJ} = -\alpha^1 \int_{\Gamma_0^I} \boldsymbol{B}_I^T \boldsymbol{D}^1 \boldsymbol{\eta} \tilde{\Psi}_J \,\mathrm{d}\Gamma + \alpha^2 \int_{\Gamma_0^I} \Psi_I \boldsymbol{\eta}^T \boldsymbol{D}^2 \tilde{\boldsymbol{B}}_J \,\mathrm{d}\Gamma - \gamma \boldsymbol{I} \int_{\Gamma_0^I} \Psi_I \tilde{\Psi}_J \,\mathrm{d}\Gamma \tag{7.18c}$$

$$\tilde{\boldsymbol{K}}_{IJ} = \int_{\Omega_0^2} \tilde{\boldsymbol{B}}_I^T \boldsymbol{D}^2 \tilde{\boldsymbol{B}}_J \,\mathrm{d}\Omega - \alpha^2 \int_{\Gamma_0^I} \tilde{\boldsymbol{B}}_I^T \boldsymbol{D}^2 \boldsymbol{\eta} \tilde{\Psi}_J \,\mathrm{d}\Gamma \tag{7.18d}$$
$$-\alpha^2 \int_{\Gamma_0^I} \tilde{\Psi}_I \boldsymbol{\eta}^T \boldsymbol{D}^2 \tilde{\boldsymbol{B}}_J \,\mathrm{d}\Gamma + \gamma \boldsymbol{I} \int_{\Gamma_0^I} \tilde{\Psi}_I \tilde{\Psi}_J \,\mathrm{d}\Gamma + \tilde{\boldsymbol{K}}_{IJ}^{EB}$$

$$\tilde{\boldsymbol{K}}_{IJ}^{EB} = -\int_{\Gamma_0^g} \tilde{\boldsymbol{B}}_I^T \boldsymbol{D}^2 \boldsymbol{\eta} \tilde{\Psi}_J \,\mathrm{d}\Gamma - \int_{\Gamma_0^g} \tilde{\Psi}_I \boldsymbol{\eta}^T \boldsymbol{D}^2 \tilde{\boldsymbol{B}}_J \,\mathrm{d}\Gamma + \beta^2 \boldsymbol{I} \int_{\Gamma_0^g} \tilde{\Psi}_I \tilde{\Psi}_J \,\mathrm{d}\Gamma \tag{7.18e}$$

7.1.3 External Force:

The external forces are given by:

$$\begin{bmatrix} \boldsymbol{f}^{ext} \\ \tilde{\boldsymbol{f}}^{ext} \end{bmatrix} = \begin{bmatrix} \boldsymbol{f}^{ext,b} \\ \tilde{\boldsymbol{f}}^{ext,b} \end{bmatrix} + \begin{bmatrix} \boldsymbol{f}^{ext,EB} \\ \tilde{\boldsymbol{f}}^{ext,EB} \end{bmatrix} \tag{7.19}$$

where $\boldsymbol{f}^{ext,b}$ and $\tilde{\boldsymbol{f}}^{ext,b}$ are contributions from external loading, and $\boldsymbol{f}^{ext,EB}$ and $\tilde{\boldsymbol{f}}^{ext,EB}$ are contributions from imposing essential boundary conditions. Because the interface conditions act as internal constraints between the background and foreground approximations, they do not appear as external forcing terms.

In the same manner as for the internal force terms, the approximations given by (4.15)

and (4.18) are introduced into δW^{ext} in (7.1d). The external forces are:

$$\boldsymbol{f}_I^{ext,b} = \int_{\Omega_x} \Psi_I \boldsymbol{b}_0^1 \, \mathrm{d}\Omega - \int_{\Omega_x^2} \hat{\Psi}_I \boldsymbol{b}_0^1 \, \mathrm{d}\Omega + \int_{\Gamma_x^h} \Psi_I \boldsymbol{h} \, \mathrm{d}\Gamma \tag{7.20a}$$

$$\tilde{\boldsymbol{f}}_I^{ext,b} = \int_{\Omega_x^2} \tilde{\Psi}_I \boldsymbol{b}_0^2 \, \mathrm{d}\Omega \tag{7.20b}$$

Likewise, (4.15) and (4.18) are introduced as test functions for the essential boundary terms involving $\boldsymbol{g}$. The resulting external forces due to essential boundary imposition are:

$$\boldsymbol{f}_I^{ext,EB} = -\int_{\Gamma_x^g} \boldsymbol{B}_I^T \boldsymbol{D}^1 \boldsymbol{\eta} \boldsymbol{g} \, \mathrm{d}\Gamma + \beta^1 \int_{\Gamma_0^g} \Psi_I \boldsymbol{g} \, \mathrm{d}\Gamma \tag{7.21a}$$

$$\tilde{\boldsymbol{f}}_I^{ext,EB} = -\int_{\Gamma_x^g} \tilde{\boldsymbol{B}}_I^T \boldsymbol{D}^2 \boldsymbol{\eta} \boldsymbol{g} \, \mathrm{d}\Gamma + \beta^2 \int_{\Gamma_0^g} \tilde{\Psi}_I \boldsymbol{g} \, \mathrm{d}\Gamma \tag{7.21b}$$

Once the weak form in (7.1) has been linearized, the solution for a given load step is determined by forcing the residual to be less than certain residual measures selected by the user.

$$\begin{bmatrix} \boldsymbol{K} & \boldsymbol{G} \\ \boldsymbol{G}^T & \tilde{\boldsymbol{K}} \end{bmatrix}_{n+1}^{\nu} \begin{bmatrix} \Delta \boldsymbol{u} \\ \Delta \tilde{\boldsymbol{u}} \end{bmatrix}_{n+1}^{\nu} = \begin{bmatrix} \boldsymbol{f}^{ext} \\ \tilde{\boldsymbol{f}}^{ext} \end{bmatrix}_{n+1} - \begin{bmatrix} \boldsymbol{f}^{int}(\boldsymbol{u}^h, \tilde{\boldsymbol{u}}^h) \\ \tilde{\boldsymbol{f}}^{int}(\boldsymbol{u}^h, \tilde{\boldsymbol{u}}^h) \end{bmatrix}_{n+1}^{\nu} \tag{7.22}$$

$$\begin{bmatrix} \boldsymbol{u} \\ \tilde{\boldsymbol{u}} \end{bmatrix}_{n+1}^{\nu+1} = \begin{bmatrix} \boldsymbol{u} \\ \tilde{\boldsymbol{u}} \end{bmatrix}_{n+1}^{\nu} + \begin{bmatrix} \Delta \boldsymbol{u} \\ \Delta \tilde{\boldsymbol{u}} \end{bmatrix}_{n+1}^{\nu} \tag{7.23}$$

where ν is the iteration index for a given load step $n+1$.

7.2 Pullout from Brittle Material

To demonstrate the proposed method, a rebar pullout model is performed in two dimensions. For brittle materials, an elastic-damage law as used in [19] is utilized and is given below.

$$\boldsymbol{\sigma} = (1-d)\boldsymbol{C} : \boldsymbol{\varepsilon} \tag{7.24a}$$

$$d(\bar{\varepsilon}) = \begin{cases} \dfrac{\bar{\varepsilon}_c(\bar{\varepsilon}-\bar{\varepsilon}_i)}{\bar{\varepsilon}(\bar{\varepsilon}_c-\bar{\varepsilon}_i)} & \bar{\varepsilon}_i \leq \bar{\varepsilon} \leq \bar{\varepsilon}_c \\ 1 & \bar{\varepsilon}_c < \bar{\varepsilon} \end{cases} \tag{7.24b}$$

and where $\bar{\varepsilon}$ is an equivalent strain which governs the damage parameter d. Here, the equivalent strain is defined using the deviatoric part of the strain as follows.

$$\boldsymbol{\varepsilon}^d = \boldsymbol{\varepsilon} - \frac{1}{3}\mathbf{I}\mathrm{tr}(\boldsymbol{\varepsilon}) \tag{7.25a}$$

$$\bar{\varepsilon} = \sqrt{\frac{2}{3}\boldsymbol{\varepsilon}^d : \boldsymbol{\varepsilon}^d} \tag{7.25b}$$

A 25 mm "deformed" bar with a length of 100 mm is embedded into a background matrix measuring 150 mm $\times$ 150 mm. The term "deformed" refers to the fact that the reinforcement includes ribs on the wall of the bar which generates mechanical interlock between the reinforcement and the background material. The top surface of the background is given a fixed displacement condition except at its center, where the bar is pulled through. The rebar is pulled by a prescribed displacement of $g_y = 1.0$ mm at the top of the rebar, as shown in Figure 7.1. The left, right, and bottom surfaces of the outer medium are free surfaces with no tractions or prescribed boundary conditions. In this study, the background matrix is given material properties of $E^1 = 20.0$ GPa, $\nu^1 = 0.2$, $\bar{\varepsilon}_i = 0.0014$, and $\bar{\varepsilon}_c = 0.030$. The foreground employs an elastic material without damage with $E^2 = 200$ GPa and $\nu^2 = 0.3$. The problem is modeled in 2D with the plane strain assumption. While this is not a realistic assumption, the purpose of this example is to demonstrate the effectiveness of capturing weak discontinuities under a nonlinear setting.

The discretization is given in Figure 7.2. The background is modeled by a uniform discretization and is independent from the foreground discretization. This example demonstrates

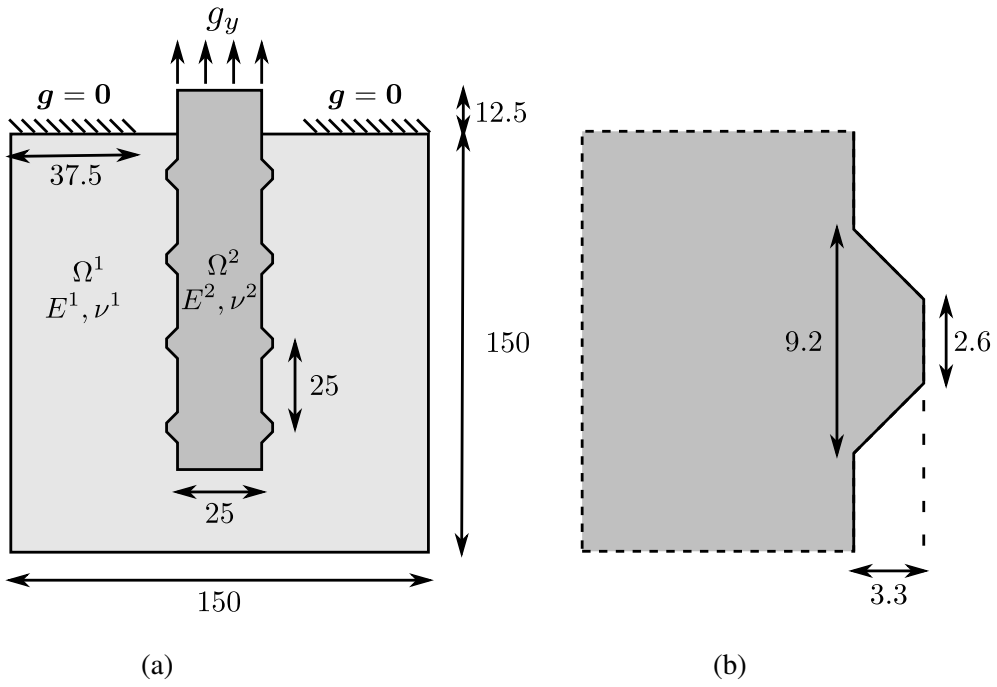

Figure 7.1: Pullout problem setup, all units are in mm. (a) Problem geometry; (b) Rib geometry

the ease for discretizing a model using the immersed RKPM method because the approximations are independent from each other. Although the problem is only in two dimensions and a conformal mesh may be generated, it still requires more effort by the user to generate such a discretization to do so and becomes more complicated with more reinforcement, especially in three dimensions. The immersed RKPM method is used and the RK approximation is constructed with linear basis, cubic B-spline kernels with support $a = 2.0h$. For enforcing the essential boundaries, $\beta^1 = 100E^1/h$ and $\beta^2 = 100E^2/h$. The Nitsche stabilization term at the interface is $\gamma = 2E^1/h$. Two analyses are performed: a linear analysis compared to body-fitted FEM using ABAQUS [77]; and a nonlinear analysis using the damage law in (7.24) to compare with body-fitted RKPM.

7.2.1 Linear comparison with body-fitted FEM

The immersed RKPM method is first compared to a linear finite element model with conformal discretization as shown in Figure 7.3. This study is intended to verify the implemen-

tation accuracy of the immersed RKPM method. For this study, the surface of the bar is also given a prescribed displacement of $g_y = 1.0$ mm. The results for the displacement and strains are given below in Figure 7.4 and Figure 7.5. The y-displacement of the immersed RKPM method is slightly greater than the body-fitted FEM results but overall the displacement profiles agree with each other. The strain results show good agreement between the immersed RKPM and conformal FEM solutions, particularly in matching the tensile strain ε_{yy} experienced behind each rib of the rebar.

The reaction force between immersed RKPM and the body-fitted FEM shown in Figure 7.6 also shows close agreement well. A slightly softer response is obtained using immersed RKPM, differing by 1.7% between immersed RKPM and body-fitted FEM at a displacement of 1 mm.

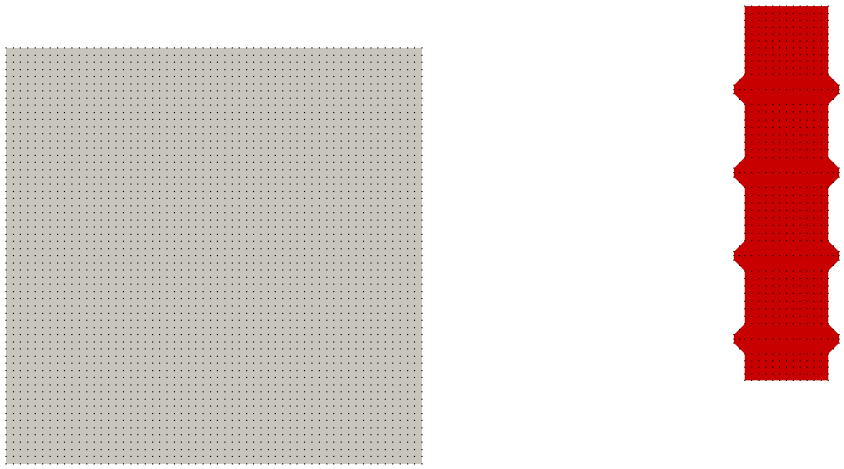

(a) (b)

Figure 7.2: Rebar pullout discretization. (a) Background discretization; (b) foreground discretization

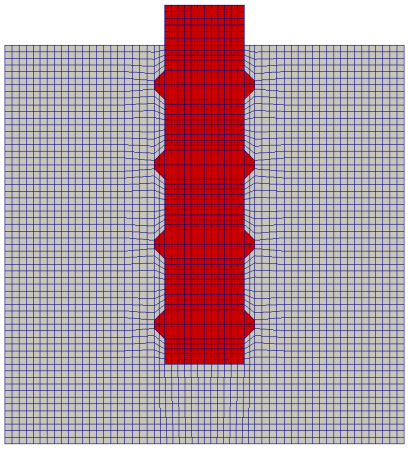

Figure 7.3: Conformal mesh for rebar pullout discretization

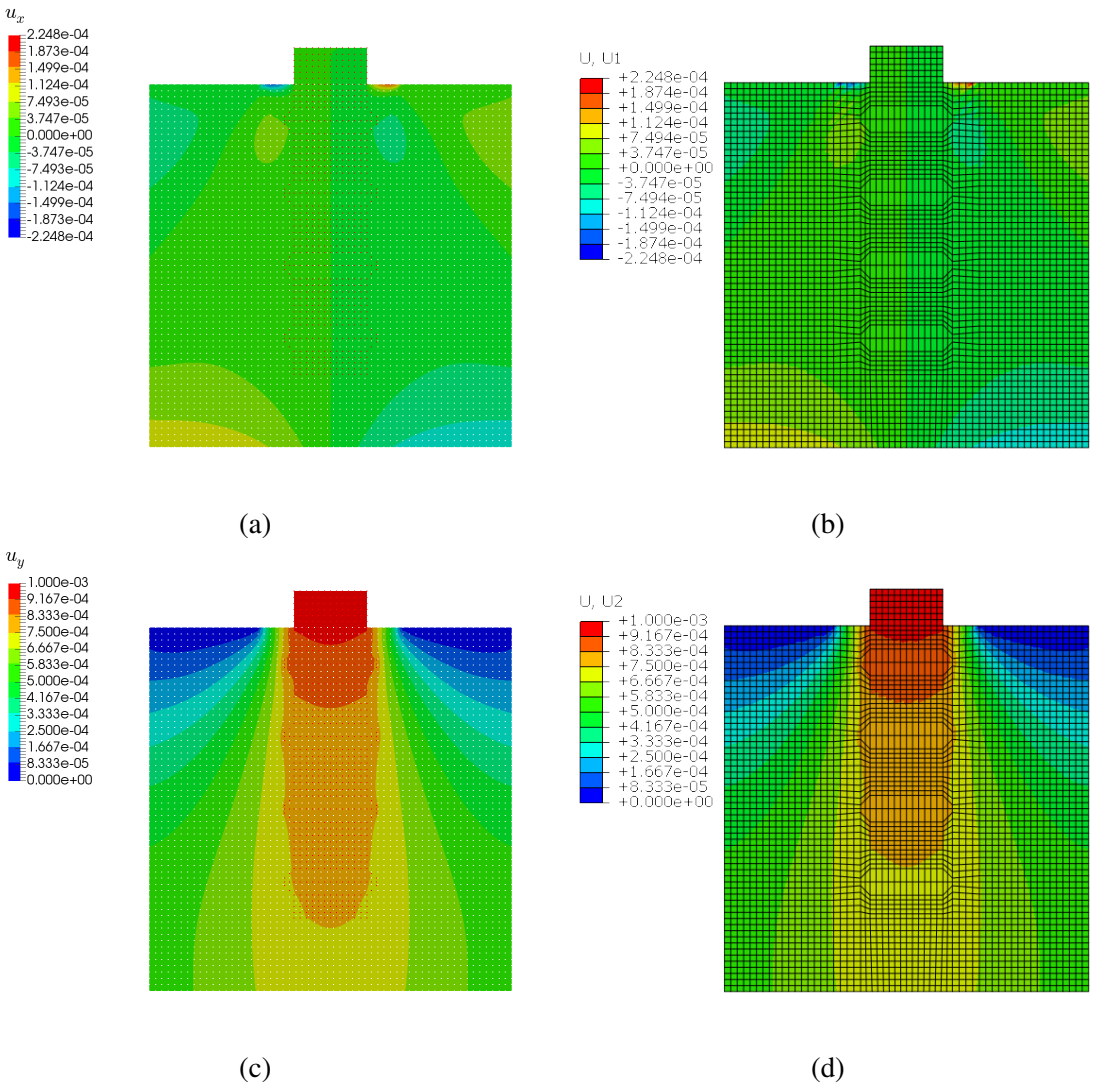

Figure 7.4: Displacement comparison between immersed RKPM and body-fitted FEM $g_y = 1.0$ mm. (a) Immersed RKPM u_x; (b) Body-fitted FEM u_x; (c) Immersed RKPM u_y; (d) Body-fitted FEM u_y

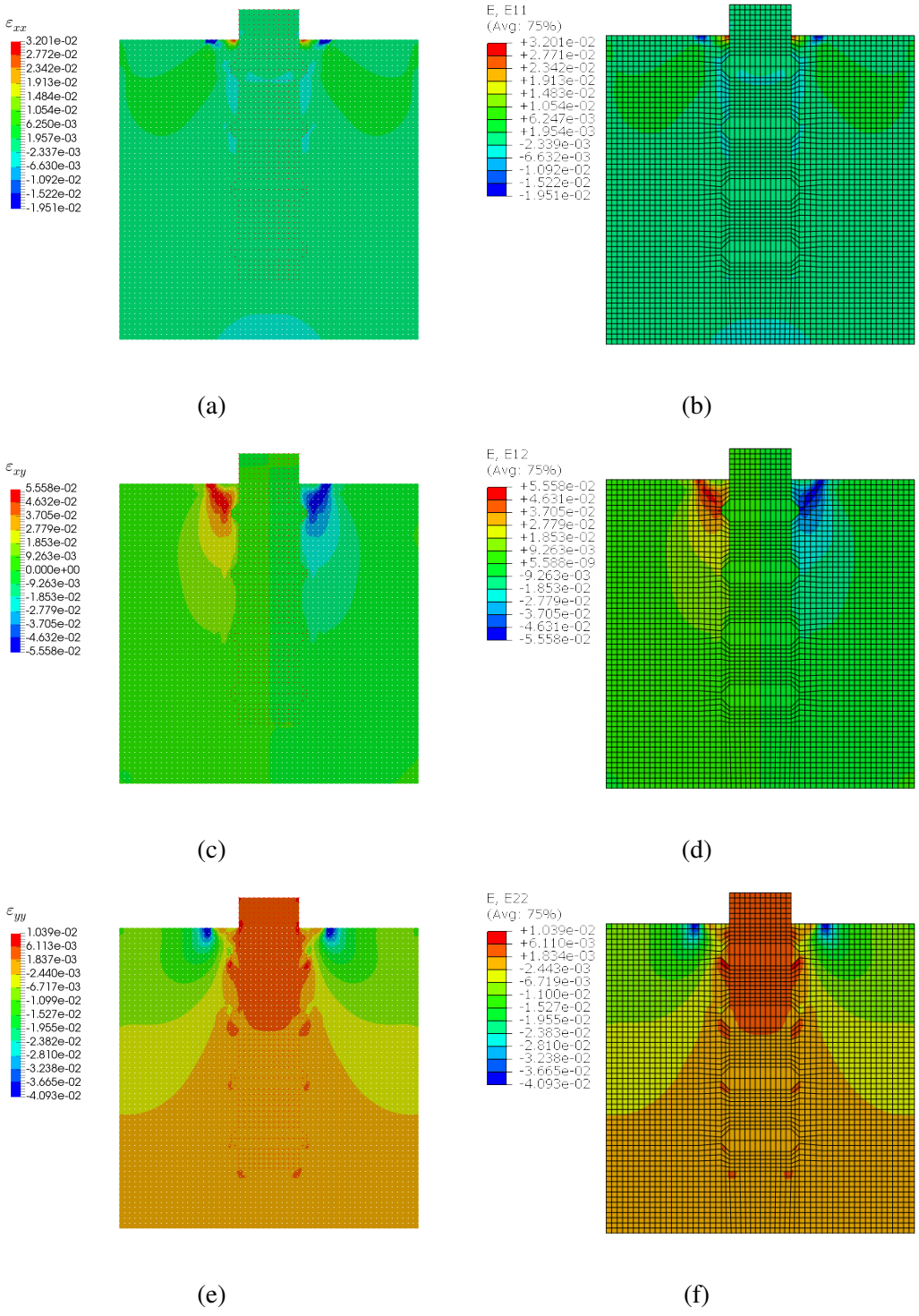

Figure 7.5: Strain comparison between immersed RKPM and body-fitted FEM $g_y = 1.0$ mm. (a) Immersed RKPM ε_{xx}; (b) Body-fitted FEM ε_{xx}; (c) Immersed RKPM ε_{xy}; (d) Body-fitted FEM ε_{xy}; (e) Immersed RKPM ε_{yy}; (f) Body-fitted FEM ε_{yy}

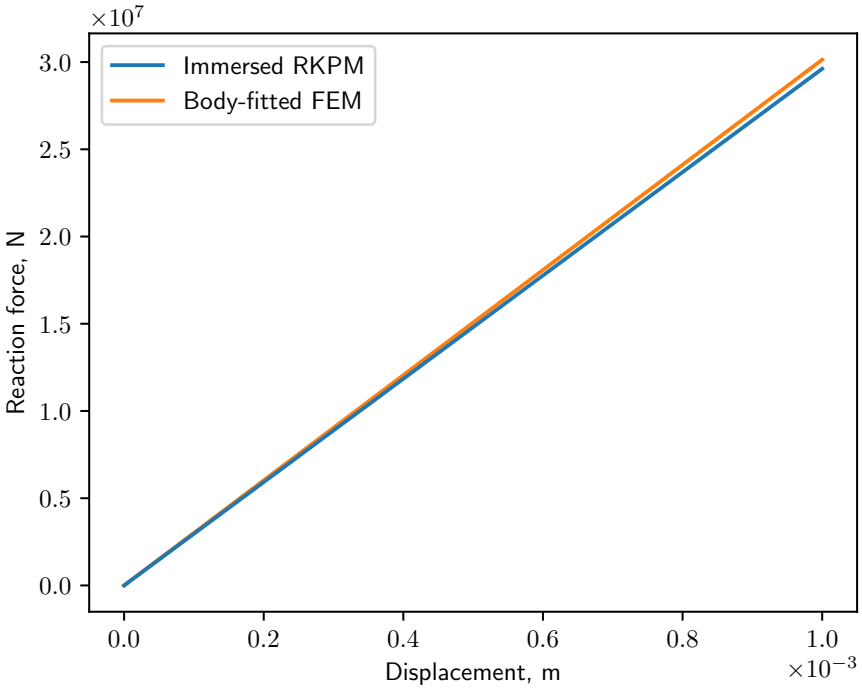

Figure 7.6: Reaction force of pullout problem with linear elasticity

7.2.2 Nonlinear comparison with body-fitted RKPM

The problem is then run with the elastic-damage law using immersed RKPM. The results for four load steps are given below in Figure 7.7 and Figure 7.8 for the damage and equivalent strain, respectively. The damage is initially concentrated at the top of the matrix domain near the fixed boundaries. Once the bar has become fully pulled, the damage spreads throughout the remainder of the domain in the shape of a cone. The equivalent strain is also concentrated at the top of the domain where large shear strains are present, but progressively spreads throughout the rest of the background as the displacement increases.

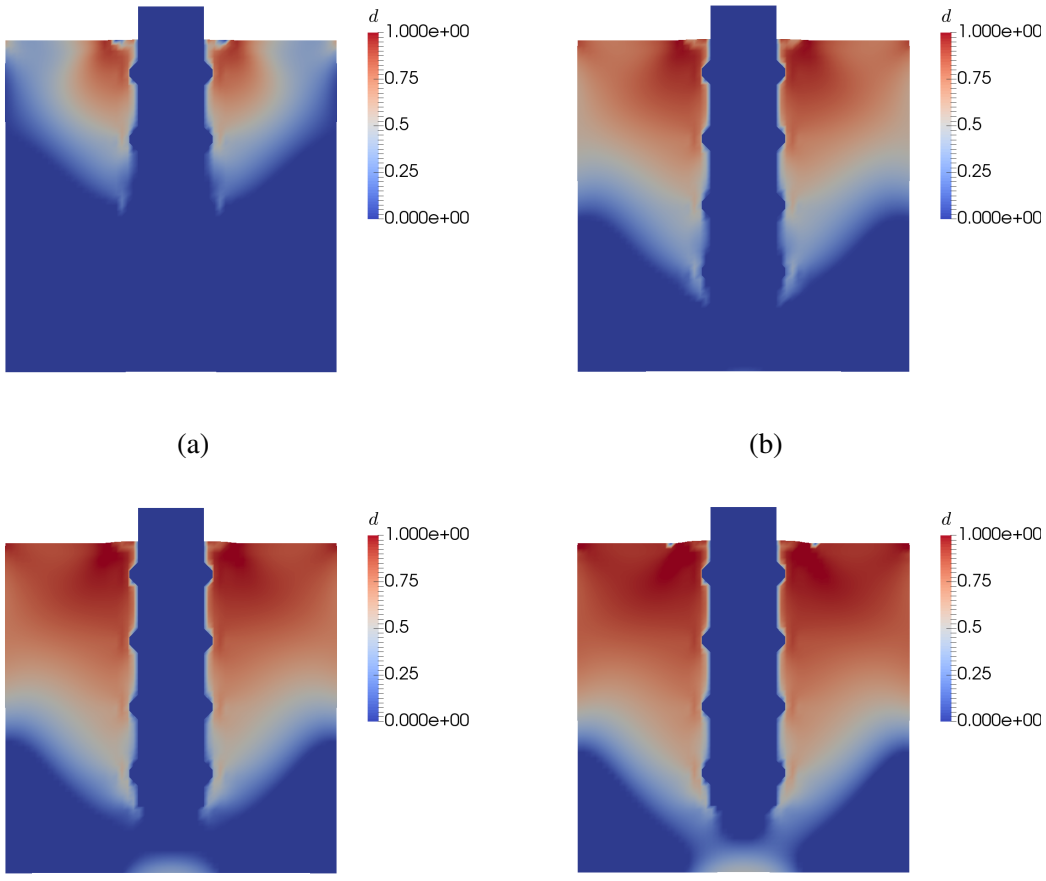

Figure 7.7: Damage profiles of pullout simulation using immersed RKPM. (a) $g_y = 0.25$mm; (b) $g_y = 0.50$mm; (c) $g_y = 0.75$mm; (d) $g_y = 1.0$mm

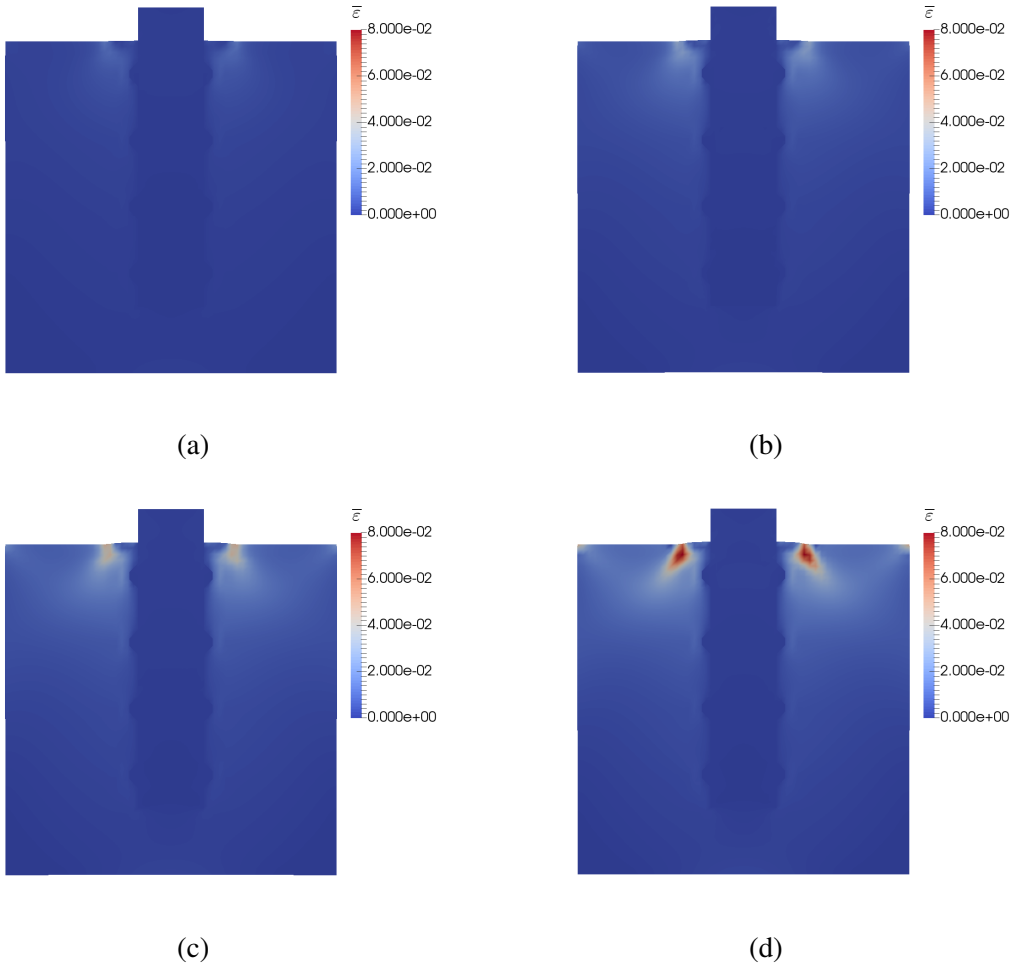

Figure 7.8: Equivalent strain of pullout simulation using immersed RKPM. (a) $g_y = 0.25$mm; (b) $g_y = 0.50$mm; (c) $g_y = 0.75$mm; (d) $g_y = 1.0$mm

For comparison, a study is also made using a conformal, body-fitted discretization with a similar nodal spacing, as shown in Figure 7.3. The standard RKPM method is used by using nodes in this body-fitted conformal discretization. The damage profiles of immersed and body-fitted RKPM are given in Figure 7.9 when the bar has reached a displacement of $g_y = 1.0$ mm. Both methods show generally good agreement to the damage in the surrounding material, but the immersed method has a sharp transition in damage between the background and foreground whereas the conforming RKPM analysis is more diffuse across the material interface. This is due to the smooth approximation in the body-fitted RKPM which is incapable of capturing interface

strain discontinuity and "smooths" out the strain, leading to less localized damage. This is clearly demonstrated in Figure 7.10, which compares the shear strain and equivalent strain across the second rib from the top at position $y = 25.4$ mm. Both strains exhibit a weak discontinuity for the immersed RKPM method whereas the conforming RKPM results are smeared over the interface.

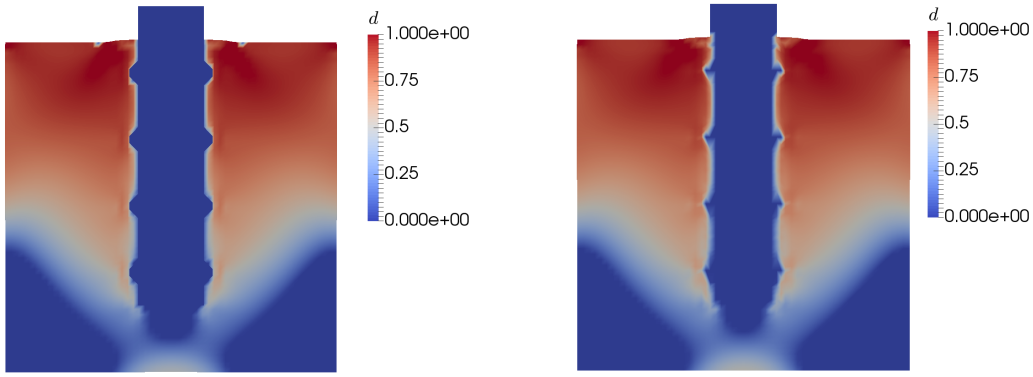

(a) (b)

Figure 7.9: Comparison of damage profiles of immersed RKPM and body-fitted RKPM at $g_y = 1.0$ mm. (a) Immersed RKPM; and (b) Body-fitted RKPM.

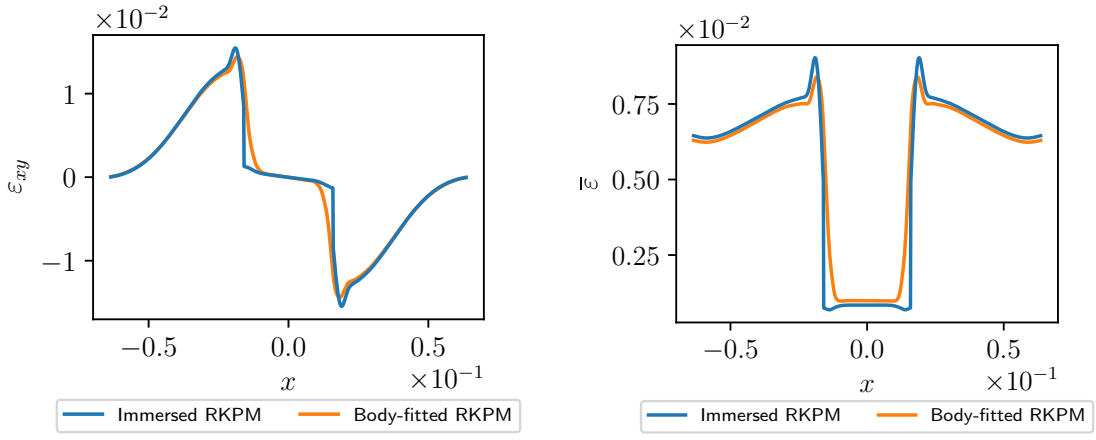

(a) (b)

Figure 7.10: Strain comparisons between immersed RKPM and body-fitted RKPM along line at $y = 25.4$ mm, $g_y = 1.0$ mm. (a) Shear strain ε_{xy}; (b) Equivalent strain $\bar{\varepsilon}$

The strain distributions of the standard and immersed RKPM methods are compared in

Figure 7.11. The strains are very similar to each other, but on closer inspection of the ribs, the immersed RKPM method has clear strain localization near the material interface indicating the weak discontinuity is properly captured whereas the standard RKPM with body-fitted conformal discretization is more diffuse and spread out. This is again due to the inability to capture a derivative jump using a continuous RK approximation.

The reaction forces at the fixed boundary are also given in Figure 7.12 and shows the immersed RKPM approach gives results consistent with the body-fitted, standard RKPM method in predicting the global response of this pullout test.

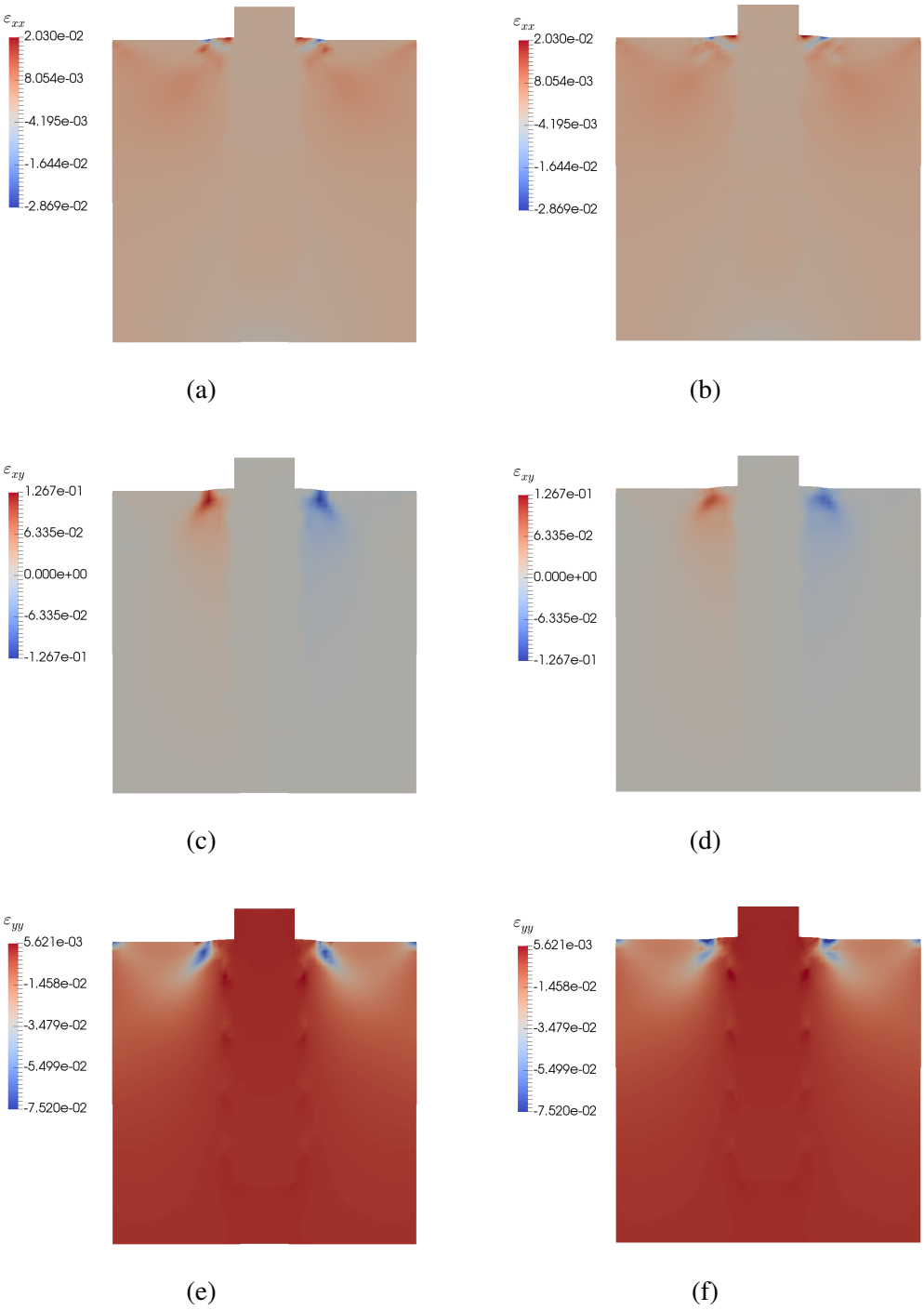

Figure 7.11: Strain comparison between immersed RKPM and body-fitted RKPM $g_y = 2.54$ mm. (a) Immersed RKPM ε_{xx}; (b) Body-fitted RKPM ε_{xx}; (c) Immersed RKPM ε_{xy}; (d) Body-fitted RKPM ε_{xy}; (e) Immersed RKPM ε_{yy}; (f) Body-fitted RKPM ε_{yy}

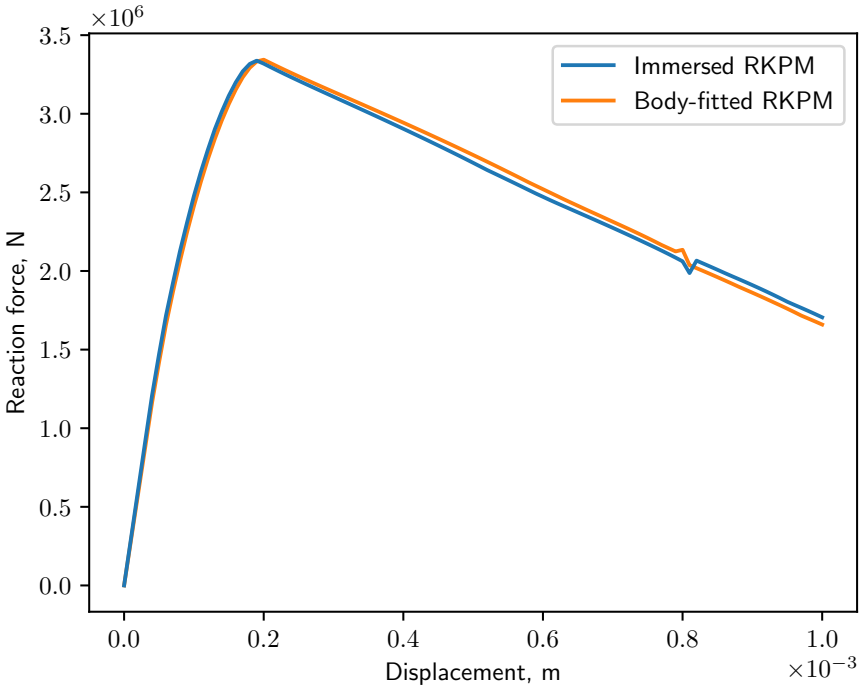

Figure 7.12: Reaction force of pullout problem with elastic-damage law

Acknowledgements

Chapter 7 includes unpublished material which is coauthored with J.S. Chen, H. Wei, and J. Sherburn. The dissertation author was the primary author of this chapter.

Chapter 8

Conclusions

In this dissertation, an immersed RKPM approach was proposed for problems with inhomogeneous materials. Nitsche's method is used to consistently enforce the displacement continuity and traction equilibrium at the material discontinuity. By introducing fictitious material to the background, the discretization of the total domain and foreground domains are simplified. Furthermore, they may be generated independently of each other and are not required to conform at the material interface. The immersed RKPM approach is developed for linear and nonlinear problems and strategies for integration of the background and foreground domains are discussed.

The immersed RKPM approach is shown to be effective in solving multi-material problems provided that the quadrature is sufficiently accurate and stable. The verification results from Chapter 6 show a strong dependence on integration order. 1-pt Gauss quadrature and SCNI demonstrate unstable behavior due to spurious low-energy modes present in the system. This can trigger unphysical behavior in the fictitious domain and leads to oscillations near the material interface. 5-pt Gauss quadrature is shown to be sufficient for the immersed RKPM method but requires many evaluation points, which is expensive for RKPM and is particularly severe when considering problems in three dimensions. To mitigate the computational expense, M-SCNI is adapted for use with immersed RKPM and is shown to be as accurate as high-order Gauss

integration but at a much lower cost. The integration constraints developed in [20] are also applicable to the immersed RKPM method. Optimal convergence of the immersed RKPM method is demonstrated using both 5-pt Gauss integration and M-SCNI.

Several numerical examples are given and show the accuracy of the proposed method. A comparison of immersed RKPM with FEM solution is given, and the immersed RKPM method is shown to effectively model bi-material problems without tedious discretization of the interface. The jump condition of the inhomogeneous material interfaces is captured as a result of using two different approximation functions, which naturally yields discontinuous derivatives at the interface. In this approach, no explicit enrichment of the approximation functions is required as in previous works [78, 50, 80]. This greatly simplifies the modeling procedure using the immersed approach. The immersed RKPM formulation was also extended to nonlinear problems and is demonstrated using an elastic-damage model. The immersed approach is not limited to the use of RKPM approximations and could be utilized to couple with FEM.

8.1 Recommendations for future research

Directions for future research for the immersed RKPM method are recommended as follows:

- Development of the immersed RKPM method to include transient analysis and dynamics. The critical time step of the immersed approach may be investigated with considerations to Nitsche's method at the material interface. An immersed method including dynamics is of particular interest to problems involving complex material geometries where high strain rates and large deformation are expected.

- Development of a semi-Lagrangian, immersed RKPM method to incorporate moving interfaces and formation of free surfaces. Under high strain rates, significant deformation can occur which will cause the analysis to fail should the deformation gradient become

non-invertible. Such conditions could occur during, for example, extensive fragmentation of quasi-brittle materials. The use of the semi-Lagrangian formulation under the immersed RKPM framework would enable the detection of free surfaces and avoid difficulties associated with a total Lagrangian framework.

- Generalize the interface conditions to consider a non-zero jump in the displacement field at the material interface (i.e. an imperfectly bonded interface). Such a non-zero jump may be introduced using a cohesive traction law dependent on the relative displacement at the material interface. By including an interface compliance, physical phenomena such as interfacial transition zones may be captured, which are not adequately described under the perfectly bonded assumption.

- The immersed approach is not limited to the use of RKPM and may be used to couple with other approximations such as FEM to take advantages of both. RKPM may be used where smooth solution fields are expected and FEM can be used in the inclusion domain where little deformation occurs. This may promote solution efficiency when using less expensive approximations than RK or others based off of moving least squares. The focus of this work is immersed RKPM under a Lagrangian formulation, but the immersed methodology provides a framework for semi-Lagrangian or Lagrangian/semi-Lagrangian coupling.

- Parallel considerations when using the immersed RKPM method. Because of its block matrix format, the immersed RKPM approach lends itself to solution methods such as taking the Schur complement. This can greatly simplify the solution procedure provided the bulk stiffness contributions may be statically condensed by relating them to the background degrees of freedom. In addition, when multiple inclusions are present, the solution of each may be divided among several processors in parallel.

- Comparison of the immersed RKPM method to a suite of experiments to validate correct prediction of the interface conditions. The experiments should be designed to measure the

interface quantities as closely as possible in order to test the immersed RKPM approach. Instrumentation methods could employ X-ray tomography in order to make direct observations to the material interface. The experiments may range from simple configurations, such pullout of a single reinforcing bar from a concrete base, to more complex configurations with multiple reinforcing inclusions.

- Coupling the immersed RKPM method with shocks either in a fluid or solid background. The proposed framework can be applied to model wave reflections/transmissions at material interface in the presence of a shock wave. The proposed method may also be used to embed a moving, Lagrangian solid within an Eulerian background.

Bibliography

[1] M. Aftosmis, M. Berger, and G. Adomavicius. A parallel multilevel method for adaptively refined cartesian grids with embedded boundaries. In *38th Aerospace Sciences Meeting and Exhibit*. American Institute of Aeronautics and Astronautics, 2000.

[2] P. Angot, C.-H. Bruneau, and P. Fabrie. A penalization method to take into account obstacles in incompressible viscous flows. *Numerische Mathematik*, 81(4):497–520, 1999.

[3] C. Annavarapu, M. Hautefeuille, and J. E. Dolbow. A robust nitsche's formulation for interface problems. *Computer Methods in Applied Mechanics and Engineering*, 225-228:44 – 54, 2012.

[4] C. Annavarapu, M. Hautefeuille, and J. E. Dolbow. A nitsche stabilized finite element method for frictional sliding on embedded interfaces. part i: Single interface. *Computer Methods in Applied Mechanics and Engineering*, 268:417 – 436, 2014.

[5] F. P. T. Baaijens. A fictitious domain/mortar element method for fluid–structure interaction. *International Journal for Numerical Methods in Fluids*, 35(7):743–761, 2001.

[6] Y. Bazilevs, K. Kamran, G. Moutsanidis, D. J. Benson, and E. Oñate. A new formulation for air-blast fluid–structure interaction using an immersed approach. part i: basic methodology and fem-based simulations. *Computational Mechanics*, 60(1):83–100, 2017.

[7] F. B. Belgacem. The mortar finite element method with lagrange multipliers. *Numerische Mathematik*, 84(2):173–197, 1999.

[8] T. Belytschko, N. Moës, S. Usui, and C. Parimi. Arbitrary discontinuities in finite elements. *International Journal for Numerical Methods in Engineering*, 50(4):993–1013, 2001.

[9] R. P. Beyer. A computational model of the cochlea using the immersed boundary method. *Journal of Computational Physics*, 98(1):145 – 162, 1992.

[10] E. Burman and P. Hansbo. Fictitious domain finite element methods using cut elements: I. a stabilized lagrange multiplier method. *Computer Methods in Applied Mechanics and Engineering*, 199(41):2680 – 2686, 2010.

[11] E. Burman and P. Hansbo. Fictitious domain finite element methods using cut elements: II. a stabilized nitsche method. *Applied Numerical Mathematics*, 62(4):328 – 341, 2012. Third Chilean Workshop on Numerical Analysis of Partial Differential Equations (WONAPDE 2010).

[12] J.-S. Chen, M. Hillman, and S.-W. Chi. Meshfree methods: Progress made after 20 years. *Journal of Engineering Mechanics*, 143(4):04017001, 2017.

[13] J.-S. Chen, M. Hillman, and M. Rüter. An arbitrary order variationally consistent integration for galerkin meshfree methods. *International Journal for Numerical Methods in Engineering*, 95(5):387–418, 2013.

[14] J.-S. Chen, W. Hu, M. Puso, Y. Wu, and X. Zhang. *Strain Smoothing for Stabilization and Regularization of Galerkin Meshfree Methods*, pages 57–75. Springer Berlin Heidelberg, Berlin, Heidelberg, 2007.

[15] J.-S. Chen, C. Pan, C.-T. Wu, and W. K. Liu. Reproducing kernel particle methods for large deformation analysis of non-linear structures. *Computer Methods in Applied Mechanics and Engineering*, 139(1):195 – 227, 1996.

[16] J.-S. Chen and D. Wang. A constrained reproducing kernel particle formulation for shear deformable shell in cartesian coordinates. *International Journal for Numerical Methods in Engineering*, 68(2):151–172, 2006.

[17] J.-S. Chen and H.-P. Wang. New boundary condition treatments in meshfree computation of contact problems. *Computer Methods in Applied Mechanics and Engineering*, 187(3):441 – 468, 2000.

[18] J. S. Chen, H. P. Wang, S. Yoon, and Y. You. Some recent improvements in meshfree methods for incompressible finite elasticity boundary value problems with contact. *Computational Mechanics*, 25(2):137–156, Mar 2000.

[19] J.-S. Chen, C.-T. Wu, and T. Belytschko. Regularization of material instabilities by meshfree approximations with intrinsic length scales. *International Journal for Numerical Methods in Engineering*, 47(7):1303–1322, 2000.

[20] J.-S. Chen, C.-T. Wu, S. Yoon, and Y. You. A stabilized conforming nodal integration for galerkin mesh-free methods. *International Journal for Numerical Methods in Engineering*, 50(2):435–466, 2001.

[21] J.-S. Chen and Y. Wu. *Stability in Lagrangian and Semi-Lagrangian Reproducing Kernel Discretizations Using Nodal Integration in Nonlinear Solid Mechanics*, pages 55–76. Springer Netherlands, Dordrecht, 2007.

[22] D. K. Clarke, H. A. Hassan, and M. D. Salas. Euler calculations for multielement airfoils using cartesian grids. *AIAA Journal*, 24(3):353–358, 1986.

[23] L. Cordes and B. Moran. Treatment of material discontinuity in the element-free galerkin method. *Computer Methods in Applied Mechanics and Engineering*, 139(1–4):75 – 89, 1996.

[24] A. Dadone and B. Grossman. An immersed boundary methodology for inviscid flows on cartesian grids. In *40th Aerospace Sciences Meeting & Exhibit*, number AIAA 2002-1059, 2002.

[25] D. DeZeeuw and K. G. Powell. An adaptively refined cartesian mesh solver for the euler equations. *Journal of Computational Physics*, 104(1):56 – 68, 1993.

[26] J. Dolbow and T. Belytschko. Numerical integration of the galerkin weak form in meshfree methods. *Computational Mechanics*, 23(3):219–230, Apr 1999.

[27] J. Dolbow and I. Harari. An efficient finite element method for embedded interface problems. *International Journal for Numerical Methods in Engineering*, 78(2):229–252, 2009.

[28] C. Duarte, O. Hamzeh, T. Liszka, and W. Tworzydlo. A generalized finite element method for the simulation of three-dimensional dynamic crack propagation. *Computer Methods in Applied Mechanics and Engineering*, 190(15):2227 – 2262, 2001.

[29] A. Düster, J. Parvizian, Z. Yang, and E. Rank. The finite cell method for three-dimensional problems of solid mechanics. *Computer Methods in Applied Mechanics and Engineering*, 197(45):3768 – 3782, 2008.

[30] J. D. Eshelby. The determination of the elastic field of an ellipsoidal inclusion, and related problems. *Proceedings of the Royal Society of London A: Mathematical, Physical and Engineering Sciences*, 241(1226):376–396, 1957.

[31] E. Fadlun, R. Verzicco, P. Orlandi, and J. Mohd-Yusof. Combined immersed-boundary finite-difference methods for three-dimensional complex flow simulations. *Journal of Computational Physics*, 161(1):35 – 60, 2000.

[32] S. Fernández-Méndez and A. Huerta. Imposing essential boundary conditions in mesh-free methods. *Computer Methods in Applied Mechanics and Engineering*, 193(12):1257 – 1275, 2004. Meshfree Methods: Recent Advances and New Applications.

[33] R. Glowinski, T. Pan, T. Hesla, D. Joseph, and J. Périaux. A fictitious domain approach to the direct numerical simulation of incompressible viscous flow past moving rigid bodies: Application to particulate flow. *Journal of Computational Physics*, 169(2):363 – 426, 2001.

[34] R. Glowinski, T.-W. Pan, T. Hesla, and D. Joseph. A distributed lagrange multiplier/fictitious domain method for particulate flows. *International Journal of Multiphase Flow*, 25(5):755 – 794, 1999.

[35] R. Glowinski, T.-W. Pan, and J. Periaux. A fictitious domain method for dirichlet problem and applications. *Computer Methods in Applied Mechanics and Engineering*, 111(3):283 – 303, 1994.

[36] D. Goldstein, R. Handler, and L. Sirovich. Modeling a no-slip flow boundary with an external force field. *Journal of Computational Physics*, 105(2):354 – 366, 1993.

[37] P. Guan, J. Chen, Y. Wu, H. Teng, J. Gaidos, K. Hofstetter, and M. Alsaleh. Semi-lagrangian reproducing kernel formulation and application to modeling earth moving operations. *Mechanics of Materials*, 41(6):670 – 683, 2009. Advances in the Dynamics of Granular Materials.

[38] A. Hansbo and P. Hansbo. An unfitted finite element method, based on Nitsche's method, for elliptic interface problems. *Computer Methods in Applied Mechanics and Engineering*, 191(47):5537 – 5552, 2002.

[39] A. Hansbo and P. Hansbo. A finite element method for the simulation of strong and weak discontinuities in solid mechanics. *Computer Methods in Applied Mechanics and Engineering*, 193(33):3523 – 3540, 2004.

[40] A. Hansbo, P. Hansbo, and M. G. Larson. A finite element method on composite grids based on Nitsche's method. *ESAIM: Mathematical Modelling and Numerical Analysis*, 37(3):495–514, 2003.

[41] I. Harari and J. Dolbow. Analysis of an efficient finite element method for embedded interface problems. *Computational Mechanics*, 46(1):205–211, 2010.

[42] C. Hesch, A. Gil, A. A. Carreño, J. Bonet, and P. Betsch. A mortar approach for fluid–structure interaction problems: Immersed strategies for deformable and rigid bodies. *Computer Methods in Applied Mechanics and Engineering*, 278:853 – 882, 2014.

[43] M. Hillman and J.-S. Chen. An accelerated, convergent, and stable nodal integration in galerkin meshfree methods for linear and nonlinear mechanics. *International Journal for Numerical Methods in Engineering*, 107(7):603–630, 2016. nme.5183.

[44] M.-C. Hsu, D. Kamensky, Y. Bazilevs, M. S. Sacks, and T. J. R. Hughes. Fluid–structure interaction analysis of bioprosthetic heart valves: significance of arterial wall deformation. *Computational Mechanics*, 54(4):1055–1071, 2014.

[45] W. Jiang, C. Annavarapu, J. E. Dolbow, and I. Harari. A robust nitsche's formulation for interface problems with spline-based finite elements. *International Journal for Numerical Methods in Engineering*, 104(7):676–696, 2015. nme.4766.

[46] M. L. Kachanov, B. Shafiro, and I. Tsukrov. *Handbook of elasticity solutions*. Kluwer Academic Publishers, Dordrecht, The Netherlands, 2003.

[47] C. Kadapa, W. Dettmer, and D. Perić. A fictitious domain/distributed Lagrange multiplier based fluid–structure interaction scheme with hierarchical B-spline grids. *Computer Methods in Applied Mechanics and Engineering*, 301:1 – 27, 2016.

[48] S. L. Karman Jr. SPLITFLOW - A 3D unstructured cartesian/prismatic grid CFD code for complex geometries. In *33rd Aerospace Sciences Meeting and Exhibit*. American Institute of Aeronautics and Astronautics, 1995.

[49] J. Kim, D. Kim, and H. Choi. An immersed-boundary finite-volume method for simulations of flow in complex geometries. *Journal of Computational Physics*, 171(1):132 – 150, 2001.

[50] Y. Krongauz and T. Belytschko. EFG approximation with discontinuous derivatives. *International Journal for Numerical Methods in Engineering*, 41(7):1215–1233, 1998.

[51] M.-C. Lai and C. S. Peskin. An immersed boundary method with formal second-order accuracy and reduced numerical viscosity. *Journal of Computational Physics*, 160(2):705 – 719, 2000.

[52] A. Landsberg and J. Boris. The virtual cell embedding method - a simple approach for building complex geometries. In *13th Computational Fluid Dynamics Conference*. American Institute of Aeronautics and Astronautics, 1997.

[53] G. Legrain, N. Chevaugeon, and K. Dréau. High order x-fem and levelsets for complex microstructures: Uncoupling geometry and approximation. *Computer Methods in Applied Mechanics and Engineering*, 241-244:172 – 189, 2012.

[54] Z. Li. The immersed interface method using a finite element formulation. *Applied Numerical Mathematics*, 27(3):253 – 267, 1998.

[55] Z. Li, T. Lin, and X. Wu. New cartesian grid methods for interface problems using the finite element formulation. *Numerische Mathematik*, 96(1):61–98, 2003.

[56] W. K. Liu, W. Han, H. Lu, S. Li, and J. Cao. Reproducing kernel element method. part i: Theoretical formulation. *Computer Methods in Applied Mechanics and Engineering*, 193(12):933 – 951, 2004. Meshfree Methods: Recent Advances and New Applications.

[57] W. K. Liu, S. Jun, and Y. F. Zhang. Reproducing kernel particle methods. *International Journal for Numerical Methods in Fluids*, 20(8-9):1081–1106, 1995.

[58] W. K. Liu, Y. Liu, D. Farrell, L. Zhang, X. S. Wang, Y. Fukui, N. Patankar, Y. Zhang, C. Bajaj, J. Lee, J. Hong, X. Chen, and H. Hsu. Immersed finite element method and its applications to biological systems. *Computer Methods in Applied Mechanics and Engineering*, 195(13):1722 – 1749, 2006. A Tribute to Thomas J.R. Hughes on the Occasion of his 60th Birthday.

[59] R. Löhner, S. Appanaboyina, and J. R. Cebral. Comparison of body-fitted, embedded and immersed solutions of low reynolds-number 3-d incompressible flows. *International Journal for Numerical Methods in Fluids*, 57(1):13–30, 2008.

[60] R. Löhner, J. D. Baum, E. Mestreau, D. Sharov, C. Charman, and D. Pelessone. Adaptive embedded unstructured grid methods. *International Journal for Numerical Methods in Engineering*, 60(3):641–660, 2004.

[61] H. Lu, D. Wan Kim, and W. Kam Liu. Treatment of discontinuity in the reproducing kernel element method. *International Journal for Numerical Methods in Engineering*, 63(2):241–255, 2005.

[62] Y. Lu, T. Belytschko, and L. Gu. A new implementation of the element free galerkin method. *Computer Methods in Applied Mechanics and Engineering*, 113(3):397 – 414, 1994.

[63] D. McQueen and C. Peskin. Shared-memory parallel vector implementation of the immersed boundary method for the computation of blood flow in the beating mammalian heart. *The Journal of Supercomputing*, 11(3):213–236, 1997.

[64] J. Melton, M. Berger, M. Aftosmis, and M. Wong. 3D applications of a cartesian grid Euler method. In *33rd Aerospace Sciences Meeting and Exhibit*. American Institute of Aeronautics and Astronautics, 1995.

[65] R. Mittal and G. Iaccarino. Immersed boundary methods. *Annual Review of Fluid Mechanics*, 37(1):239–261, 2005.

[66] J. Mohd-Yusof. Combined immersed-boundary/B-spline methods for simulations of flow in complex geometries. In *CTR Annual Research Briefs*, pages 317–327. NASA Ames Research Center, Stanford University, 1997.

[67] S. M. Murman, M. J. Aftosmis, and M. Berger. Implicit approaches for moving boundaries in a 3-D cartesian method. In *41st AIAA Aerospace Sciences Meeting*, number AIAA-2003-1119, 2003.

[68] J. Nitsche. Über ein variationsprinzip zur lösung von dirichlet-problemen bei verwendung von teilräumen, die keinen randbedingungen unterworfen sind. In *Abhandlungen aus dem mathematischen Seminar der Universität Hamburg*, volume 36, pages 9–15. Springer, 1971.

[69] J. Parvizian, A. Düster, and E. Rank. Finite cell method. *Computational Mechanics*, 41(1):121–133, 2007.

[70] C. S. Peskin. Numerical analysis of blood flow in the heart. *Journal of Computational Physics*, 25(3):220 – 252, 1977.

[71] C. S. Peskin. The immersed boundary method. *Acta Numerica*, 11:479–517, 2002.

[72] C. S. Peskin and D. M. McQueen. A three-dimensional computational method for blood flow in the heart i. immersed elastic fibers in a viscous incompressible fluid. *Journal of Computational Physics*, 81(2):372 – 405, 1989.

[73] M. A. Puso, J. S. Chen, E. Zywicz, and W. Elmer. Meshfree and finite element nodal integration methods. *International Journal for Numerical Methods in Engineering*, 74(3):416–446, 2008.

[74] A. M. Roma, C. S. Peskin, and M. J. Berger. An adaptive version of the immersed boundary method. *Journal of Computational Physics*, 153(2):509 – 534, 1999.

[75] M. J. Roth, J.-S. Chen, K. T. Danielson, and T. R. Slawson. Hydrodynamic meshfree method for high-rate solid dynamics using a Rankine–Hugoniot enhancement in a Riemann-SCNI framework. *International Journal for Numerical Methods in Engineering*, 108(12):1525–1549, 2016. nme.5266.

[76] J. Sanders and M. A. Puso. An embedded mesh method for treating overlapping finite element meshes. *International Journal for Numerical Methods in Engineering*, 91(3):289–305, 2012.

[77] M. Smith. *ABAQUS/Standard User's Manual, Version 6.9*. Simulia, 2009.

[78] N. Sukumar, D. Chopp, N. Moës, and T. Belytschko. Modeling holes and inclusions by level sets in the extended finite-element method. *Computer Methods in Applied Mechanics and Engineering*, 190(46):6183 – 6200, 2001.

[79] N. Sukumar, N. Moës, B. Moran, and T. Belytschko. Extended finite element method for three-dimensional crack modelling. *International Journal for Numerical Methods in Engineering*, 48(11):1549–1570, 2000.

[80] D. Wang, J.-S. Chen, and L. Sun. Homogenization of magnetostrictive particle-filled elastomers using an interface-enriched reproducing kernel particle method. *Finite Elements in Analysis and Design*, 39(8):765 – 782, 2003. 14th Robert J. Melosh Competition.

[81] X. Wang and W. K. Liu. Extended immersed boundary method using fem and rkpm. *Computer Methods in Applied Mechanics and Engineering*, 193(12):1305 – 1321, 2004. Meshfree Methods: Recent Advances and New Applications.

[82] X. Wang, C. Wang, and L. T. Zhang. Semi-implicit formulation of the immersed finite element method. *Computational Mechanics*, 49(4):421–430, 2012.

[83] X. Wang and L. T. Zhang. Interpolation functions in the immersed boundary and finite element methods. *Computational Mechanics*, 45(4):321, 2009.

[84] X. Wang and L. T. Zhang. Modified immersed finite element method for fully-coupled fluid–structure interactions. *Computer Methods in Applied Mechanics and Engineering*, 267:150 – 169, 2013.

[85] Y. Wang, P. K. Jimack, and M. A. Walkley. A one-field monolithic fictitious domain method for fluid–structure interactions. *Computer Methods in Applied Mechanics and Engineering*, 317:1146 – 1168, 2017.

[86] C. Wu, Y. Guo, and E. Askari. Numerical modeling of composite solids using an immersed meshfree galerkin method. *Composites Part B: Engineering*, 45(1):1397 – 1413, 2013.

[87] C. Wu, D. Wang, and Y. Guo. An immersed particle modeling technique for the three-dimensional large strain simulation of particulate-reinforced metal-matrix composites. *Applied Mathematical Modelling*, 40(4):2500 – 2513, 2016.

[88] Z. Yu. A DLM/FD method for fluid/flexible-body interactions. *Journal of Computational Physics*, 207(1):1 – 27, 2005.

[89] L. Zhang and M. Gay. Immersed finite element method for fluid-structure interactions. *Journal of Fluids and Structures*, 23(6):839 – 857, 2007.

[90] L. Zhang, A. Gerstenberger, X. Wang, and W. K. Liu. Immersed finite element method. *Computer Methods in Applied Mechanics and Engineering*, 193(21):2051 – 2067, 2004. Flow Simulation and Modeling.